HORIZONTAL CALIBRATION OF VESSEL LEVER ARMS

USING NON-TRADITIONAL SURVEY METHODS

BY

CASEY O'HERAN

Bachelor of Science in Surveying Engineering, Ferris State University, 2018

Associate in Applied Science in Surveying Technology, Ferris State University, 2017

THESIS

Submitted to the University of New Hampshire
In Partial Fulfillment of
The Requirements for the Degree of

Master of Science
In
Ocean Engineering: Ocean Mapping

May, 2020

COMMITTEE

This thesis was examined and approved in partial fulfillment of the requirements for the degree of Master of Science in Ocean Engineering: Ocean Mapping:

Thesis Director, Brian Calder,
Research Professor of Ocean Engineering

Semme Dijkstra,
Affiliate Professor of Earth Sciences

Christopher Parrish,
Associate Professor, Oregon State University
Affiliate Associate Professor, CCOM

Approval signatures are on file with the University of New Hampshire Graduate School.

DEDICATION

To my family, friends, and colleagues that have helped along the way to shape this project,

this is for you. I am eternally grateful for your support.

ACKNOWLEDGEMENTS

TABLE OF CONTENTS

LIST OF TABLES

LIST OF FIGURES

LIST OF APPENDIX FIGURES

GLOSSARY

AGL – Above Ground Level

ASPRS – American Society of Photogrammetry and Remote Sensing

CCOM – Center for Coastal and Ocean Mapping

CORS – Continuously Operating Reference Station

CSB – Crowdsourced Bathymetry

DCDB – International Hydrographic Organization Data Centre for Digital Bathymetry

DEM – Digital Elevation Model

EXIF – Exchangeable Image File Format

GCP – Ground Control Point

GNSS – Global Navigation Satellite System

GPS – Global Position System

GSD – Ground Sampling Distance

HTDP – Horizontal Time-Dependent Positioning

IHO – International Hydrographic Organization

IMU – Inertial Measurement Unit

ITRF – International Terrestrial Reference Frame

MBES – Multibeam Echo Sounder

MRU – Motion Reference Unit

MVS – Multi-View Stereo

NAD 83 – North American Datum of 1983

NGS – National Geodetic Survey

NOAA – National Oceanic and Atmospheric Administration

NVA – Non-vegetated Vertical Accuracy

PPK – Post-Processing Kinematic

RGB – Red Green Blue

RMS – Root Mean Square

RMSE – Root Mean Square Error

RTK – Real Time Kinematic

SfM – Structure from Motion

SOP – Standard Operating Procedure

SPCS – State Plane Coordinate System

SRF – Ship's Reference Frame

TCB – Trusted Community Bathymetry

UAS – Unmanned Aircraft System

UNH – University of New Hampshire

UTM – Universal Transverse Mercator

VVA – Vegetated Vertical Accuracy

WGS84 – World Geodetic System of 1984

2D – Two-dimensional

3D – Three-dimensional

ABSTRACT

HORIZONTAL CALIBRATION OF VESSEL LEVER ARMS USING

NON-TRADITIONAL SURVEY METHODS

by

Casey O'Heran

University of New Hampshire, April 17, 2020

Knowledge of offset vectors from sonars, mounted on vessels, to systems such as Inertial Measurement Units (IMUs) and Global Navigation Satellite Systems (GNSS) is crucial for accurate ocean mapping applications. Traditional survey methods, such as employing laser scanners or total stations, are used to determine professional vessel offset distances reliably. However, for vessels of opportunity that are collecting volunteer bathymetric data, it is beneficial to consider survey methods that are less time consuming, less expensive, and which do not involve bringing the vessel into a dry dock. Thus, this thesis explores three alternative methods that meet this criterion for horizontally calibrating vessels

With the development of Unmanned Aircraft Systems (UASs) in the field of mapping, more cost-effective and quicker surveys can be conducted. For standard mapping applications, the tradeoff in using UASs compared to traditional surveying instruments is that there is an increase in errors. To investigate the potential of using UASs to accurately calibrate horizontal vessel offsets, UASs were utilized to calibrate a vessel with both Structure from Motion (SfM) photogrammetry and aerial lidar while the vessel was

moored. Estimates of the horizontal deviations from ground truth, for both methods, were obtained by comparing the horizontal distances between targets on a vessel, acquired by the UAS methods, to ground-truth measurements of offset distances from survey-grade laser scanning of the vessel. In addition to the UAS methods, a seafloor reference technique that involves collecting single-beam echo sounder (SBES) data over a known bathymetric feature to estimate horizontal offsets of a vessel, was investigated.

Errors for the seafloor reference method were on the meter level and therefore may only be relevant for larger offsets such as on larger ships. In contrast, UAS methods were able to achieve horizontal deviations on the order of centimeters with the use of Ground Control Points (GCPs).

CHAPTER 1

INTRODUCTION

1.1   Crowd Sourced Bathymetry

Ocean mapping can be described as the technique of surveying underneath the surface of the water to estimate the topography of the ocean floor. Modern technologies such as satellites and aircraft equipped with electromagnetic energy sensors (e.g., passive/active light and radar) and oceanographic vessels equipped with echo sounders, have become popular to map the seabed (Hillman, 2019). However, direct measurement of depth with active remote sensing techniques (e.g., bathymetric lidar) is only possible to depths of several tens of meters, even in the clearest waters. (Mayer et al., 2018). This has left the majority of the ocean unmapped, resulting in the implementation of vessels equipped with echo sounders as the dominant source of high-resolution seabed data.

Utilizing echo sounders to map the ocean is crucial to understanding ocean processes, as much of what happens on Earth (e.g., weather, human activity, and geomorphic processes) is controlled by the 71% ocean coverage on the surface (Weatherall et al., 2015). Commonly, acoustical mapping of the seafloor occurs by securing single-beam and/or multibeam echo sounders to a mount or hull of a vessel. Single-beam echo sounders (SBES) send out a series of acoustic pulses to the seabed where they are reflected and returned to the echo sounder for a series of depth measurements; multibeam echo sounders (MBES) send out an acoustic pulse in a swath coverage, obtaining multiple seabed depth

measurements at a time (SeaBeam, 2000). Single-beam systems are generally less expensive and take less time to process than multibeam systems. However, multibeam systems achieve a significantly higher amount of seafloor coverage over a shorter time span. Each type of echo sounding system has its benefits and limitations, but both types possess the ability to contribute to seafloor mapping efforts. Even with these systems, under 18% of the oceans have been mapped by echo sounders (Mayer et al., 2018). Since there is much of the seafloor left to the mapped, the Seabed 2030 initiative was created in June 2016 with the goal of mapping the entire seafloor at depth-dependent resolutions by 2030 (Mayer et al., 2018). Successfully executing this initiative requires cooperation from public and private entities across the world that are associated with ocean mapping operations. However, with the immense amount of seafloor remaining unmapped it is reasonable to believe that further assistance in completing this initiative could come from voluntary sources (Robertson, 2016).

Data collected by a group of voluntary participants for the purpose of contributing to a collective goal is known as crowd sourcing. Similarly, crowdsourced bathymetry (CSB) is the voluntary collection of depths measured by vessels equipped with standard navigation systems undergoing routine maritime activities (Luma-ang, 2017 and IHO, 2020). Data such as these can be provided by a CSB mariner for public consumption. The International Hydrographic Organization's (IHO) Data Centre for Digital Bathymetry (DCDB) is a system that holds worldwide bathymetric data and now accepts CSB contributions (IHO, 2020). Before the CSB data is transmitted to the DCDB, it must go through trusted nodes, entities serving as liaisons between CSB mariners and the DCDB (IHO, 2020). The

network of trusted nodes offers a variety of support services to mariners, but the support does not guarantee the CSB data can be trusted. As Dodge and Kitchin (2013) suggest, the integrity of crowd sourced geospatial data can be called into question due to the potential inexperience of the crowd in relation to the complexity in collecting high quality geospatial data. Ensuring high quality geospatial data is being collected by the crowd requires knowledge that the crowd possesses the proper equipment setup and are performing the procedures necessary to collect trusted geospatial data. CSB is not exempt from this concept due to the complex nature of ocean mapping operations. Achieving accurate CSB data requires reassurance that operations are being conducted in a manner conducive for producing trusted bathymetric data.

Obtaining accurate seafloor mapping data commences with integrating the vessel's echo sounder(s) with other equipment on board, such as Global Navigation Satellite System (GNSS) receiver(s), and an Inertial Measurement Unit (IMU). Vectors indicating the coordinate differences between such pieces of equipment, lever arms (Hughes Clarke, 2003), must be known and are crucial in producing accurate estimations of the horizontal and vertical locations of soundings that are reflected from the seafloor. For professional mapping vessels, static surveys are performed in external coordinate systems to establish locations of the sensors and other markers on board the vessel; these measurements can then be used to establish the Ship's Reference Frame (SRF) (Hughes Clarke, 2003). The SRF organizes the locations of the sensors with respect to an origin designated as the reference point on the vessel. Instruments utilized to conduct SRF calibration surveys often involve traditional survey instruments such as total stations or laser scanners. Costs

associated with such instruments and high quality of survey can be significant. In addition, time spent on such a survey can be lengthy due to the process requiring the vessel to be placed in a dry dock. However, vessels designated for high-quality ocean mapping operations require such services to generate the desired accurate locations and depths of the seafloor derived from acoustic soundings.

It is unreasonable to expect voluntary CSB participants to pay a considerable amount of money and spend a substantial amount of time to have their vessel statically surveyed in a dry dock. This problem has resulted in most CSB vessels not possessing an SRF or accurate knowledge of the vessel's lever arm vectors. Without known lever arm vectors the sonar and other sensors cannot be properly integrated with each other, which could lead to unreliable CSB data. Methods outside the traditional static survey techniques must be explored to procure higher quality CSB data at reasonable cost.

Techniques aimed at making CSB data more trustworthy must be capable of obtaining both vertical and horizontal offset distances between a vessel's GNSS antenna and its sonar in a time/cost efficient manner. Additionally, it is important to set a standard of how accurate calibration methods should be for CSB applications. Most ocean mapping applications require centimeter level or better lever arm accuracies. On most CSB vessels the offsets are not known, but if the offsets were to be calibrated it is probably more realistic to expect CSB lever arms with errors of 1-30 cm. A Trusted Community Bathymetry (TCB) system that integrates a GNSS antenna with a single-beam sonar to autonomously compute the vertical offset, falls within this error range (Calder et al., 2020). Soundings with an

4

estimated vertical uncertainty of 0.16 m (one sigma) with respect to the ellipsoid were demonstrated using the TCB system (Calder et al., 2020). This hardware has the potential to significantly improve the vertical accuracies of CSB data, but it does not yet possess the ability to accurately define the horizontal offsets between the GNSS antenna and sonar. Until a solution to this issue is proposed, soundings produced utilizing the TCB system will not be georeferenced to the soundings' true horizontal location. The value and reliability of CSB data could increase if data is collected with proper vertical and horizontal sensor offsets. Consequently, this thesis focuses its research on examining and creating Standard Operating Procedures (SOPs) for non-traditional survey techniques to calibrate horizontal sensor offsets on vessels, as there already exists practical alternative vertical vessel calibration methods.

1.2 Proposed Methods

1.2.1 UAS Methods

Development of Unmanned Aircraft Systems (UASs) for civilian based remote sensing applications has increased extensively over the last decade, leading to UASs achieving spatial mapping resolutions of 1-20 cm (Nebiker et al., 2008). Two sensors are commonly employed when conducting UAS based remote sensing operations: cameras and lidar units. Cameras can be equipped to UASs where a collection of two-dimensional (2D) images are captured and processed by mathematical photogrammetric Structure from Motion (SfM) and multi-view stereo (MVS) algorithms, generating a 3D model of the surveyed area (Sanz-Ablanedo et al., 2018). This technology supports the ability to perform high resolution geospatial mapping with low-cost consumer grade UASs. Lidar based UAS

operations, however, are costlier and intricate to set up when compared to UAS SfM photogrammetry. As shown by Simpson (2018), UAS lidar advantages include fast collection, surface characterization, penetration of vegetation, vertical feature mapping, and capability of global accuracy. Both UAS sensors have demonstrated that they can quickly and efficiently map objects.

The characteristics of UAS mapping make it a potential candidate for meeting the desire to quickly and cost effectively survey a vessel's horizontal lever arms. However, if a UAS survey of a vessel were to be performed in the traditional manner by placing the vessel in a dry dock, the survey would still be costly and take a substantial amount of time. Conducting a UAS vessel calibration survey without placing the vessel in a dry dock would tremendously reduce the time and cost required to perform the survey, making such a service a viable option for CSB operators. Thus, this research proposes conducting UAS surveys of a vessel while it remains in water. This concept implies that the vessel would not be completely static while being mapped by a UAS. Therefore, this research investigates the implementation of UASs to perform horizontal lever arm calibrations of moored vessels, along with the exploration of factors that contribute to the uncertainty associated with such a survey. As this research could lead to a professional service available to CSB vessels, it was important to design the protocol methods in ways that would offer practical horizontal vessel calibration guidance to the CSB community.

In this investigation two separate methods are considered: SfM photogrammetry from a low-cost consumer grade UAS and lidar from a higher cost industrial grade UAS. Common

low-cost UASs can perform simple high-resolution photogrammetry surveys without survey grade GNSS capabilities. However, UAS lidar requires expensive industrial grade UASs equipped with survey grade GNSS receivers. Applying both methods independently to determine the lever arms on a single vessel allows a complete assessment of accuracy and cost between these methods, similar to that done by Simpson (2018), but for the application of mapping a slightly moving object. Since the focus of this research is on making accurate measurements between points on a vessel, it may not be necessary to georeference or conduct the surveys with Real Time Kinematic (RTK) GNSS enabled UASs to achieve accurate lever arm vectors. UASs with non-RTK GNSS receivers could possibly generate properly scaled models without accurately georeferencing the object, however, georeferencing has the potential to increase the accuracy of the survey. Hence, it is important to investigate whether it is necessary to georeference a vessel when conducting a horizontal lever arm calibration. As a result, two UAS SfM photogrammetry methods are proposed: processing with and without Ground Control Points (GCPs). GCPs are known three-dimensional (3D) coordinates within the area of survey that are utilized to georeference the model in post-processing. Indirect georeferencing, assigning known coordinates to targets present in the photographs (Sanz-Ablanedo et al., 2018), was the chosen georeferencing method as it was the easiest to conduct given the implementation of a consumer grade UAS. This branching workflow demonstrates whether this type of survey could be performed without laying ground control and how accurate the survey could be by georeferencing the model with GCPs. Information such as this is critical for the implementation of UAS SfM vessel calibration surveys. In summary, this thesis

investigates implementing UAS lidar in addition to UAS SfM photogrammetry, with and without utilizing GCPs, to horizontally calibrate vessel lever arms.

1.2.2 Echo Sounding Method

An additional vessel calibration source can come from the utilization of SBES. There currently exists a set of MBES calibration procedures that involve collecting pairs of survey lines over a defined bathymetric area and cross comparing the lines to estimate offsets. This protocol is known as the patch test and it ascertains the roll, pitch, and heading misalignment angles associated with MBES (Herlihy, 1989). Patch tests are essential to collecting accurate multibeam bathymetry data. Similar to patch tests, it would be beneficial for vessels to possess a means of acquiring their horizontal lever arms through an equivalent SBES based calibration. A method by which to do this would involve mapping a distinct bathymetric feature that has already been mapped accurately with a MBES. The exact feature would be observed with an echo sounder, simultaneously setting the lever arm offsets to zero, thus producing the 3D feature in a location hypothetically offset by the lever arm vectors, Figure 1. Utilizing the known feature location from the multibeam data, the observed data would be calibrated by estimating the lever arm distances until the observed and known features visually align. This process could potentially be done with two pairs of lines instead of the three necessary for a patch test. Given that most CSB vessels utilize SBES, this research investigates the procedure described above while using a single-beam system.

8
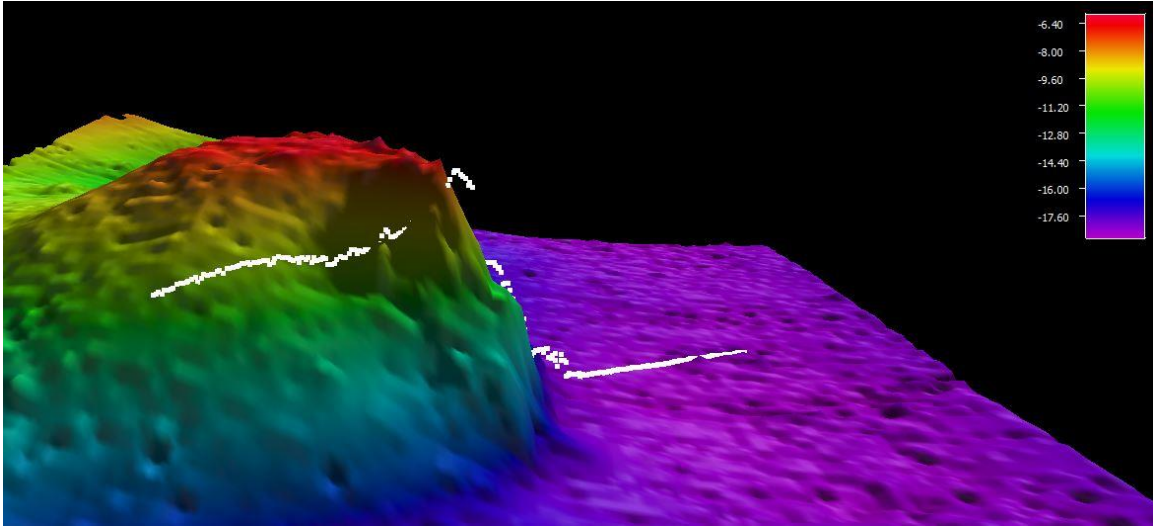
Figure 1: Cod Rock, a bathymetric feature in the Piscataqua River, New Hampshire. A reference MBES surface is overlaid with horizontally displaced single-beam data (white).

1.2.3 Summary

In total, three distinct methods for calibrating horizontal vessel lever arms are proposed and investigated in this thesis. Proposed methods include UAS SfM photogrammetry, UAS lidar, and a single-beam seafloor reference technique. All three methods have been extensively tested for the purpose of crafting SOPs, creating recommendations for future work, accuracy assessment, and method comparison.

CHAPTER 2

METHODS

2.1 Introduction

2.1.1 Vessel

The vessel selected for all three proposed calibration methods was the *R/V Gulf Surveyor,* Figure 2. This vessel was chosen because it is owned by the Center for Coastal and Ocean Mapping (CCOM), has previously surveyed-in monuments within its own established reference frame, and is fully equipped to conduct ocean mapping operations. Having a pre-calibrated vessel for any succeeding lever arm survey enables a direct comparison of measurements taken from the ground-truth survey to measurements obtained from the three proposed methods. Doucet Survey Inc. performed the original ground truth survey of the *R/V Gulf Surveyor* in 2016, Figures 3 and 4. With the vessel in a dry dock, a Leica P40 laser scanner was used to perform 40 high definition laser scan setups of the vessel. All scans were registered and a designated point inside the cabin was chosen to represent the origin of the Ship's Reference Frame (SRF). More points within the scans were then chosen to help establish the axes of the SRF, with the x-axis being positive towards the bow, the y-axis positive towards starboard side, and the z-axis positive downward. In total, 14 monuments were established on the vessel with known 3D coordinates within the SRF. 3D uncertainties for the associated monuments fell under three millimeters (Doucet Survey INC, 2016). The quality of this calibration survey meets the standards required for high

quality ocean mapping applications, making this vessel and its associated survey suitable ground truth data to compare against the proposed calibration methods.

Figure 2: The Center for Coastal and Ocean Mapping's (CCOM) 14.6 meter long hydrographic research vessel, the *R/V Gulf Surveyor*. (CCOM/JHC, 2019)

Figure 3: Laser scan survey of the *R/V Gulf Surveyor* performed by Doucet Survey Inc. (Doucet Survey INC, 2016)

POINT	X	Y	Z	DESCRIPTION
500	0.000	0.000	0.000	TOP-OF-STUD
501	7.164	0.000	-0.439	MONUMENT-BOW
504	1.575	0.003	0.111	SCREW-CAB-FLOOR
505	-2.843	0.007	0.101	MON-STERN-FLOOR
506	1.673	-2.587	-0.737	MON-PORT-RAIL
507	1.656	2.585	-0.739	MON-STAR-RAIL
508	1.690	0.000	-2.143	MON-UPPER-DECK
509	3.320	-1.845	-4.319	MON-GNSS-PORT
510	3.314	1.822	-4.319	MON-GNSS-STAR
511	-1.671	0.018	-0.237	MON-PLATE
512	2.345	1.294	1.786	MON-CENTER-WINDOW-HULL
513	1.671	-2.544	-0.016	MON-CENTER-CLAMP-PORT

Figure 4: SRF coordinates (m) of markers on the *R/V Gulf Surveyor* derived from the ground truth laser scan survey (Doucet Survey Inc, 2016).

2.1.2 Experiment Site: UAS Surveys

For all UAS flights, the *R/V Gulf Surveyor* was docked at its home location at the University of New Hampshire (UNH) pier on New Castle Island, New Hampshire, as shown in Figure 5. This location was chosen because the vessel did not have to be moved from its usual docked location. Consequently, the UAS flights were conducted in an open area above the vessel and GCPs had to be established on the pier. Additionally, the pier is in a class G airspace, meaning no permission was needed to fly UASs. However, given the pier's association to UNH and its proximity to a United States Coast Guard station, permission from the UNH Police Chief was obtained to fly at the pier.
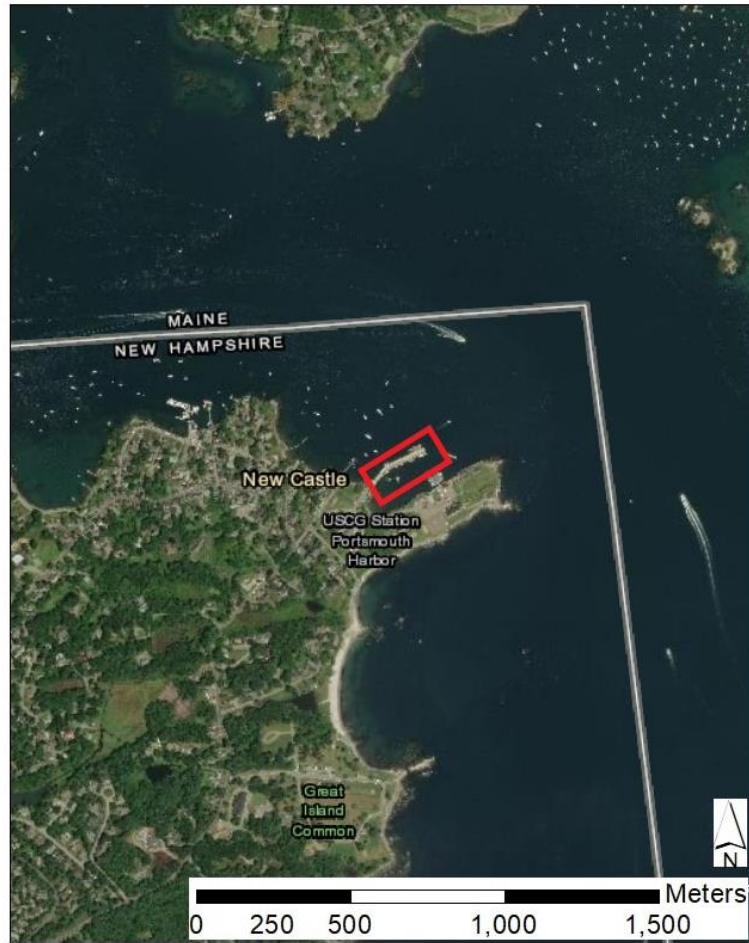
Figure 5: A map of New Castle, New Hampshire with the red rectangle identifying the site of survey at the UNH pier.

2.1.3 Experiment Sites: Seafloor Reference Method

Implementation of the single-beam echo sounding method occurred in the Piscataqua River, adjacent to the UNH pier where the UAS methods were developed, Figure 6. Features with significant bathymetric changes were required to properly test the echo sounding method. Thus, Cod Rock and Henderson Point were selected because of their recorded bathymetric changes shown in previous surveys of the river, Figures 7 and 8. Both locations allowed for enough maneuverability within the river. This enabled the vessel to perform the required survey experiments on the features.
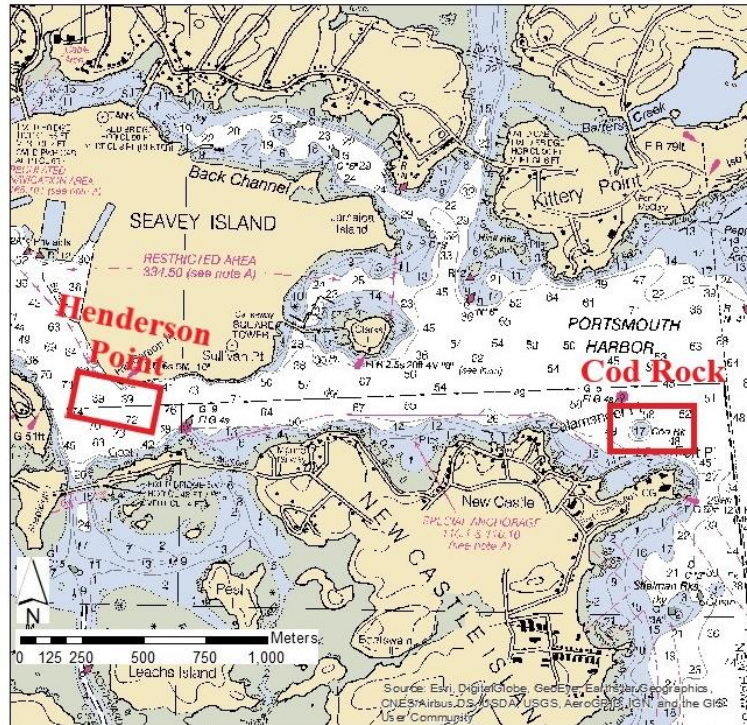
Figure 6: Locations within the Piscataqua River where the echo sounding method was tested. The red rectangles show the two locations in which the method was implemented.
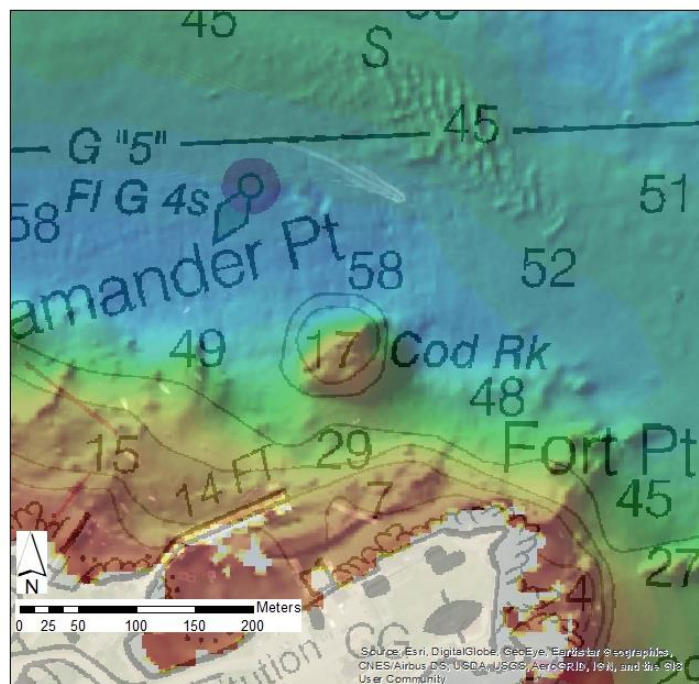
Figure 7: Cod Rock, a feature within the Piscataqua River chosen to implement the echo sounding method.

14
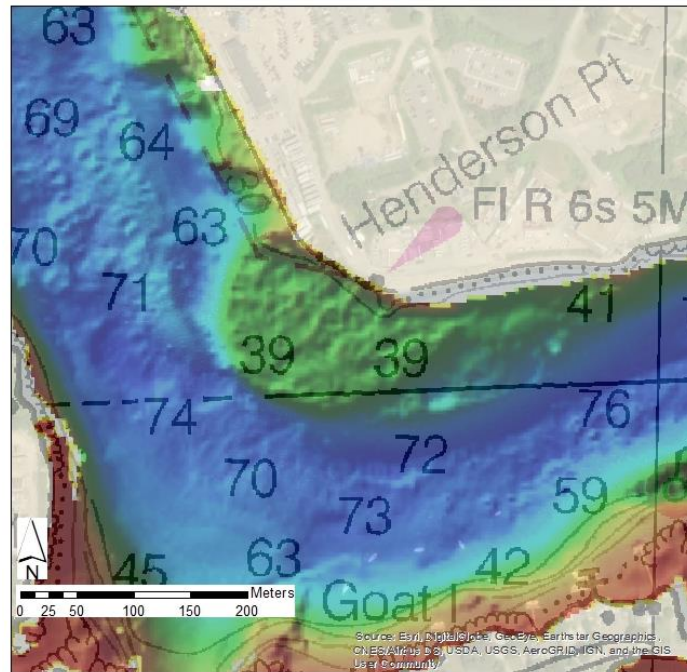
Figure 8: Henderson Point, a feature within the Piscataqua River chosen to implement the echo sounding method.

2.1.4   Timeline of Experiments

UAS data collection was completed on five separate days: one in the spring and four in the summer/fall of 2019. Single-beam collection occurred in the span of two days in January of 2020. See Table 1 for a detailed breakdown of all field experiments performed for this project along with the associated data that was collected on each date.

Table 1: Timeline of experiments conducted for this thesis.

Date	Primary Data Collected
Spring, 2016	Laser Scan Ground Truth Survey
April 17, 2019	Aerial Lidar & SfM Photogrammetry
August 6, 2019	GCP GNSS Observations
August 21, 2019	SfM Photogrammetry
August 22, 2019	SfM Photogrammetry
August 23, 2019	SfM Photogrammetry
November 7, 2019	SfM Photogrammetry
January 9, 2020	Single-Beam Echo Sounder
January 10, 2020	Single-Beam Echo Sounder

2.2 Ground Control Network: UAS Surveys

2.2.1 Ground Control Point Data Collection

A control network was established to accurately georeference the aerial lidar and SfM photogrammetry data, thus placing the vessel in its actual location in the world within a specific reference frame. Utilizing a ground control network enables a comparison between errors associated with the UAS models of the vessel created with and without ground control. On the first day of UAS data collection, a temporary control network was established using AeroPoints, Figure 9, which are single frequency GNSS receivers capable of 5 cm vertical and 2 cm horizontal Root Mean Square (RMS) accuracies (ARE, 2019). Ten AeroPoints, provided by ARE, were secured to the pier structure adjacent to the *R/V Gulf Surveyor* in a zig-zag pattern, Figure 10. The AeroPoints collected GNSS observations for approximately five hours. It is important to note for the following that the vessel was not located inside the ground control network.

Figure 9: AeroPoint target utilized as a GCP for the April 17, 2019 UAS survey.
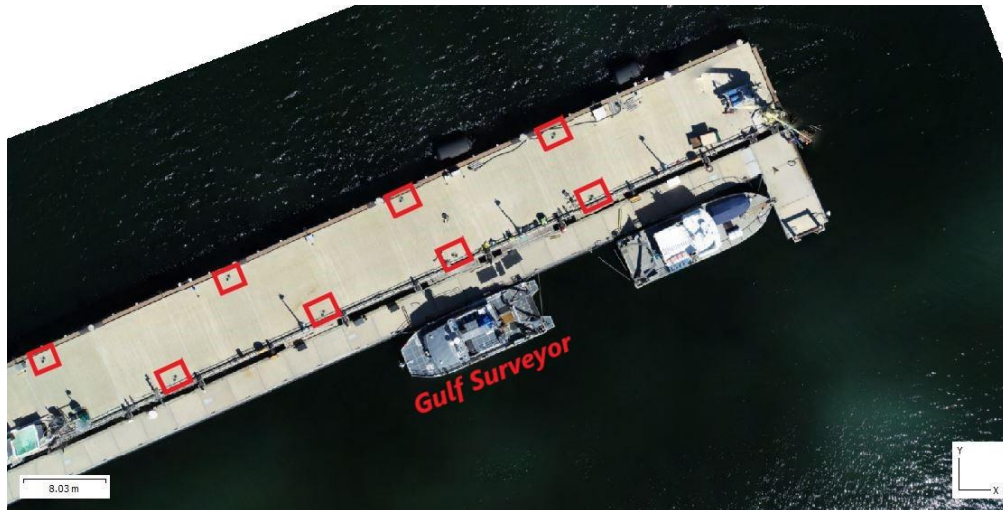
Figure 10: Layout of the AeroPoint control network for the April 17, 2019 UAS surveys.

For the remaining UAS experiments a separate set of GCPs were established due to the

lack of accessibility and affordability of ARE's AeroPoints. As seen in Figure 11, ten nylon

targets were spread out across the pier in a similar zig-zag fashion as the first control

network. The targets were affixed to the pier by placing gorilla tape on all four edges of the target. GNSS observations of the GCPs were taken with a Trimble 5700 receiver with a Zephyr geodetic antenna. Each target was statically occupied for ten minutes, Figure 12.

Figure 11: Layout of the second ground control network using nylon targets.
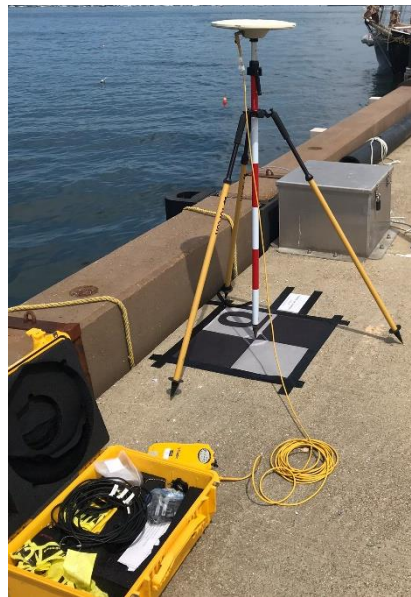
Figure 12: The second ground control network being surveyed in with Trimble GNSS equipment.

2.2.2   Ground Control Point Processing

The first set of GCPs were delivered by ARE in the North American Datum of 1983 (NAD83 (2011)), geodetic coordinates. This was due to ARE's typical file delivery format. Using the National Geodetic Survey (NGS) Horizontal Time-Dependent Positioning (HTDP) tool (NGS, 2020), the GCP coordinates were transformed into the World Geodetic System of 1984 (WGS84 (G1762)), which is aligned to the International Terrestrial Reference Frame (ITRF) of 2008 (ITRF2008). Since the SfM camera locations were output in WGS84, it was logical to convert the GCPs to that datum. The transformed coordinates were output in degrees of geodetic latitude and longitude with altitude in meters. Standard deviations for the first set of GCPs were derived by ARE and can be seen in Table 2.

Table 2: Standard deviations associated with the GCPs of the April 17, 2019 control network.

Point #	SD X (mm)	SD Y (mm)	SD Z (mm)
1	2.2	1.4	2.6
2	2.5	2.7	2.6
3	1.5	1.2	1.5
4	1.5	1.0	1.3
5	1.8	1.5	3.0
6	1.0	0.8	1.2
7	1.4	0.8	1.8
8	2.1	1.6	2.5
9	0.6	0.9	1.1
10	1.3	1.9	1.0

With the second set of GCPs the raw observations were downloaded using Trimble's data transfer software and converted to the RINEX 2.11 file format using Trimble's Convert to

RINEX utility. The RINEX files were post-processed using RTKlib, and a Continuously

Operating Reference Station (CORS), named NHUN, was used as the base station for post

processing the GNSS data. NHUN, located on UNH's campus, was the closest available

GNSS base station to the site of the UAS surveys, making it a logical choice as the base

station for post processing the observed GNSS data. Similar to the first set of GCPs, the

second set of GCPs were output in WGS84 (G1762), with coordinates being in degrees of

geodetic latitude and longitude with altitude in meters. Standard deviations for the second

set of GCPs were calculated in RTKlib and can be seen in Table 3.

Table 3: Standard deviations associated with the GCPs of the second ground control network.

Point #	SD X (mm)	SD Y (mm)	SD Z (mm)	SD XY (mm)	SD XZ (mm)	SD YZ (mm)
CT0	0.1	0.3	0.4	0.1	0.1	-0.1
CT1	0.2	0.4	0.7	0.1	0.1	-0.3
CT2	0.2	0.3	0.7	0.1	0.1	0.1
CT3	0.1	0.2	0.4	0	0.1	0
CT4	0.1	0.2	0.5	0.1	0.1	-0.2
CT5	0.1	0.2	0.4	-0.1	0	-0.1
CT6	0.1	0.2	0.3	0	0	0
CT7	0.1	0.2	0.3	-0.1	-0.1	0.1
CT8	0.2	0.2	0.3	0	-0.1	-0.1
CT9	0.2	0.2	0.3	0.1	0	-0.1

2.2.3 Vessel Targets

In addition to the established control networks on the pier, a set of targets were secured to

the *R/V Gulf Surveyor* prior to each UAS experiment. For the purpose of identifying the

square monuments with known SRF coordinates on the vessel from the aircraft, targets

with holes in the middle of the target were placed over the center of each visible monument,

Figure 13. This enabled the possibility for accurate measurements from monument to

monument within the lidar and SfM photogrammetry models. As a result, this allowed error estimates to be made by comparing the ground truth distances between monuments on the vessel to the observed distances. Three cut out targets were placed on the vessel as there were only three square monuments that could be seen from the aircraft. Two additional SRF points could be seen from the aircraft in the form of the starboard and port GNSS antennas. Figure 14 displays the locations of the five known SRF points that could be identified from above.
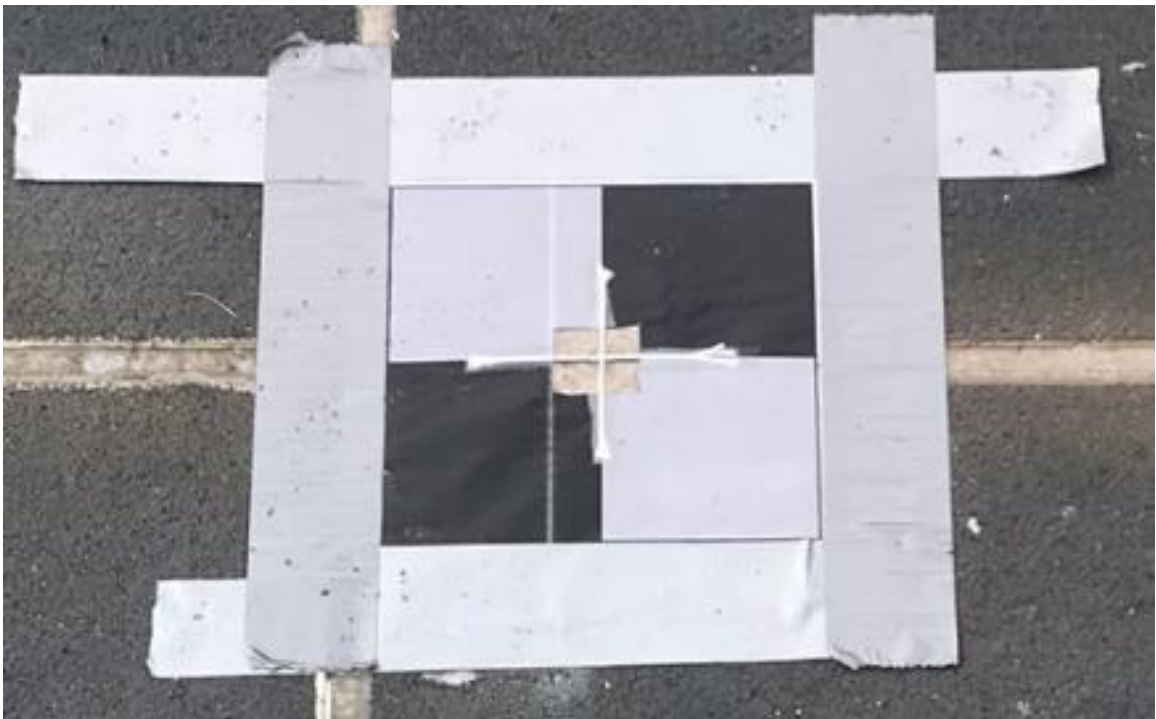
Figure 13: Modified paper target placed over a monument on board the *R/V Gulf Surveyor*. Cutout targets were utilized to accurately place the targets over the exact center point of each monument.
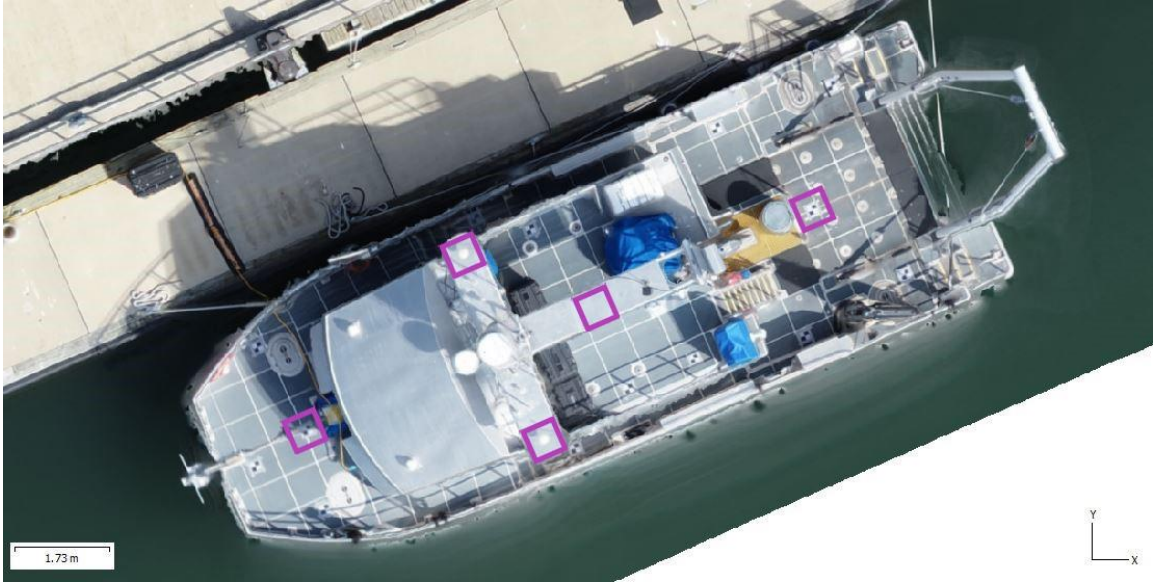
Figure 14: Locations of the SRF monuments on the *R/V Gulf Surveyor* utilized as a primary source of error estimation.

Along with the three cut out targets, 12 unmodified targets were placed around the vessel's main and top decks, Figure 15. As a secondary source of error estimation, measurements between the modified and unmodified vessel targets were taken with fiberglass tape. While taking measurements, the tape was held level with the surface of the deck and the ends centered on the middle of the targets. The vessel targets were secured to the vessel with gorilla tape before the flights were flown, 17 total measurements were made before or after the flights, and once the flights concluded for the day the targets were removed. A more durable target was considered, but given the potential moisture build up on deck overnight, it was not clear whether a more durable target would stay attached to the deck long term. Thus, paper targets were used and this process was repeated for each day of experimentation, resulting in the locations of the unmodified targets changing on the meter level each time as they were not placed in the same location after each iteration of experiments.
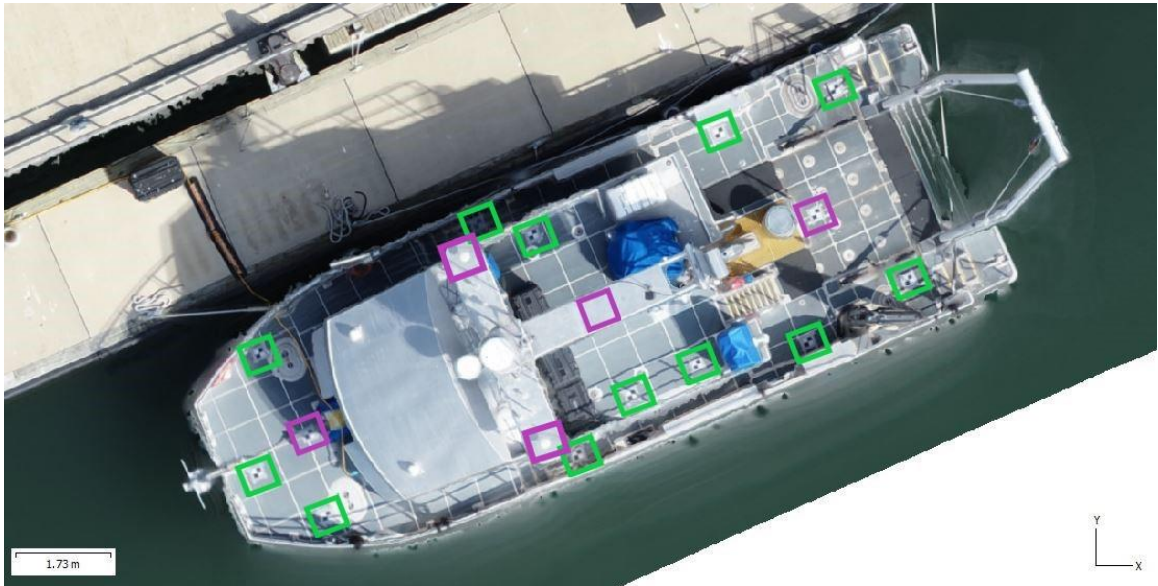
Figure 15: Shown are vessel targets utilized as a secondary source of error estimation. Unmodified vessel targets are in green and modified vessel targets shown in purple.

2.3 Auxiliary Data: UAS Surveys

2.3.1 Auxiliary Data Collection

Since the proposed UAS methods involve mapping a vessel while it is in the water, the vessel is not a completely fixed object while it is being mapped. Hence, it is important to observe and quantify the impact a vessel's motion has on the accuracies of such a survey. As potential contributing factors, changes in water level height and changes in the vessel's attitude during the time of flight were recorded. Water level data for every UAS experiment day was retrieved from the National Oceanic and Atmospheric Association (NOAA) Tides and Currents website; due to its close proximity to the survey area, the Fort Point tidal station was used. However, this data does not demonstrate how much small-scale movement the vessel undergoes.

To investigate further the effect a vessel's local horizontal and vertical motion has on UAS vessel calibration surveys, Motion Reference Unit (MRU) data was recorded on the *R/V Gulf Surveyor* on each day of experiment. The vessel's installed POS MV 320 v.5, which includes an Inertial Measurement Unit and two GNSS antennas, was used to record motion data of the vessel while the flights took place. Estimated accuracies for typical operating circumstances of the POS MV 320 can be seen in Figure 16. The POS MV 320's current presence on board the vessel and high degree of accuracy made it a viable source for collecting attitude data. Logging of the MRU data began approximately one hour before the commencement of flights for the day, with a logging frequency of 100 Hz for the April 17, 2019 experiment and 200 Hz for all other UAS experiment days. MRU data concluded logging approximately 15 minutes after flights for each experiment day ended. The attitude data was collected in relatively static conditions compared to typical ocean mapping operations, but the potential inertial drift that could have been experienced due to these conditions was most likely kept in check by the MRU's GNSS antennas.

PERFORMANCE SUMMARY - POS MV 320 ACCURACY

POS MV 320	DGPS	RTK	Accuracy During GNSS Outage
Position	0.5 - 2 m[1]	Horizontal: +/- (8 mm + 1 ppm x baseline length)[2] Vertical: +/- (15 mm + 1 ppm x baseline length)[2]	~ 6 m for 60 s total outages (DGPS) ~ 3 m for 60 s total outages (RTK) ~ 2 m for 60 s (post-processed DGNSS) ~ 1 m for 60 s total outages (IAPPK)
Roll & Pitch	0.02°	0.01° (0.008° with post processing)	0.02°
True Heading	0.01° with 4 m baseline 0.02° with 2 m baseline	-	1° per hour degradation (negligible for outages <60 s)
Heave TrueHeave™	5 cm or 5%[3] 2 cm or 2%[4]	5 cm or 5%[3] 2 cm or 2%[4]	5 cm or 5%[3] 2 cm or 2%[4]

Figure 16: Accuracies of the POS MV 320 (Applanix Corp., 2013).

2.3.2   Auxiliary Data Processing

Both auxiliary datasets were processed to assess what was happening to the vessel in the water while it was being mapped by the UAS sensors. A visual test of the tidal plots was performed to confirm what stage in the tidal cycle the surveys were performed. Differences in water level heights between the times at which the UAS surveys started and ended were taken, indicating how much the water level changed between flights. Having these data helps in understanding the impact tidal cycles have on the operational procedures of UAS vessel calibration surveys.

To understand the effects of the vessel's change in attitude, the MRU data were analyzed. Recorded roll, pitch, heading, heave, and their timestamps were extracted from the POS MV data files. Time series plots of the vessel's roll, pitch, and heading over the course of the UAS surveys were then generated.

An additional purpose in processing MRU data was to quantify the uncertainties introduced into the UAS vessel calibration surveys by analyzing how many pixels and how much distance the vessel moved due to the attitude changes induced by local water disturbances. To do this, a code was implemented to estimate the vessel's movement at a defined point in the SRF using the changes in the attitude values as the angles of rotation. Figure 17 lays out the computational steps utilized to determine how much the vessel shifted in a defined time interval from its starting orientation at the commencement of each flight.

| Read in recorded attitude information of the vessel during the flights (Roll, pitch, and heading). | → | Computed attitude deviations from the vessel's orientation at the start of the flight, with a defined time interval. | → | Defined a 3D point within the vessel's SRF (x,y,z): [7.164,0.00,-0.439] m | → | Computed rotation matrices based upon the vessel's orientation changes and applied them to the defined point. |

| Utilizing the rotated points, 3D distances the vessel moved from frame to frame were computed. | → | Calculated the ground sampling distance (cm/pixel) of the photos based on the camera properties and flying height. | → | The 3D vessel distance shifts were divided by the ground sampling distance. | → | Pixel shifts ,with a defined time interval, the vessel experienced during the SfM UAS flights were achieved. |

Figure 17: Computational procedure utilized to analyze the vessel's motion during UAS flights.

Distance/pixel shift time intervals for this code were set to one second to look at the short time-scale effects of the motion, and 15 seconds. The attitude time series and distance/pixel shift plots for all UAS datasets helped demonstrate how local vessel motion impacts UAS vessel calibration surveys. This code has been preserved and made available for future use through a Bitbucket repository (Contact info@ccom.unh.edu for more information).

2.4 UAS Structure from Motion

2.4.1 Structure from Motion Data Collection

UAS photogrammetry is the collection of aerial photographs obtained from an aircraft, which are then put through photogrammetric algorithms to construct a 3D point cloud of the photographed scene. From the photogrammetric point cloud an orthomosaic (a composite image formed from multiple photos of the same scene) can be used to perform measurements of the surveyed object. Five separate days of UAS SfM experiments were conducted to explore the practicality of performing horizontal vessel calibrations using

UAS photogrammetry. For this study, it was desired to evaluate the performance of a low-cost consumer grade UAS that has the capability of mapping an object at a high resolution. The DJI Phantom 4 Pro is a UAS that can be purchased off the shelf for around $2,000 (2019 US dollars), is equipped with an IMU and consumer grade GNSS, has the ability to be in the air for up to 30 minutes, and includes a 20-megapixel camera with properties shown in Table 4 (DJI, 2020). Due to its low cost, quality camera resolution, and reasonable battery life, the Phantom 4 Pro was selected for the SfM photogrammetry mapping missions of the *R/V Gulf Surveyor*, Figure 18.

Table 4: Phantom 4 Pro camera properties (DJI, 2020).

Property	Specifications
Focal Length	8.8 mm
Sensor Width	13.2 mm
Image Width	5472 pixels
Image Height	3648 pixels
ISO	100 - 12800
Shutter Speed	8 - 1/8000 s
Aperture	F2.8 - F11

Figure 18: The non-RTK/PPK version of the DJI Phantom 4 Pro UAS (DJI, 2020).

When carrying out UAS mapping missions a flight plan must be designed to fit the application of the end product. In this instance, we chose the deliverables to be clean point clouds and orthomosaics of the vessel that allow for horizontal measurements to be taken from multiple points on the orthomosaic or point cloud. Producing detailed 3D features from nadir imagery requires images to be collected in flight paths that are perpendicular to each other. As a result of this, a 3D grid mission in both along and across track directions with respect to the vessel were selected in Pix4D Capture as the primary form of UAS SfM data. Since high detail is desired for this type of survey, the amount of overlap between flight lines (side lap) and overlap between photos along a survey line (end lap) were both set to the maximum value of 90 percent. Along with overlap, the UAS's flying height helps determine the amount of detail captured in an image. Based on the area of the survey site along with investigating the effect flying height has on the accuracy of UAS SfM vessel calibration surveys, both 31 and 21 meter above ground level (AGL) flying heights were utilized, resulting in Ground Sampling Distances (GSD) under 0.85 cm/pixel. Figures 19 and 20 show the 3D grid missions with the respective survey properties flown at 31 and 21 meters above the *RV Gulf Surveyor*.
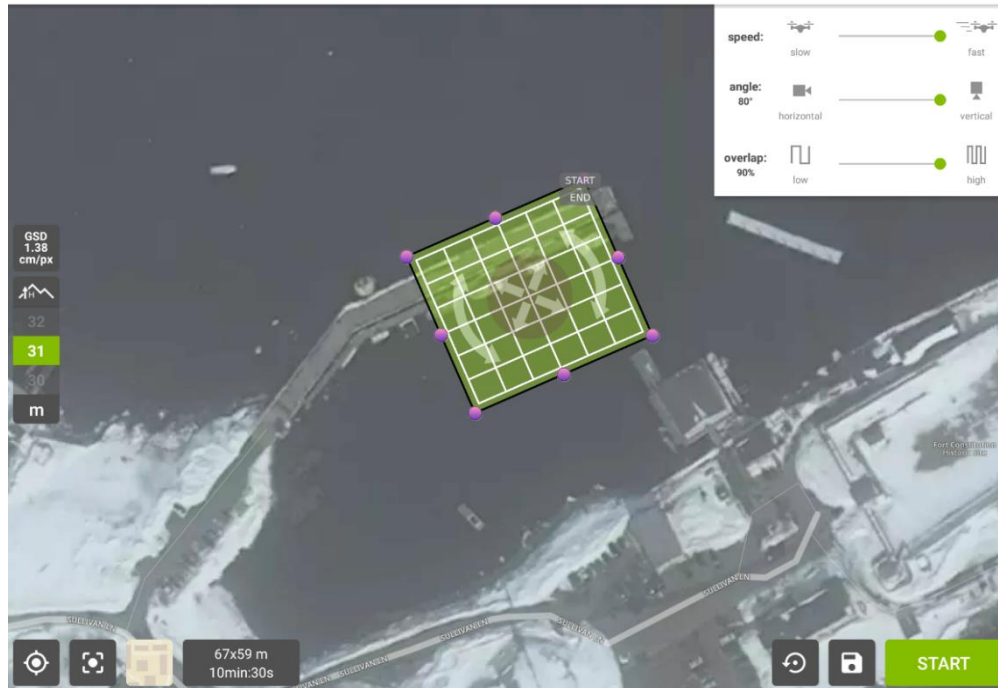
Figure 19: 3D grid pattern flown at 31 m over the UNH pier.
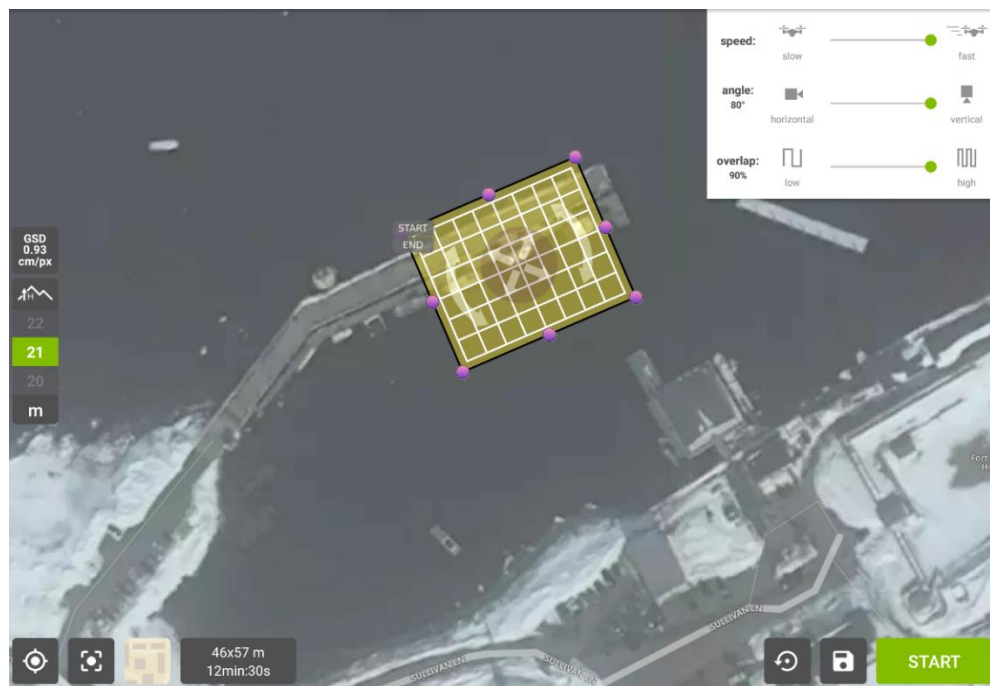
Figure 20: 3D grid pattern flown at 21 m over the UNH pier.

Even though 3D grid missions with nadir camera orientations are recommended when creating 3D surfaces from imagery, vertical detail of 3D objects can be lacking when employing this method. With an oblique camera orientation, images are collected with a camera intentionally tilted away from nadir, making it more effective at collecting detail on vertical features. Since the *R/V Gulf Surveyor* has vertical planes, circular orbits with a 45° camera angle (low oblique angle) were flown around the *R/V Gulf Surveyor* at 31 and 21 meters AGL to provide supplementary information to the 3D grid datasets, Figures 21 and 22. Additionally, oblique oriented elliptical flight paths following the along and across track directions of the vessel were flown at 31 meters. However, it is important to note that, for this application, horizontal calibrations of vessel lever arms are performed by taking horizontal measurements on planar surfaces of the vessel within the orthomosaic. Acquiring detailed information of the vertical features on the vessel is not crucial to the end goal, making it non-imperative to collect oblique imagery. A vertical vessel calibration survey using UAS SfM photogrammetry, however, would necessitate oblique imagery.
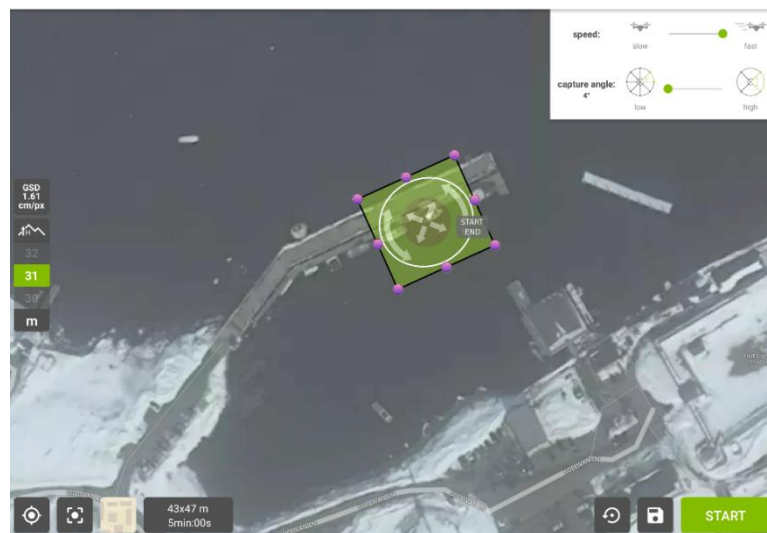
Figure 21: 31m circular orbit with oblique camera orientation flown over the UNH pier.
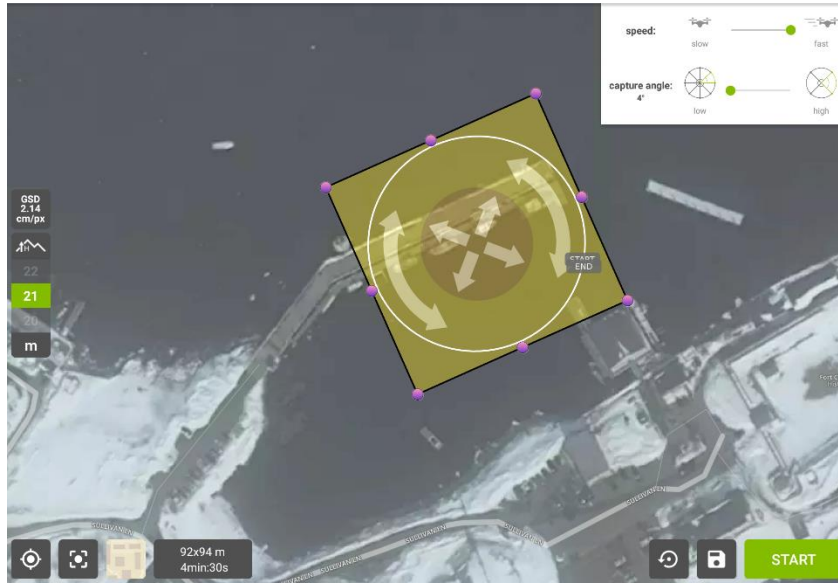
Figure 22: 21m circular orbit with oblique camera orientation flown over the UNH pier.

To obtain consistent datasets on which to compare, the SfM experiment days consisted of similar workflows, in addition to conducting experiments in mostly similar environmental conditions. Before each day of SfM data collection, all sensors on board the Phantom 4 Pro were calibrated: vision, IMU, and compass. Due to the UNH pier's metal framework, the UAS had to be launched either away from the pier, or on an elevated platform in order to avoid compass interference. Additionally, the set of camera properties shown in Table 5 were chosen and utilized over the span of all UAS SfM experiment days. As mentioned in chapter 2.3.1, low and high tide at the pier determined when the flights would occur because it was hypothesized that the significant vertical displacement the vessel could undergo during the survey as it moves with the tide could impact its quality. Given this hypothesis and the semidiurnal nature of the tides at the survey site, operating at low or high tide ensured at least two hours of proper flight time.

Table 5: Camera properties established for the UAS SfM photogrammetry surveys.

Property	Setting
Shutter Speed	1/800 s
ISO	Auto
Image Size	3:2
Image Format	JPEG
Color Balance	Sunny or cloudy
Mechanical Shutter	On
Exposure Value	-1 to 1 (Manually set based on cloud conditions)

For the purpose of limiting uncertainties induced by vessel motion into the UAS surveys, the vessel was tied down tight by adding extra mooring lines. In addition to the normal mooring lines used to tie the vessel to the pier, extra mooring lines were utilized to secure the vessel as tight as possible in hope of limiting the amount of horizontal motion the vessel could experience. On these days, two nadir grid missions and two oblique circular missions, flown at 31 and 21 meters AGL respectively, were carried out to survey the *R/V Gulf Surveyor*.

In an effort to investigate the effect vessel motion induced by local water disturbances has on accuracies of UAS vessel calibration surveys, UAS SfM photogrammetry flights were also performed with the vessel tied down loosely. The first experiment of this type was limited to just one 3D grid mission at 31 meters AGL due to weather constraints. However, the second experiment of its kind comprised of two 3D grid missions at 31 meters AGL with the vessel loosely tied down, and one 3D grid mission at 31 meters AGL with the vessel tied down tight.

The common workflow for the UAS SfM missions commenced with preparing the vessel to be surveyed. This procedure included laying the vessel targets, measuring the distances between vessel targets with fiberglass tape, ensuring GCPs were set, starting MRU logging, and securing the vessel to the dock with the desired number of mooring lines. These preparation procedures were followed by adjusting the camera settings of the UAS, performing UAS calibrations, and executing the desired flight missions. Upon completion of flights for the day, the vessel targets were removed and MRU logging ended.

2.4.2   Structure from Motion Data Processing

All SfM datasets were put through trials of data processing procedures in Agisoft Metashape, which was used to implement the SfM algorithm, reconstruct 3D scenes from collections of 2D images, and produce the following final deliverables: 3D point clouds, 3D surfaces, Digital Elevation Models (DEMs), and orthomosaics (Agisoft LLC, 2019). Many datasets and combinations of datasets were processed to gain a greater understanding of the limitations of UAS SfM photogrammetry for the application. In addition, the processing procedures enabled a further investigation of how uncertainties were being propagated into the final deliverables.

For the purposes of this project, Agisoft Metashape's auto calibration tool was used to calibrate the camera. Calibration parameters included focal length (f), principal point coordinates (cx and cy), radial distortion coefficients (k_1, k_2, and k_3), and tangential distortion coefficients (p_1 and p_2). Without an accurate camera calibration, an error phenomenon called the "doomed dome" can occur (James et al., 2014), which can

introduce significant vertical errors into the final DEM. James and Robson (2014) demonstrate that if self-calibration software is required, having a flight plan with oblique imagery can significantly limit this error. Additionally, they found that control points can help detect doming errors. Both ground control and oblique imagery were available for use in limiting the vertical doming errors through the camera calibration. However, with the application of this survey being to perform accurate horizontal measurements, possessing an extremely accurate camera calibration is not as pertinent as it would be if the main goal were to conduct accurate vertical measurements. Consequently, each unique section of data that was processed, no matter the flight properties or inclusion of GCPs, received its own camera calibration based on the data that was present within the individual section.

The general workflow that was employed followed the one outlined by the Agisoft Metashape version 1.5 manual, which starts with recommending the generation of a sparse point cloud by aligning cameras. This step matches common points between images, locates the position where each photograph was taken, and fine tunes the camera calibration and locations (Agisoft LLC, 2019). A dense point cloud can then be built from the estimated camera positions using an MVS algorithm, followed by deriving a mesh and DEM. Lastly, the orthomosaic can then be computed from either the 3D mesh or DEM. With the unusual task of modelling a slightly moving object, it was necessary to experiment with various processing parameters within the workflow.

As a result of the unusual conditions of the survey a few application-specific issues were encountered in processing. With the combination of location, design of the flight pattern,

and flying height, many images of murky water were collected. The software does not register these photos as they possess an insufficient number of matchable points needed for the SfM algorithm, justifying their removal in the filtering process. Additionally, an abundance of noise around the vessel at water level height was generated during the dense point cloud build due to the combination of water movement and lack of water clarity during the flights. This required careful manual cleaning of the dense point cloud.

When texturizing the meshes and orthomosaics built from the dense point clouds, disconnecting distortions occurred when implementing the mosaic blending method, Figure 23. However, a simpler approach to texturizing, the average blending method, which takes the weighted average pixels over all relevant photographs (Agisoft LLC, 2019), resulted in smooth orthomosaic and mesh textures, Figures 24 and 25. Consequently, the average texturizing method was utilized for almost all datasets.
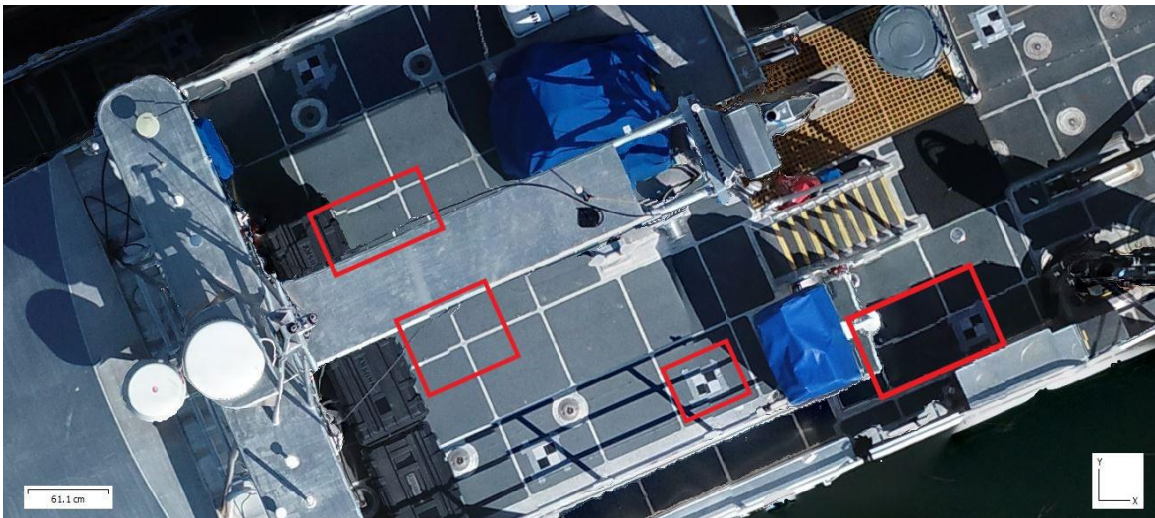
Figure 23: Orthomosaic of the *R/V Gulf Surveyor* created from photogrammetry data collected on August 22, 2019, texturized with the mosaic blending method. The red rectangles represent distortions.
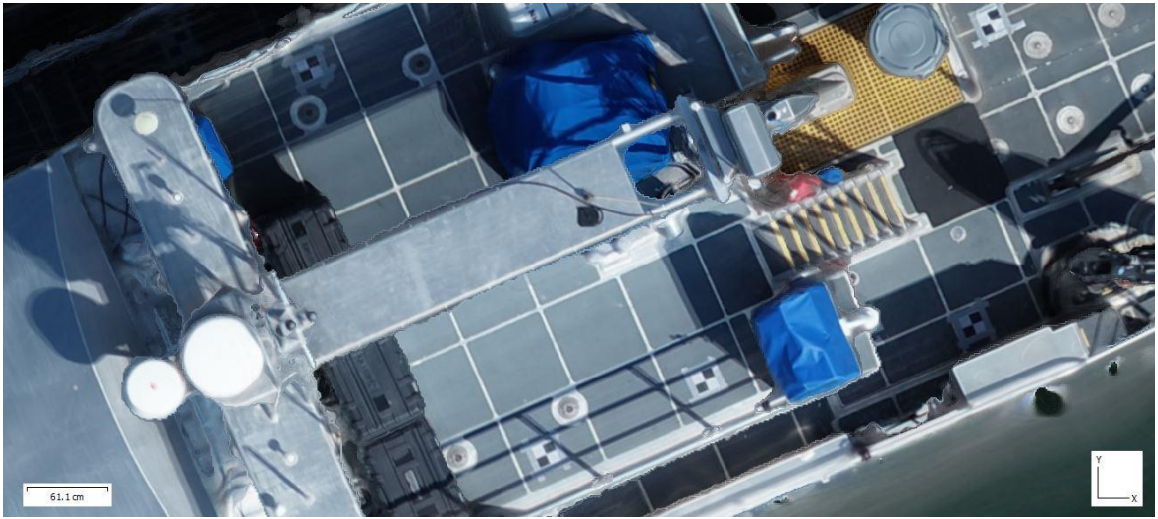
Figure 24: Orthomosaic of the *R/V Gulf Surveyor* created from photogrammetry data collected on August 22, 2019, texturized with the average blending method.
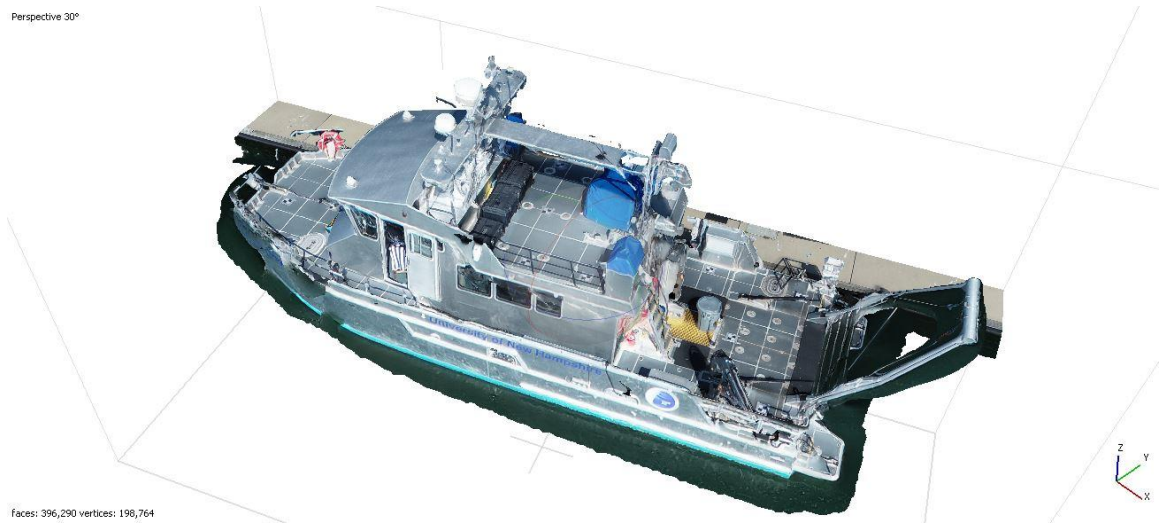
Figure 25: Mesh model of the *R/V Gulf Surveyor* created from photogrammetry data collected on August 22, 2019, texturized with the average blending method.

The final two steps in processing the UAS SfM data were generating the DEMs and orthomosaisc. DEMs were derived from either the dense point cloud or mesh in WGS84 (G1762) Universal Transverse Mercator (UTM) zone 19 North with interpolation enabled, Figure 26. Orthomosaics were created with DEMs or meshes as the base data and also were output in WGS84 UTM 19N. In preparing the models for accuracy assessment, polylines were drawn on the orthomosaic, marking the Euclidian distances between the centers of vessel targets, Figure 27. These measurements were taken in Agisoft Metashape and were primed to be directly compared to their ground truth counterparts. Every apparently minor processing detail had an important role in getting to the finished deliverables. Table 6 displays a detailed breakdown of the specific parameters utilized to process the UAS SfM photogrammetry data.
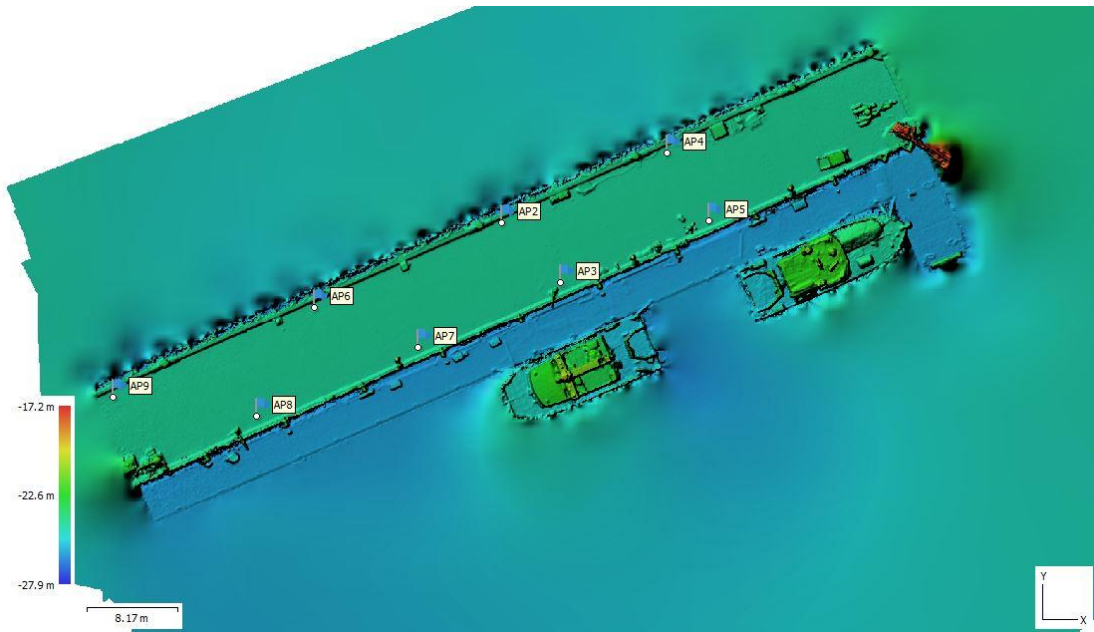
Figure 26: DEM of the *R/V Gulf Surveyor* and UNH pier made from photographs taken on April 17, 2019. The blue flags represent the GCPs utilized to georeference the model.
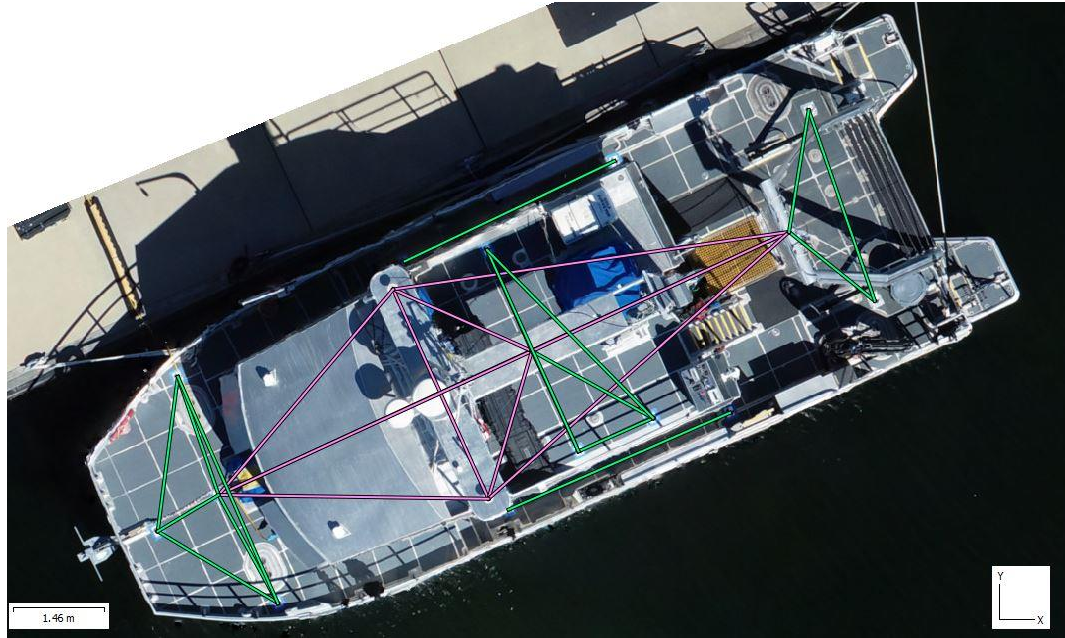
Figure 27: Orthomosaic of *R/V Gulf Surveyor* made from photographs taken on April 17, 2019. Purple polylines represent primary measurements, and green polylines represent secondary measurements.

Table 6: UAS SfM processing stages and settings.

UAS SfM Processing Action	Settings
Import Photographs	Remove irrelevant photographs
Alignment	Highest accuracy
	Key point limit of 40,000
	Tie point limit of 4,000
Import GCP file	Assign respective GCP coordinates
Optimiziation	f, cx, cy, k1, 2, k3, p1, & p2
Gradual Selection	Reprojection Error: Level 0.70
(Sparse Point Cloud Cleaning)	Reconstruction Uncertainty: Level 130
Build Dense Cloud	High quality
	Manual point cloud cleaning
Build Mesh	Source Data: Dense cloud or depth maps
	Surface Type: Arbirtary (3D)
	Face Count: High
Build Mesh Texture	Average or mosaic blending mode
Build DEM	WGS 84 UTM 19 N
	Source Data: Dense cloud or mesh
	Interpolation enabled
Build Orthomosaic	WGS 84 UTM 19 N
	Surface: DEM or Mesh
	Blending Mode: Average or Mosaic
Draw Polyline	Click on locations within orthomosaic

38

For all experiment days, 3D grid flight data were processed separately. All 31- and 21-meter 3D grid flights were processed individually to produce models made solely from a single 3D grid flight. Subsequently, each individual 3D grid dataset was processed with and without GCPs. The datasets processed with GCPs were done three times, once using the maximum number of GCPs in the coverage area (8-10), once with four, and once with three GCPs. Constructing models with more than the minimal amount of GCPs demonstrates the obtainable accuracies with a varying number of GCPs. Knowing, for example, if having three GCPs when calibrating a vessel with UAS SfM photogrammetry is as good as having 10 GCPs in terms of accuracy, could potentially cut down the time and cost of the survey.

Processing sections were also performed by combining multiple datasets to investigate whether combined flights affected the final accuracies of the model. For the first UAS experiment, the 31-meter grid flight was combined with the along and across track ellipses separately. An attempt was made at combining two 3D grids for the first experiment day, which resulted in a generation of two point clouds. 31-meter grid flights were also combined with a 21-meter oblique orbit for all individual experiment days in which an oblique orbit was flown.

Another section of processing included masking two individual flight datasets: a 21-meter grid flown on the first UAS experiment day and a 31-meter grid flown on the second UAS experiment day. Masking in Agisoft Metashape entails drawing a perimeter around the

area/object the user wants the software to include in the SfM algorithm, thus excluding the 3D content outside the defined boundary. This procedure was performed for every photo that contained any visual information of the *R/V Gulf Surveyor*. Masking to this extent allowed the software to execute its SfM algorithm solely based on the 3D location of the vessel. Without masking, it is theorized that the software, using this project as an example, anchors to the fixed land content of the pier. This could be problematic if the motion of the vessel exceeds a certain threshold over the duration of the mapping mission. As a result, major errors could be introduced into areas in the model that are of the vessel. Hence, masking of the vessel was carried out to determine if it limits the potential errors induced from this phenomenon. However, masking out content outside the *R/V Gulf Surveyor* meant that GCPs could not be used to georeference the model as the GCPs located on the pier were excluded in the masking process.

In total, over 30 sections of data were processed to produce dozens of point clouds, 3D meshes, DEMs, and orthomosaics. The processing procedures enabled sufficient data analysis to be performed. Shown in Table 7 are all models produced, along with what data was used to generate them.

Table 7: All models generated from the UAS processing workflow.

UAS Collection Day	Processing Classification
Wednesday, April 17, 2019 Vessel tied down tight	31m grid 21m grid 21 grid with Masks 31m grid with circle 31m grid with across track ellipse 31m grid with along track ellipse 31m grid (Eight GCPs) 31m Grid (Four GCPs) 31m Grid (Three GCPs) 21m grid (Eight GCPs) LiDAR
Wednesday, August 21, 2019 Vessel tied down loosely	31m grid 31m grid with masks 31m grid (10 GCPs)
Thursday, August 22, 2019 Vessel tied down tight	31m grid 21m grid 31m grid with circle 31m grid with IMU corrections 31m grid (10 GCPs) 31m grid (Four GCPs) 31m grid (Three GCPs) 21m grid (Eight GCPs)
Friday, August 23, 2019 Vessel tied down tight	31m grid 21m grid 31m grid with circle 31m grid (10 GCPs) 31m grid (Four GCPs) 31m grid (Three GCPs) 21m grid (10 GCPs)
Thursday, November 7, 2019	31m grid A (Vessel tied down loosely) 31m grid B (Vessel tied down loosely) 31m grid C (Vessel tied down tight) 31m grid A (10 GCPs) 31m grid B (10 GCPs) 31m grid C (10 GCPs)

2.5   UAS Lidar

2.5.1   UAS Lidar Data Collection

Since UAS lidar configurations are expensive and complicated to set up, an engineering firm called ARE was hired to complete a UAS lidar survey of the *R/V Gulf Surveyor* on April 17, 2019. ARE deployed a DJI Matrice 600 Pro to conduct the aerial lidar survey of the vessel. The DJI Matrice 600 Pro is an industrial grade UAS, equipped with three GNSS antennas with triple modular redundancy algorithms, an IMU with a dampening system, RTK positioning compatibility, and a mounting bracket (DJI, 2020). Attached to the Matrice 600 Pro was a Riegl miniVUX scanning system, capable of collecting 100,000 points per second, Figure 28. For non-vegetated areas, this system is capable of achieving nominal absolute accuracies of approximately 2-3 cm horizontal Root Mean Square Error (RMSE) and 4-6 cm RMSEz (ARE, 2019). To provide accurate Post Processed Kinematic (PPK) GNSS corrections to the Matrice 600 Pro trajectory, a CHC X900R static GNSS base station was set up on NGS control point AB2631, located just southwest of the survey site, as shown in Figure 29. Static GNSS observations on the control point began approximately half an hour before the lidar survey was conducted and concluded half an hour after the lidar mission ended. In addition to the base station, the ten AeroPoints, discussed in chapter 2.2.1 were present for the lidar survey to act as check points to the final georeferenced lidar model derived from the PPK UAS trajectory.

Figure 28: A DJI Matric 600 Pro being prepared to conduct a lidar survey at the UNH pier on April 17, 2019.

Figure 29: Location of the NGS control point utilized to conduct GNSS observations for post processing the DJI Matrice 600 Pro trajectory (NGS, 2020).

Calibration of the sensors on board the Matrice 600 Pro involved performing figure eight loops in the air close to the survey site. The flight pattern consisted of three lines parallel to the *R/V Gulf Surveyor's* along track direction, in addition to three lines parallel to the

vessel's across track orientation. This 3D grid pattern was repeated for multiple flying heights: 46-, 31-, and 16-meters AGL. To acquire minute detail on the vessel, one final pass was flown at 10-meters AGL parallel to the ship's across track direction. For the three passes following the ship along track direction, one line followed the centerline of the vessel, while the remaining two were offset from the centerline pass to capture detail on the sides of the vessel. Along track line lengths spanned the entire length of the pier, while lengths of the across track lines ranged from the North side of the pier to land directly South of the pier, Figure 29. Survey passes were flown at speeds between two and three meters per second resulting in approximately 120 points per meter squared directly underneath the aircraft's flight path over a single pass. In total, the survey took approximately 19 minutes to conduct, tallying 19 passes. Table 8 displays a detailed breakdown of the lidar flight pattern. It is hypothesized that the absolute accuracy from a single lidar pass is consistent over the few seconds it took to fly a single line. However, this hypothesis is less likely to be true across multiple passes due to the amount of motion the vessel could experience over the course of the Lidar survey (ARE, 2019).

Table 8: A breakdown of the lidar flight pattern performed by ARE (ARE, 2019).

Survey Pass Number	AGL Altitude (m)	Line Direction	Line Position
1	46	Stern to bow	Offset from center of vessel
2	46	Bow to stern	Centerline
3	46	Stern to bow	Offset from center of vessel
4	46	Port to starboard	Offset from center of vessel
5	46	Starboard to port	Centerline
6	46	Port to Starboard	Offset from center of vessel
7	31	Starboard to port	Offset from center of vessel
8	31	Port to starboard	Centerline
9	31	Starboard to port	Offset from center of vessel
10	31	Stern to bow	Offset from center of vessel
11	31	Bow to stern	Centerline
12	31	Stern to bow	Offset from center of vessel
13	15	Bow to stern	Offset from center of vessel
14	15	Stern to bow	Centerline
15	15	Bow to stern	Offset from center of vessel
16	15	Starboard to port	Offset from center of vessel
17	15	Port to starboard	Centerline
18	15	Starboard to port	Offset from center of vessel
19	10	Port to starboard	Centerline

2.5.2   UAS Lidar Data Processing

Initial processing of the lidar and associated GNSS observations were performed by ARE.

Novatel Inertial Explorer v8.70 was used to perform the post processing of the aircraft

trajectory, while a different program was used to process/clean the lidar data. Scan angles

for the lidar data were left at ± 90 degrees from the nadir beam so that the lower altitude

passes would enable data returns from higher angles. The lidar datasets were produced to

meet the American Society of Photogrammetry and Remote Sensing (ASPRS) "Positional

Accuracy Standards for Digital Geospatial Data" (2015) for a 2.5 (cm) RMSEx / RMSEy

Horizontal Accuracy Class, which is equivalent to a Positional Horizontal Accuracy equal

to ±6.1 cm at a 95% confidence level (ARE, 2019). Additionally, these datasets were

produced to achieve ASPRS Positional Accuracy Standards for Digital Geospatial Data

(2015) for a 5 cm RMSEz Vertical Accuracy Class equating to a Non-vegetated Vertical Accuracy (NVA) equal to ±9.8cm at 95% confidence level and a Vegetated Vertical Accuracy (VVA) equal to ±15cm at the 95th percentile. ARE's RMSEz calculations against the nine AeroPoints in the coverage area demonstrate an RMSEz value of 1.006 cm (ARE, 2019). Final deliverables received from ARE included the trajectory results, lidar LAS files, and a report summarizing the survey. The LAS files were provided in the State Plane Coordinate System of 1983 (SPCS83) (NAD83 (NSRS2007)), New Hampshire zone, FIPS 2800, with units of US survey feet (sft) and orthometric heights in NAVD88 (Geoid12B) US survey feet.

To further analyze the accuracy of the lidar dataset, the LAS files were brought into Global Mapper. Similar to the UAS SfM data, the method chosen to assess the accuracy of the UAS Lidar survey was to compare it to the ground truth survey. Comparing the UAS lidar model of the *R/V Gulf Surveyor* to its ground truth laser scan survey began with accurately identifying monument locations in the observed point cloud. The original LAS files did not contain true color values, and non-RGB point clouds make it extremely difficult to accurately identify minute features within the point cloud. Images taken from the lidar equipped UAS for the purpose of colorizing the point cloud were not requested to be in the original deliverable package from ARE. Therefore, images collected from the UAS SfM flights, which were conducted after the conclusion of the lidar survey, were utilized to colorize the LAS files. It is important to note that for this type of survey it would be ideal to collect imagery and lidar data simultaneously on board the same platform/aircraft. For a UAS vessel calibration survey, the object of interest is slightly moving, so if the lidar and

imagery are collected at separate times the vessel could experience different changes in orientation between the two types of data collection, causing potential for errors to be introduced in the colorization of the point cloud. This phenomenon will affect the uncertainty of the lidar model.

Inside Global Mapper, a GeoTIFF of an orthomosaic derived from the April 17, 2019 31-meter AGL flight processed with three GCPs, was overlaid onto the lidar point cloud. Both the orthomosaic and lidar data were set to reference NAD83 (NSRS2007) / SPCS83, New Hampshire US survey feet (sft) as this was the datum that the final deliverables from ARE were referenced to. The 2D viewer was used to verify that the orthomosaic lined up with the location of the lidar data. A tool called "Apply Color to Lidar Points" was selected to colorize the lidar data using the overlaid orthomosaic, Figure 30. After colorization, the 3D viewer was used to verify that the color from the orthomosaic was properly transferred to the respective positions on the lidar point cloud. To prepare the lidar model for accuracy assessment, polylines were drawn in the 2D viewer between the centers of the vessel targets, Figure 31.

Figure 30: The true color lidar point cloud of the *R/V Gulf Surveyor* in Global Mapper.
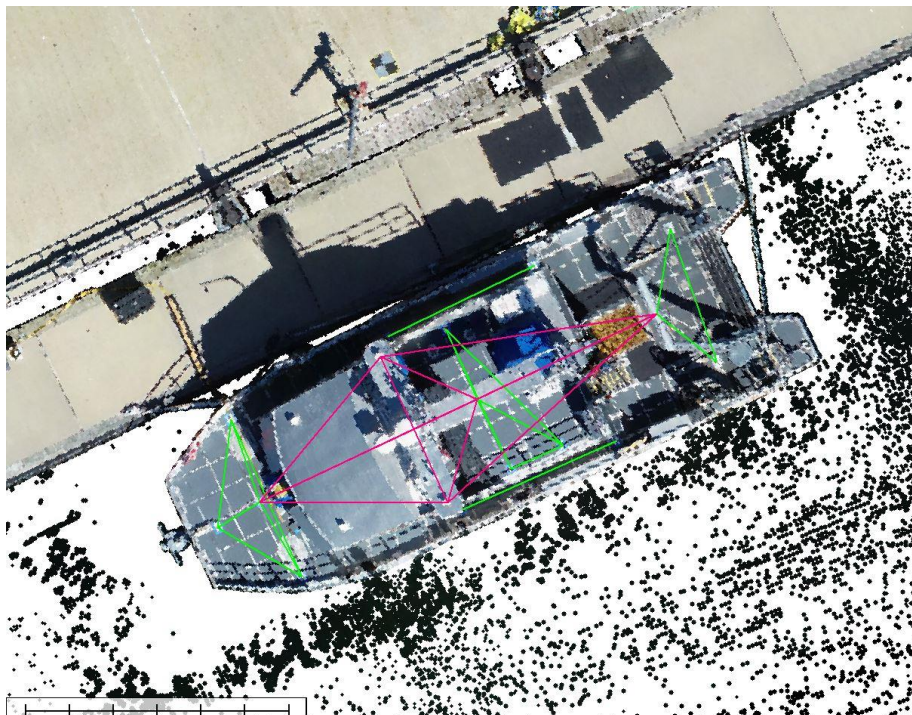
Figure 31: 2D view of the true color lidar point cloud with primary (purple) and secondary polylines (green).

2.6 Horizontal Error Estimation: UAS Surveys

2.6.1 General Error Estimation

General horizontal deviation estimates for the UAS lidar and SfM models were calculated by taking the distances between vessel targets in the observed models and subtracting them from the respective ground truth lengths, Figure 32. In doing this, only the total baseline lengths between targets were compared since the observed measurements were originally output to either WGS84 or NAD83 for the SfM and lidar data respectively, and not the defined SRF. Comparisons between the ground truth and observed models were broken up into primary and secondary forms. Primary comparisons involved the differences between the ground truth laser scanned monument distances and the observed UAS lidar/SfM monument distances. Secondary comparisons were between the ground truth fiberglass tape measurements of vessel targets and the observed UAS lidar/SfM vessel target distances. The laser scan survey took priority as the primary ground truth source due to its higher accuracy measurements compared to the fiberglass tape distances, which have a slightly higher uncertainty per measurement. Consequently, primary comparisons most likely represent the best-estimated horizontal deviations from the ground truth.
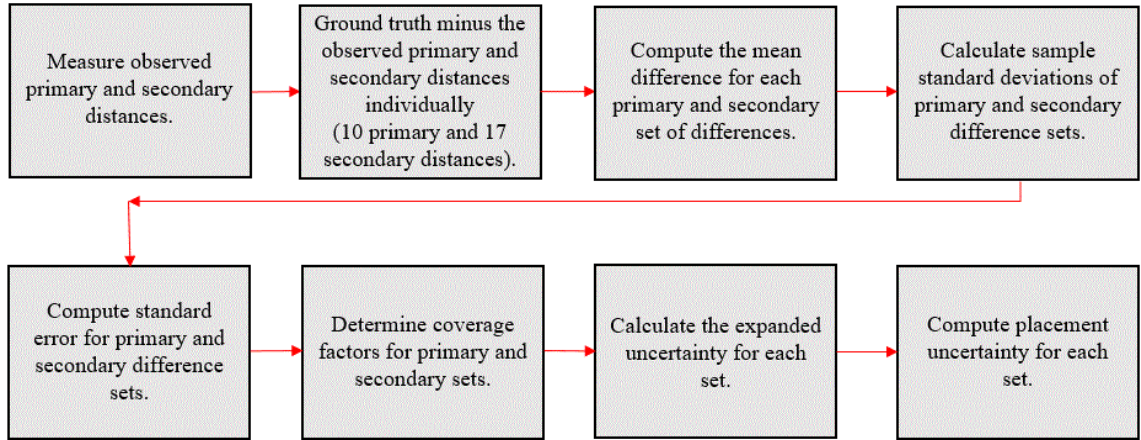
Figure 32: General workflow implemented to estimate the horizontal deviations from ground truth of the UAS surveys.

Acquisition of primary and secondary observed measurements were taken from the final deliverables of the observed models. For the lidar model, distances were taken from the polygonal chains, defined as polylines in Global Mapper, between vessel targets in the 2D viewer of Global Mapper. However, necessary measurements for the UAS SfM models came from the polylines marking the distances between vessel targets in the orthomosaics. In total, there were 10 primary baselines and 17 secondary baselines for each observed model. Recorded Euclidean distances from all models were brought into a code as baseline lengths for horizontal error estimation. Differences between the observed primary/secondary components and their ground truth counterparts were computed along with the average differences for each component set. Each processed model possesses one set of primary differences and one set of secondary differences. A sample standard deviation was computed for each respective set of differences followed by the calculation of standard errors, (1) and (2).

$$\sigma = \sqrt{\frac{\Sigma(X-\overline{X})^2}{n-1}} \tag{1}$$

$$SE = \frac{\sigma}{\sqrt{n}} \tag{2}$$

From nine and 16 degrees of freedom the 95 percent coverage factors were found for both primary/secondary sets: 2.262 and 2.120. The expanded uncertainty for each model was calculated by multiplying the respective standard error by the proper coverage factors, (3).

$$U = SE \cdot CF \tag{3}$$

To compute the uncertainty in placing the center point of the targets, a derivative of Pythagorean's Theorem was taken and put through (4), with further simplification leading to the target placement uncertainty equation, (5).

$$\sigma^2 = \left[\left(\frac{dDistance}{d\Delta x}\right)^2 \sigma_{\Delta x}^2\right] + \left[\left(\frac{dDistance}{d\Delta y}\right)^2 \sigma_{\Delta y}^2\right] \tag{4}$$

$$\sigma^2 = 2\sigma_p^2 \tag{5}$$

Two sets of plots were created to visualize the estimated horizontal deviations from the ground truth based on the primary and secondary components of each model. The mean differences between the sets of ground truth and observed distances along with the expanded uncertainties of the sets were plotted. These plots provide useful information on the general deviation patterns occurring from specific datasets utilized to generate the finished models.

Initial deviation estimates provide a general indicator in quantifying what the horizontal deviations of the UAS surveys are; however, more can be learned about the deviation estimates by employing an additional procedure. Without the observed target coordinates being in the same coordinate system as the ground truth monuments, Cartesian components of the baselines cannot be compared, thus directionality of the deviations cannot be determined. Therefore, steps were taken to transform observed coordinates into the SRF and perform this type of analysis.

2.6.2 Error Estimation Using Ship's Reference Frame (SRF) Coordinates

Similar to the ground truth survey of the *R/V Gulf Surveyor,* typical practices for calibrating a vessel with traditional survey techniques entails establishing an SRF for the designated vessel. Hence, as a part of the exploration into the proposed UAS approaches, it is essential to outline the necessary procedure for establishing SRFs when implementing UASs to calibrate vessels. In this case the collected datasets that resided in either WGS84 or NAD83 were transformed to the *R/V Gulf Surveyor's* already established SRF. An affine transformation from projected coordinates (e.g. WGS84 UTM 19N for the SfM data and from NAD83 (NSRS2007) / SPCS83, New Hampshire for the lidar data) was performed utilizing the SRF monuments as reference markers. Knowing the distances between monuments on the *R/V Gulf Surveyor* helped in translating the coordinates in reference to the correct SRF origin. However, if a UAS is being used to establish a new SRF for a vessel, an origin that could be seen in the point cloud would simply be selected. A detailed breakdown of the transformation procedure to the SRF can be seen in Figure 33. Executing

the transformations into the SRF enabled explicit comparisons between the ground truth and observed SRF coordinates.
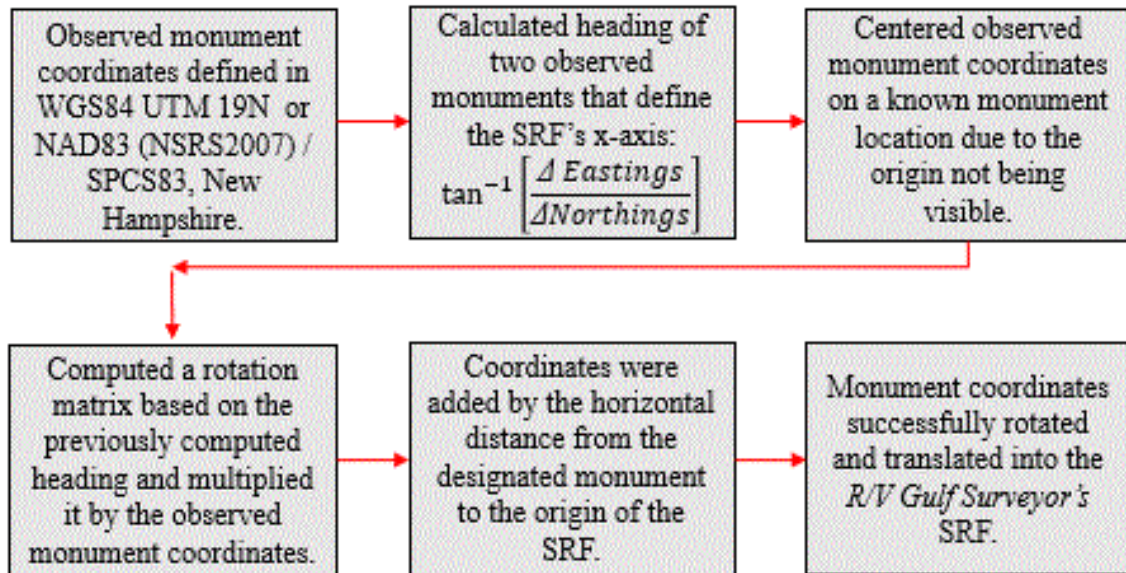
Figure 33: Diagram showing the stages required to transform vessel monuments from geographic to SRF coordinates.

Determination of the observed horizontal SRF coordinate accuracies were performed by explicitly comparing the observed to the ground truth SRF coordinates. The Euclidian distances between monuments, Cartesian deviation vectors, and deviation magnitudes for each baseline were calculated. Consequently, the deviation vectors for each baseline were output with respect to the SRF. By referencing the deviations in the SRF, directionality of the deviations could be visualized, thus demonstrating any directional deviation biases. The deviation magnitudes were also output in reference to the SRF and are similar values to those obtained in the general horizontal deviation estimation process, except that the deviation magnitudes are positive. Possessing the individual Cartesian baseline lengths not

only helps in analyzing the directionality of the deviations, but it provides additional information necessary to investigate the scales of each observed baseline.

Exploring the scale of each baseline reveals useful information pertaining to how the scale changes throughout the observed models. Absolute scales, S_x and S_y, for each Cartesian baseline were obtained from (6) and (7).

$$S_x = \left| \frac{L_{x\ Observed}}{L_{x\ Ground\ Truth}} \right| \tag{6}$$

$$S_y = \left| \frac{L_{y\ Observed}}{L_{y\ Ground\ Truth}} \right| \tag{7}$$

As a result, a scale value under one represents under scaling and values above one represent over scaling. Possessing Cartesian deviations and scales of SRF baselines enables thorough analysis of what is occurring in the observed models.

2.7 Seafloor Reference Methods

2.7.1 Seafloor Reference Data Collection

Similar to the UAS methods, multiple pieces of equipment were employed to determine the capabilities of different SBES systems to calibrate horizontal vessel lever arms. Two independent systems, one survey and one consumer grade, were set up on the *R/V Gulf Surveyor* to test the single-beam seafloor reference method. The survey grade setup integrated an Echotrac CV200 SBES with a POS MV 320 MRU. RTK positioning was performed throughout the survey by utilizing the Massachusetts CORS network. For the

consumer grade setup, the TCB system demonstrated in Calder et al. (2020) was utilized. The TCB system is comprised of a SeaID GNSS data logger connected to a Harxon GNSS antenna. In this instance, the SeaID logger was integrated with a Garmin SBES with both GNSS and depth data being recorded on the SeaID data logger. HYPACK was used to record positioning data from the POS MV 320 and depths from the CV200, and as a secondary collector of the Garmin single-beam data. Offsets of each echo sounder in the SRF were input in HYPACK in a way that enabled them to be turned on and off for processing purposes. Having the horizontal offsets originally defined as zero would theoretically place the surveyed feature at distances approximately equal to the vessel's horizontal offsets, enabling the vessel's horizontal offsets to be estimated.

Sufficient survey lines over a distinct feature were necessary to properly test the capabilities of the proposed SBES seafloor reference method. Capturing a feature's vertical relief from multiple angles with a SBES is crucial because if there is a horizontal offset between the observed and true data, a vertical feature will show the horizontal displacements between the two datasets, unlike flat terrain. A survey line perpendicular to the vertical relief of a feature potentially shows the vessel's x-axis, along track, offset. However, determining the y-axis, across track, offset is more difficult making running just one line likely insufficient. Hence, two y-offset calibration lines that intersect the defined edge of a feature at approximately 45° angles were performed. The three proposed survey lines were all performed in two opposing directions at under six knots and were implemented for two distinct features in the Piscataqua River previously mapped with a MBES, Figures 34 and 35. Sound speed profiles were taken at each survey site with a

Teledyne Odom-DigibarPro, while water level predictions for Fort Point, New Hampshire were retrieved from the NOAA Tides and Currents tidal prediction website. Draft measurements of the vessel were estimated based upon previous measurements.
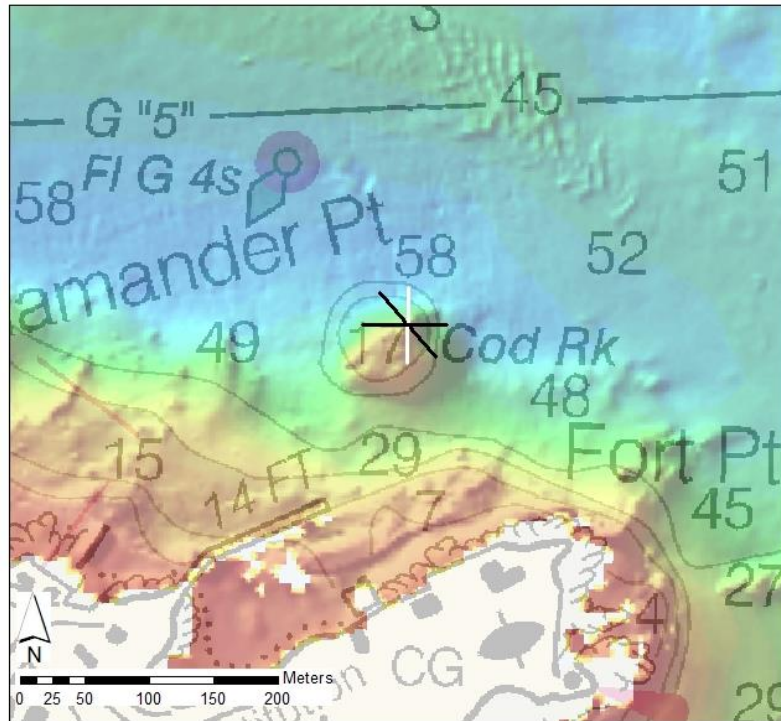

Figure 34: Survey lines performed over Cod Rock in the Piscataqua River with black lines representing the y-axis offset calibration and the white line representing the x-axis offset calibration.
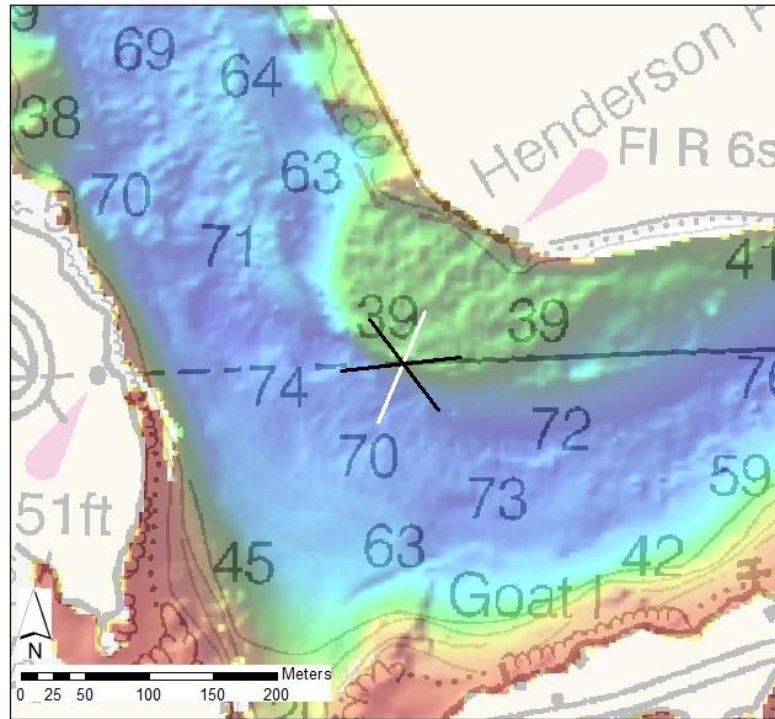
Figure 35: Survey lines performed over Henderson Point in the Piscataqua River with black lines representing the y-axis offset calibration and the white line representing the x-axis offset calibration.

2.7.2   Seafloor Reference Data Processing

All single-beam datasets were post processed in the HYPACK single-beam editor. Noisy data were removed and sound speed, heave, and water level correctors were applied. Additionally, all horizontal and vertical offsets to the single-beam transducers were set to zero in the corrector process, hypothetically placing the seabed data horizontally displaced from its actual locations by the true horizontal offsets. Course over ground (°), heading (°), northing (m), easting (m), and corrected depth (m) were exported for each point in each line.

Having reference data to compare to the observed seabed measurements is crucial to the execution of the single-beam seafloor reference method. In this case, the selected ground truth data came from the NOAA Survey H11014. This survey was performed in 2000 by the NOAA Ship Whiting, with a Reson 8101, at a frequency of 240 kHz (NOAA NCEI, 2020). The features selected from this survey were of a highly stable nature, ensuring repeatability of the results. A CARIS HIPS project containing the corrected sounding data from this survey was used to generate individual gridded surfaces for Cod Rock and Henderson Point at a one-meter resolution. To visually compare the reference surfaces to the observed single-beam points, all relevant files were brought into Fledermaus. Before attempting estimation of the horizontal vessel offsets, it was important to resolve any vertical displacements between the datasets. The offset tool in Fledermaus was utilized to obtain the vertical offsets between the two datasets. The vertical offsets were then applied to the respective observed single-beam datasets to vertically align the data with the reference surfaces, thus leaving just horizontal offsets between the datasets, Figure 36.
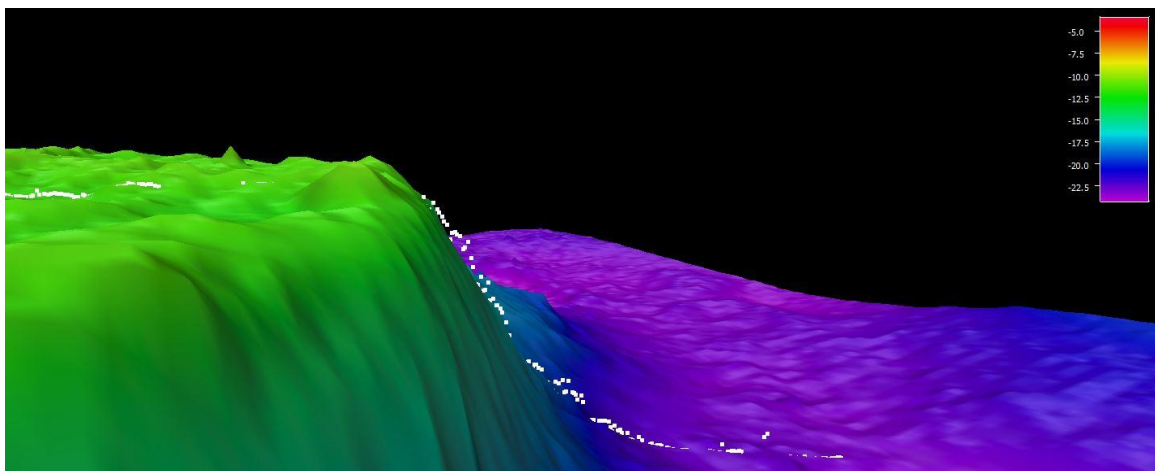

Figure 36: The Henderson Point reference surface overlaid with the horizontally displaced observed single-beam data (white).

The reference surfaces were interpolated, enabling direct comparison to 3D coordinates of the observed single-beam points. Figure 37 shows the procedure implemented to estimate horizontal vessel offsets from the seafloor reference technique. A grid search optimization, an algorithm that methodically evaluates combinations of estimated parameters in a grid format (Paul, 2018), was created to estimate the offsets. In the algorithm, the horizontally shifted single-beam profiles were compared to the respective reference surface by taking the sum of the squares of the residuals of elevations between the two datasets, with the most closely matching shifted profile indicating the estimated horizontal offsets between the two datasets. The x and y shifts corresponding to the lowest sum of the squares of the residuals value were selected from the grid search algorithm as the estimated horizontal vessel offsets. This procedure was done on just the CV200 single-beam data.

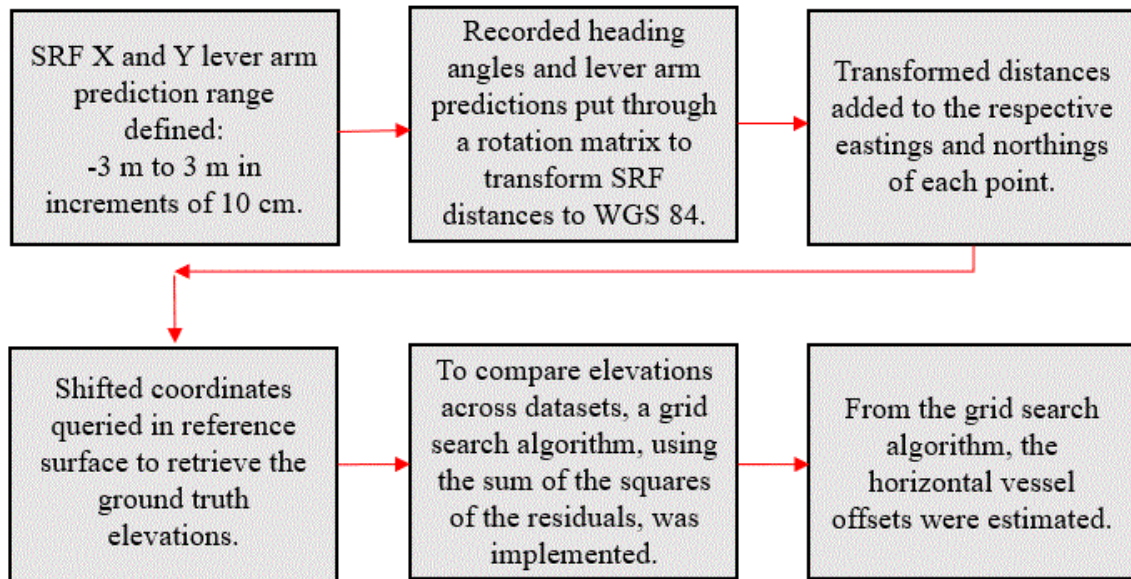Figure 37: Procedure used to estimate horizontal vessel offsets for the seafloor reference method.

Errors in lever arm approximations were obtained by comparing the ground truth SRF lever arms of the single-beam transducer, (x,y) = (2.345, 1.294) m, to the estimated offsets. Estimated offsets were subtracted from their ground truth distances to determine the accuracies associated with the lever arm approximations.

CHAPTER 3

RESULTS

3.1   Horizontal Error Estimates: UAS Surveys

3.1.1   Vessel Motion Analysis

Initial flights were conducted during a period of high tidal change, resulting in feature duplication within the point cloud when combining two separate photogrammetry flights, Figure 38. This discovery indicates a vertical displacement threshold Agisoft Metashape can withstand before generating multiples of the same feature. To further investigate this phenomenon, water level plots were inspected to help determine how much vertical displacement the vessel experienced over the course of the UAS surveys. Figure 39 demonstrates that the UAS surveys were conducted when the tide was shifting from high to slack tide on the first day of experimentation. The amount of water level change between the end of each flight was approximately 70 cm, matching the vertical offset between the two point clouds. To eliminate this phenomenon, all other surveys were conducted within a two-hour window of high or low tide, limiting the vertical displacement of the vessel to under 10 cm over the course of all surveys for each day.
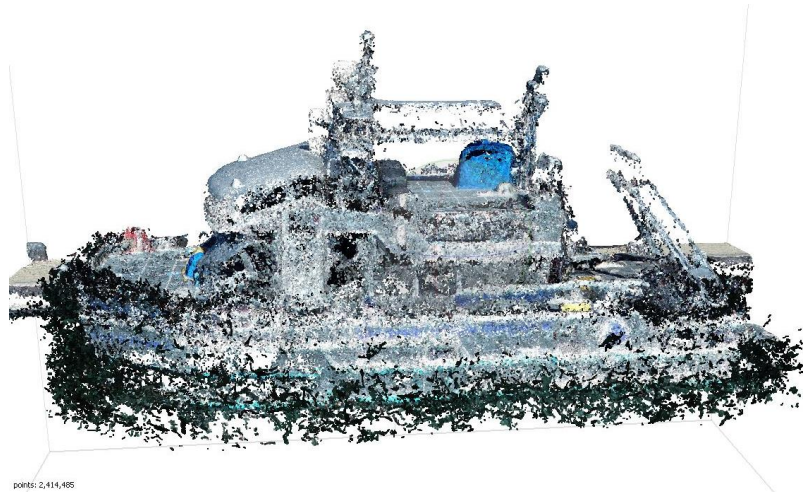
Figure 38: Point cloud generated from two 3D grid flights collected on April 17, 2019

Figure 39: NOAA water level plot at Fort Point, New Hampshire during the April 17, 2019 UAS survey (NOAA, 2020). The red box represents the approximate time of the surveys.

Similar to the vertical displacement discovery, it was noticed after conducting a flight with a loose vessel configuration that visual distortions were present in the resulting orthomosaic, Figure 40. However, orthomosaics generated from tight vessel configurations resulted in smooth, sharp composite images, Figure 41. Given that the distortions were appearing in loose vessel setups; it was suspected that the local vessel motion may have been causing the blurriness in the orthomosaics. To further investigate this phenomenon, the MRU data collected on board the vessel while the UAS surveys were being conducted, were analyzed.
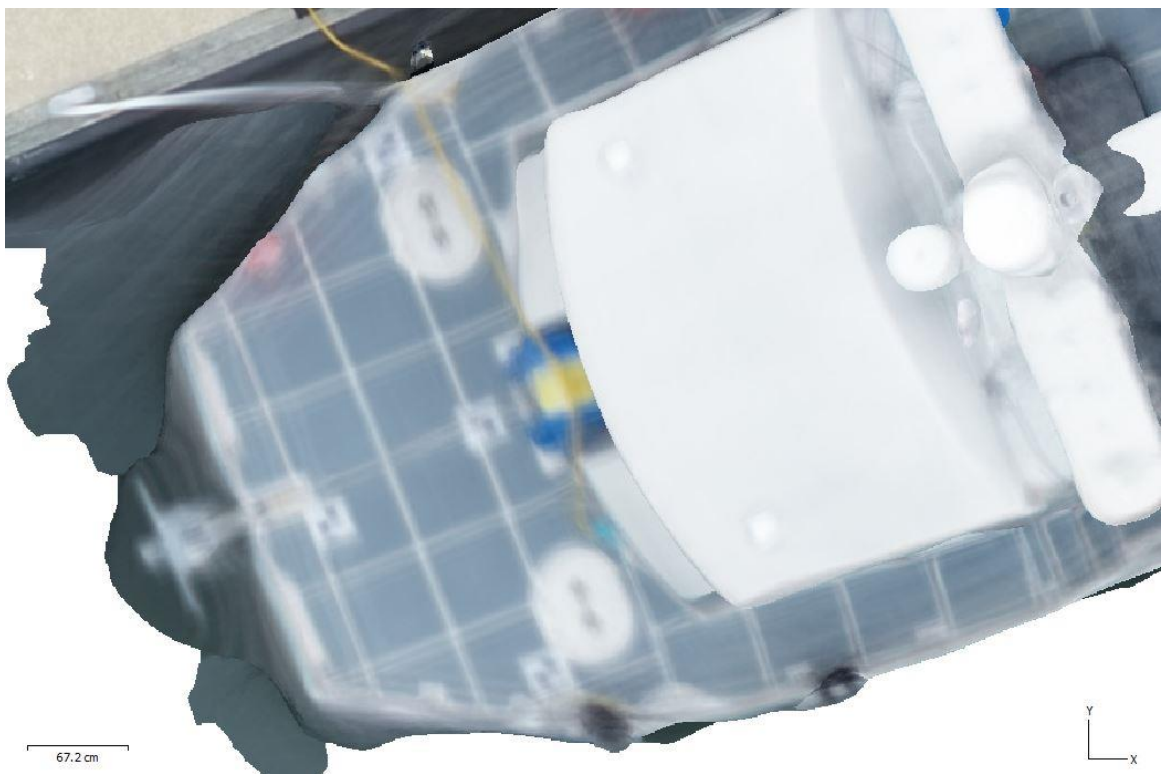

Figure 40: Orthomosaic generated from data collected with the *R/V Gulf Surveyor* loosely tied down on August 21, 2019.
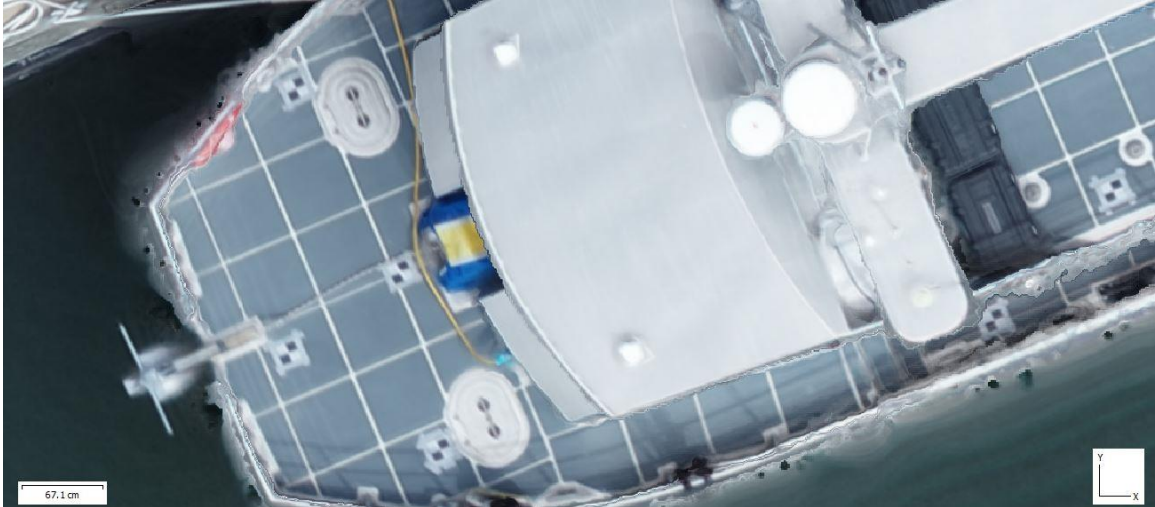
Figure 41: Orthomosaic generated from data collected with the *R/V Gulf Surveyor* tightly tied down on August 23, 2019.

When looking at an attitude time series plot of the vessel during one tie down setup, Figure 42, it is difficult to discern which attitude properties significantly change when moving from a loose to tight vessel tie down setup. However, Figure 43 demonstrates that heading experiences the most change out of the three measurements when transitioning from a loose to tight vessel tie down system. Further analysis of the heading change demonstrates that there is a significant difference between each tie down configuration. Figure 44 displays a 15-second interval heading change range of -0.6° to 0.6° for a tight vessel setup, while Figure 45 shows a -1° to 1° heading change range for a loose vessel configuration. Both ranges remain generally consistent for all other respective datasets, Appendix A. These figures demonstrate the degrees of attitude motion, but they do not quantify how much distance the vessel moved during the surveys.
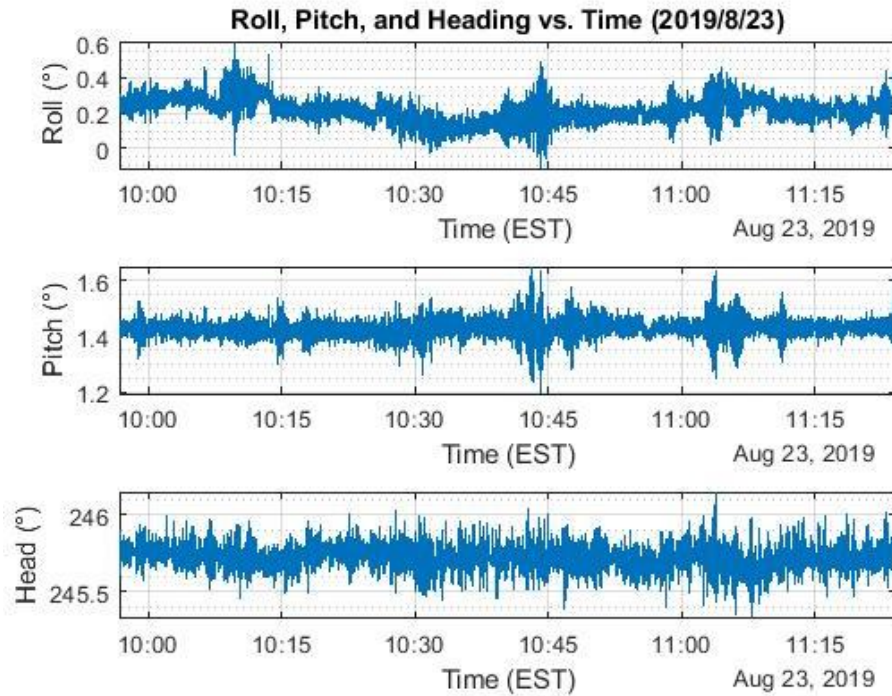
Figure 42: Roll, pitch, and heading time series of the *R/V Gulf Surveyor* tightly tied down on August 23, 2019.

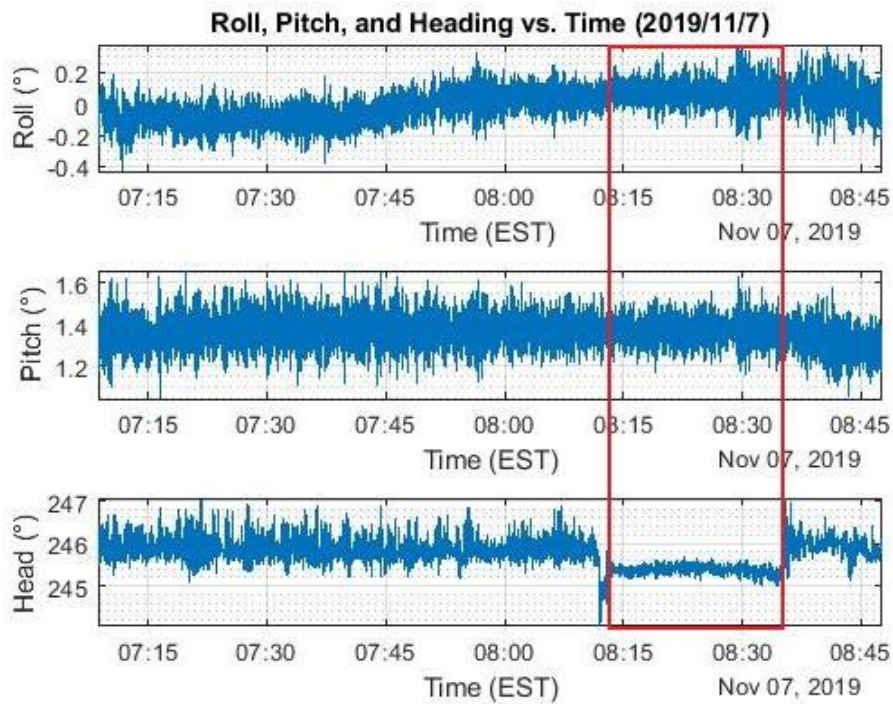Figure 43: Roll, pitch, and heading time series of the *R/V Gulf Surveyor* loosely and tightly tied down on November 7, 2019. The red rectangle represents the time in which the vessel was tied down tight.
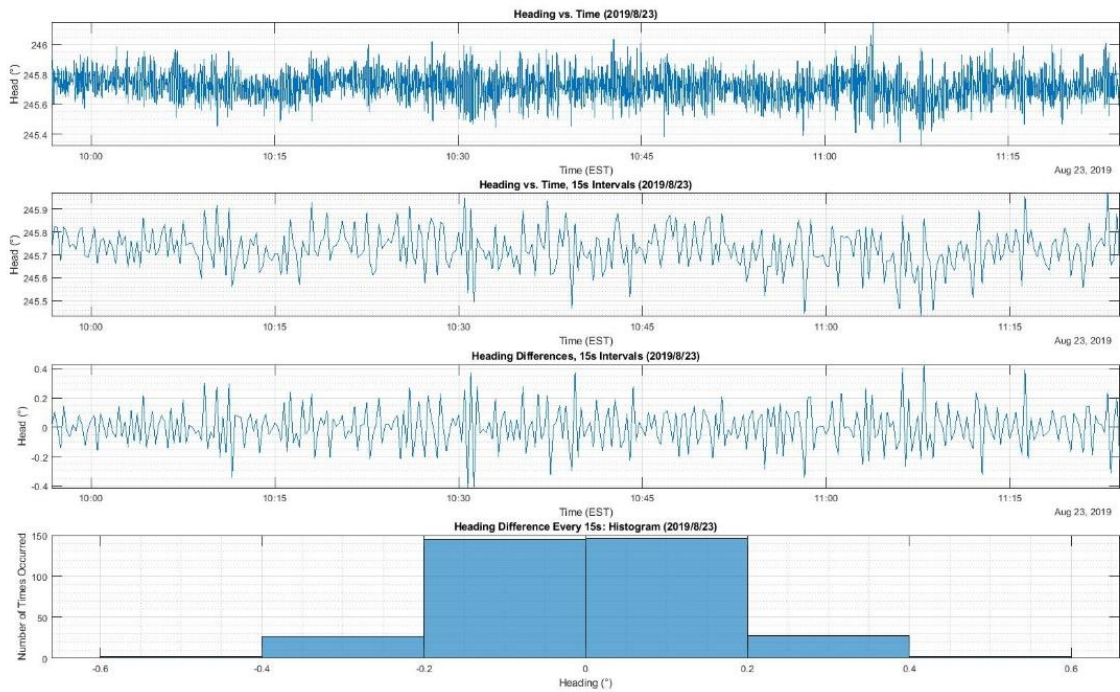
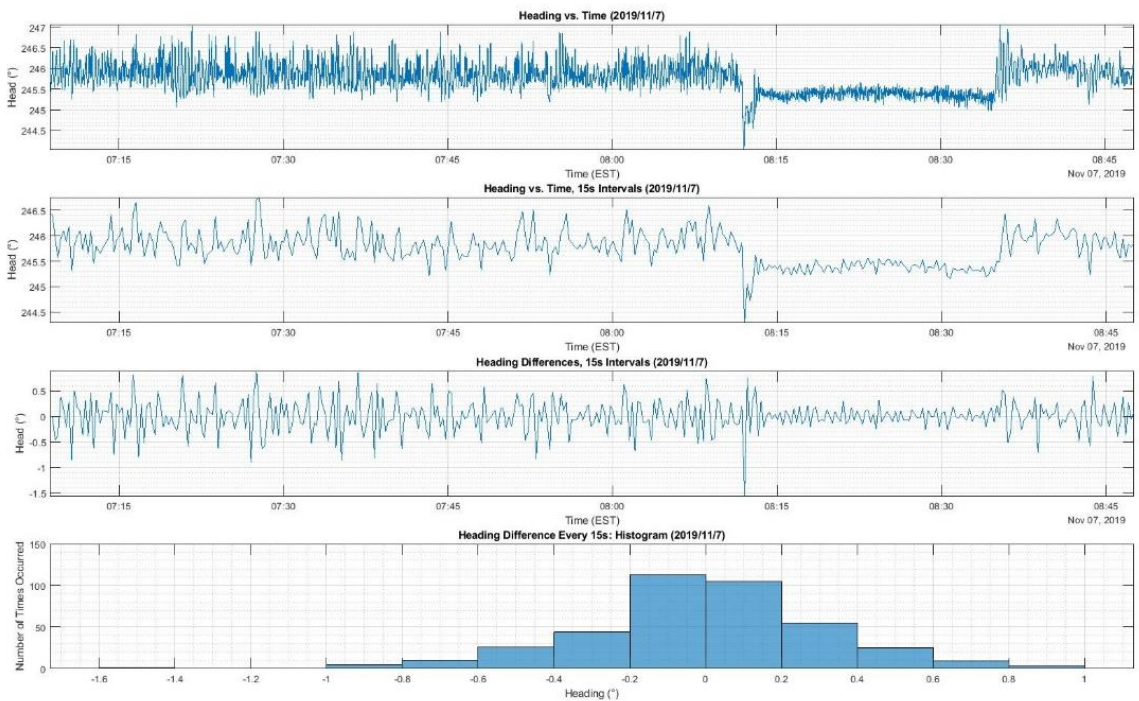Figure 44: Heading plots of the *R/V Gulf Surveyor* tightly tied down on August 23, 2019.

Figure 45: Heading plots of the *R/V Gulf Surveyor* loosely and tightly tied down on November 7, 2019.

The pixel shift code discussed in chapter 2.3.2 was created to quantify how much the local vessel motion impacted the quality of the UAS surveys. Recorded attitude changes of the vessel were used in this code to compute how much the vessel moved over a defined time interval. The code generated plots displaying how much the vessel shifted in distance and pixels at a defined 3D (X, Y, Z) point, [7.164, 0, -0.439] m, in the SRF. This point was chosen due to it being a ground truth SRF monument.

Based on the flight plan properties for the SfM flights, approximately 10 photographs were taken every 15 seconds. Figure 46 shows that during a tightly tied down vessel configuration the distance shifts every 15 seconds were under 7 cm, which are consistent with other analogous datasets, Appendix A. A similar value can be seen when the vessel was tied down tight for a different survey between 0815 to 0835 EST in Figure 47. However, in the remaining time spans where the vessel was tied down loosely within the same survey, distance shifts were between 5 cm and 20 cm, consistent with all other datasets collected under similar conditions, Appendix A. This means a loose vessel setup resulted in 3D distance displacements between 5 cm and 20 cm over 10 photographs. Given the discovery that heading was the most contributing factor to the vessel's attitude change, it was logical to conclude that changes in the vessel's heading caused this significant movement. In addition, it can be concluded that heading change is responsible for inducing the blurriness in the orthomosaics produced from loosely tied down vessel configurations.
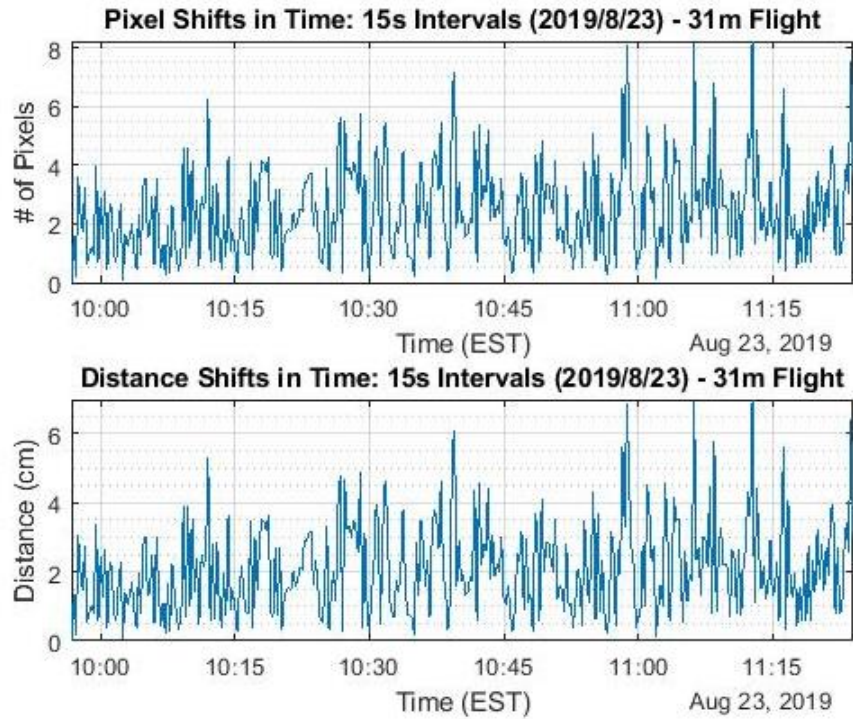
Figure 46: Pixel and distance shifts the tightly tied down *R/V Gulf Surveyor* experienced during the August 23, 2019 UAS surveys.
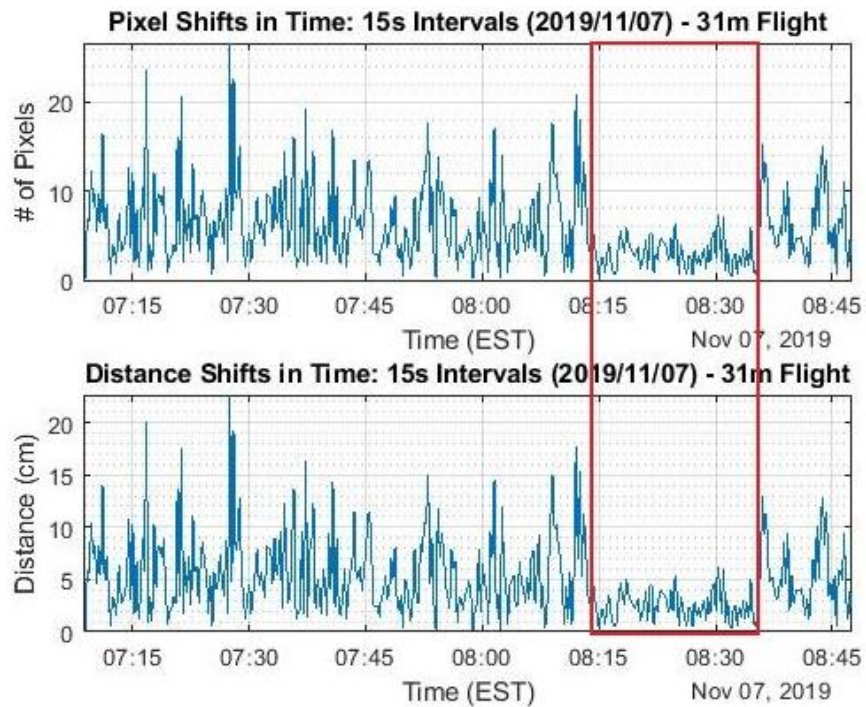

Figure 47: Pixel and distance shifts the *R/V Gulf Surveyor* experienced during the November 7, 2019 UAS surveys. The red rectangle represents the time in which the vessel was tied down tight.

3.1.2 Error Analysis

Figure 48 displays the estimated horizontal deviations for all processed datasets in which the primary ground truth data was utilized. From this figure it can be seen that the SfM models without GCPs consistently result in decimeter level and sometimes centimeter level deviation ranges. SfM models processed with GCPs experience deviation ranges on the centimeter level. Both average distance differences and deviation ranges, in most cases, lessen when GCPs are implemented. These observations demonstrate that GCPs will result in consistent UAS survey qualities for this application, while non-GCP models can produce, at times, inconsistent results. Logically, this is due to the lesser quality of the UAS GNSS receiver compared to the survey grade quality GCP observations. Higher quality GNSS observations could result in more reliable scaling of the models, which is exhibited in the primary deviation estimations in this thesis. In addition, the deviations indicate no significant change between different flying heights and when going from implementing the maximum number to three or four GCPs.
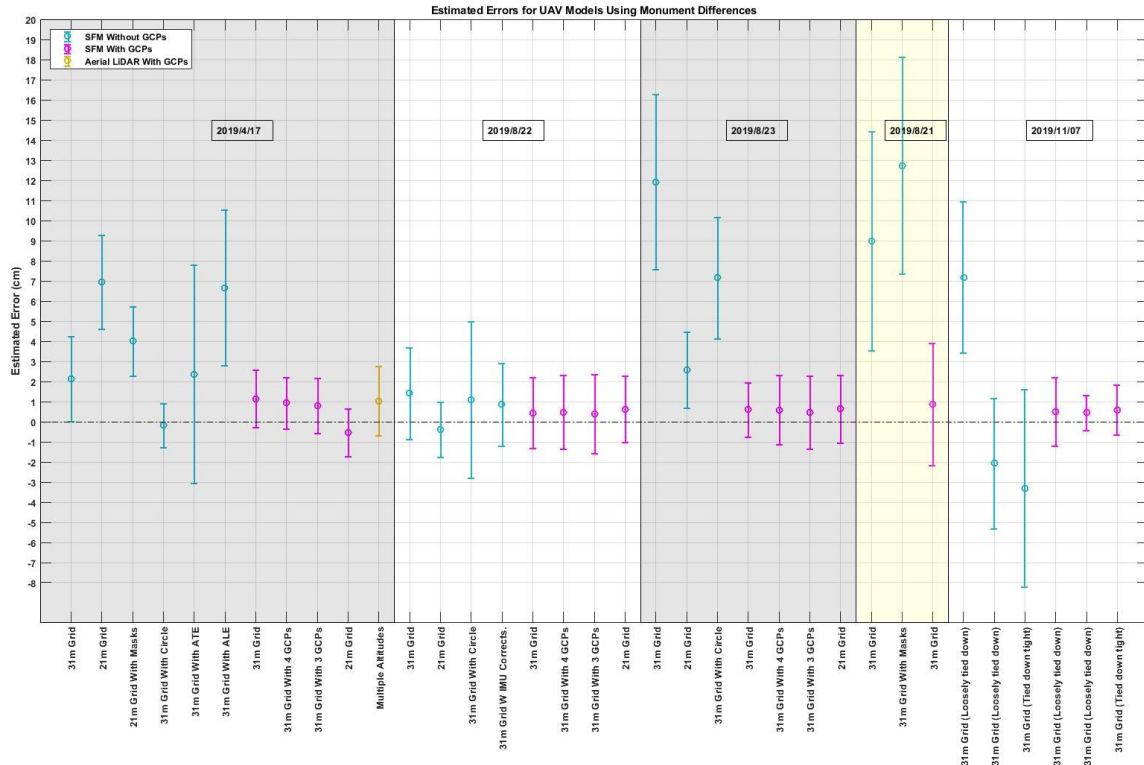
Figure 48: General deviation estimates for all UAS surveys utilizing the primary source data as ground truth.

The last two sections of data in Figure 48 represent loosely tied down vessel configurations, unless otherwise specified. These models mostly possess higher deviation ranges compared to their tight vessel configuration counterparts. This phenomenon is caused by the heading change of the vessel while being tied down loosely. When GCPs are implemented in this scenario the deviation ranges shrink significantly. Additionally, the lidar survey resulted in similar centimeter level deviation ranges as the SfM datasets. Inconsistent effects on deviation ranges without GCPs were experienced when combining oblique orbits with nadir grids. The two masked datasets resulted in opposing effects: lowering of deviation range for a tight vessel configuration and increasing of deviation range for a loose vessel

configuration. Analogous result patterns are experienced for deviation estimates achieved

when comparing observed measurements to secondary ground truth data, Figure 49.
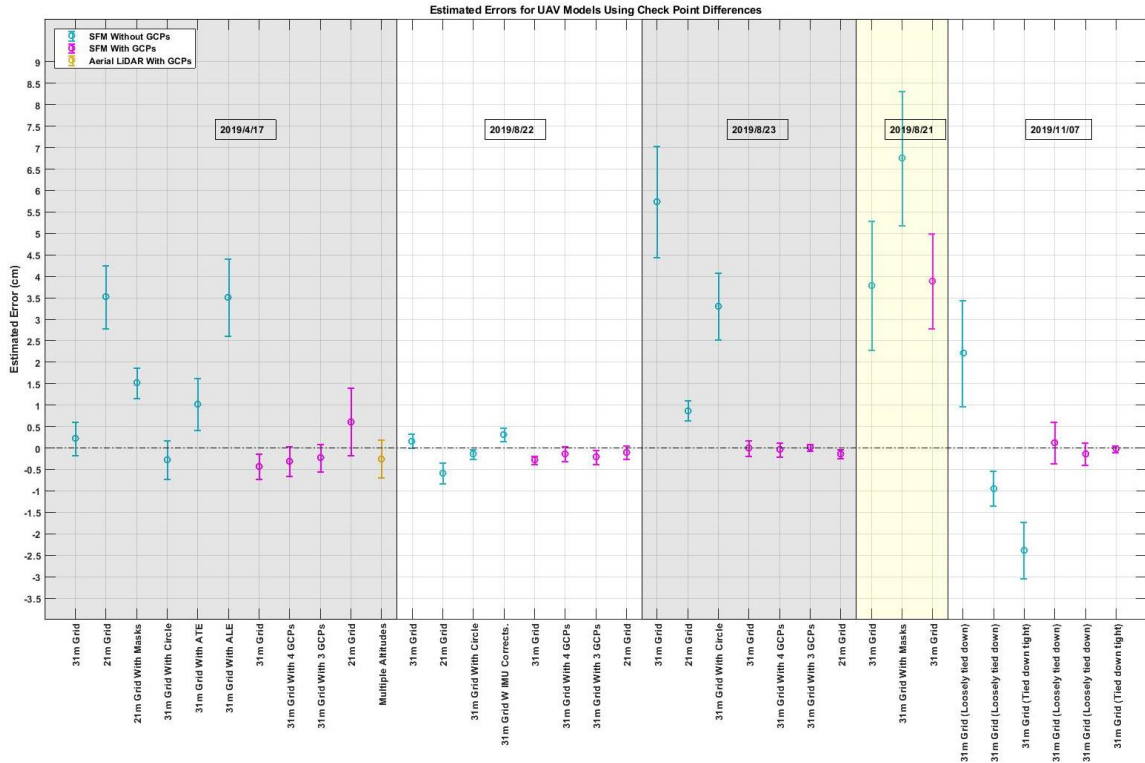

Figure 49: General deviation estimates for all UAS surveys utilizing the secondary source data as ground truth.

Diagrams such as Figures 50 and 51 demonstrate the size and direction of the deviations

when utilizing primary ground truth data. These plots demonstrate a tendency for the

deviations to point towards the starboard side of the vessel where the pier is located. It is

logical to believe this is happening for the GCP tight vessel datasets because the control

network is located on the pier, to the starboard side of the vessel. Similar datasets without

GCPs show analogous, but not as dominant directional biases, suggesting a slight deviation

bias towards fixed content in the form of the pier. These tendencies appear consistent

throughout all datasets with tight configurations, Appendix B, but not with loose setups. Figures 52 and 53 not only show larger errors than tight vessel configurations, but also suggest a more randomly distributed deviation direction pattern when implementing GCPs. Results from the motion analysis indicate that the vessel motion is responsible for these occurrences. A similar random deviation directionality can be seen in a masked dataset, Figure 54. When masking, data was processed solely by focusing on the geospatial content of the vessel and not incorporating the fixed pier data, explaining why the deviations are not directionally biased towards the pier. However, this does not explain the random directional deviations associated with datasets where the vessel was tied down loosely. The motion analysis suggests the induced motion of the vessel is responsible for this phenomenon.
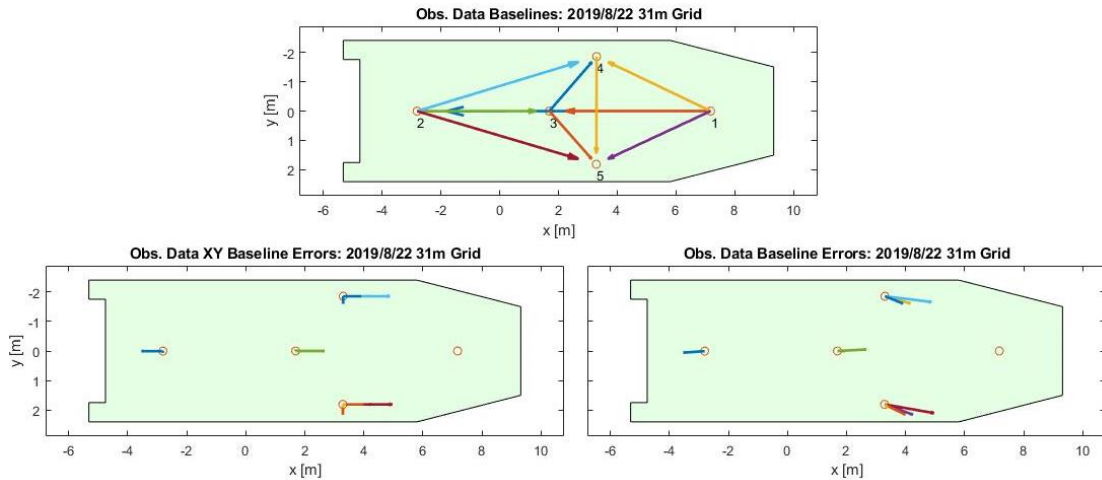

Figure 50: SRF baseline lengths (top), error vectors (left), and polar errors (right) of a 31 m grid dataset flown on August 22, 2019. Errors are scaled by a factor of 30.
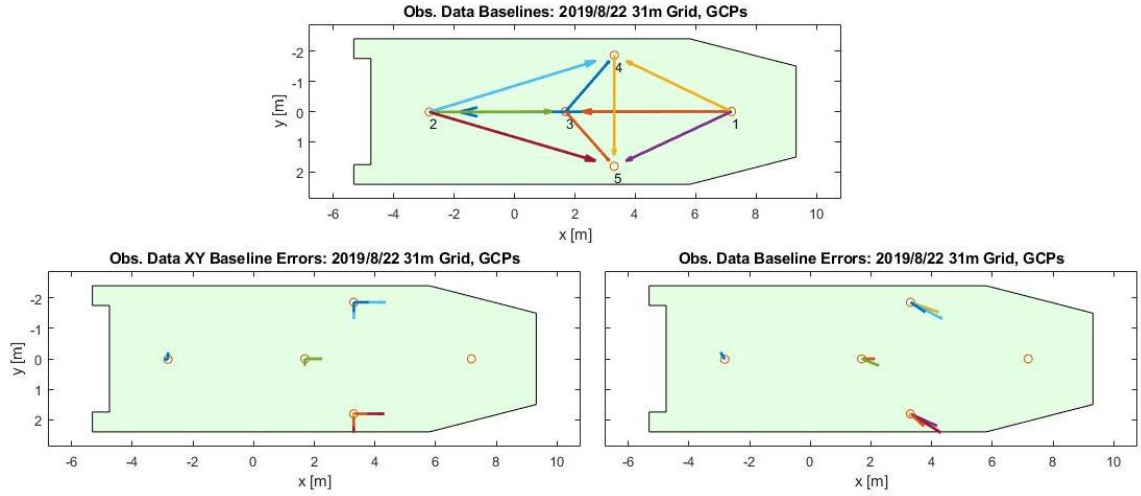
Figure 51: SRF baseline lengths (top), error vectors (left), and polar errors (right) of a 31 m grid GCP dataset flown on August 22, 2019. Errors are scaled by a factor of 30.

Figure 52: SRF baseline lengths (top), error vectors (left), and polar errors (right) of a 31 m grid dataset flown on August 21, 2019. Errors are scaled by a factor of 30.

Figure 53: SRF baseline lengths (top), error vectors (left), and polar errors (right) of a 31 m grid GCP dataset flown on August 21, 2019. Errors are scaled by a factor of 30.
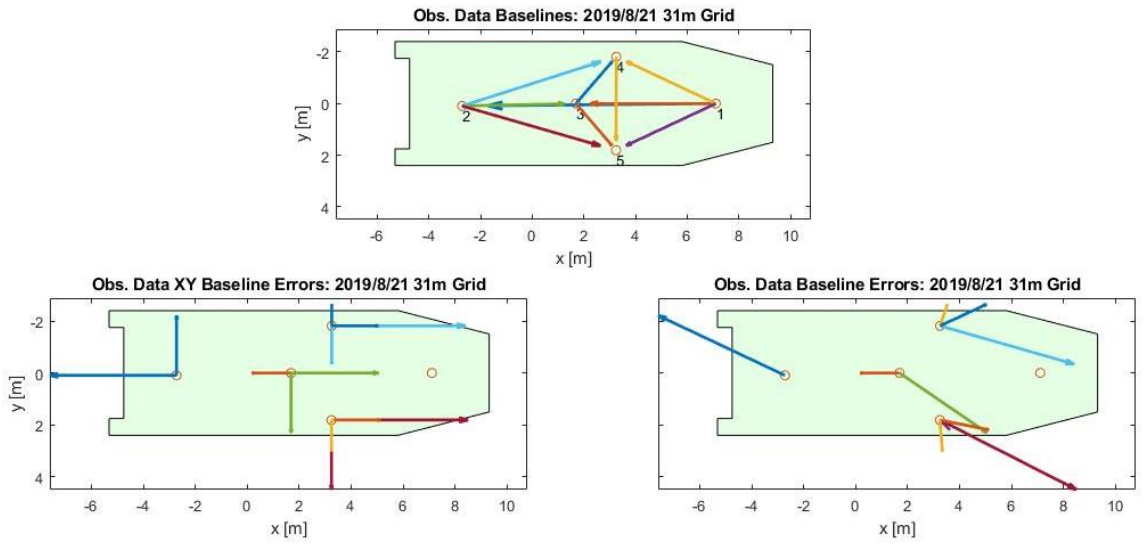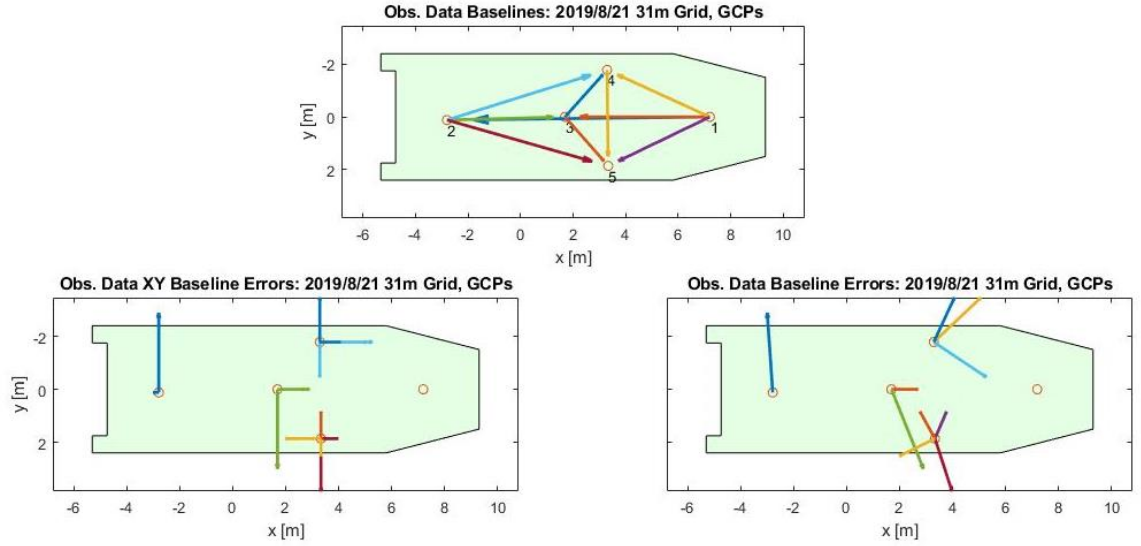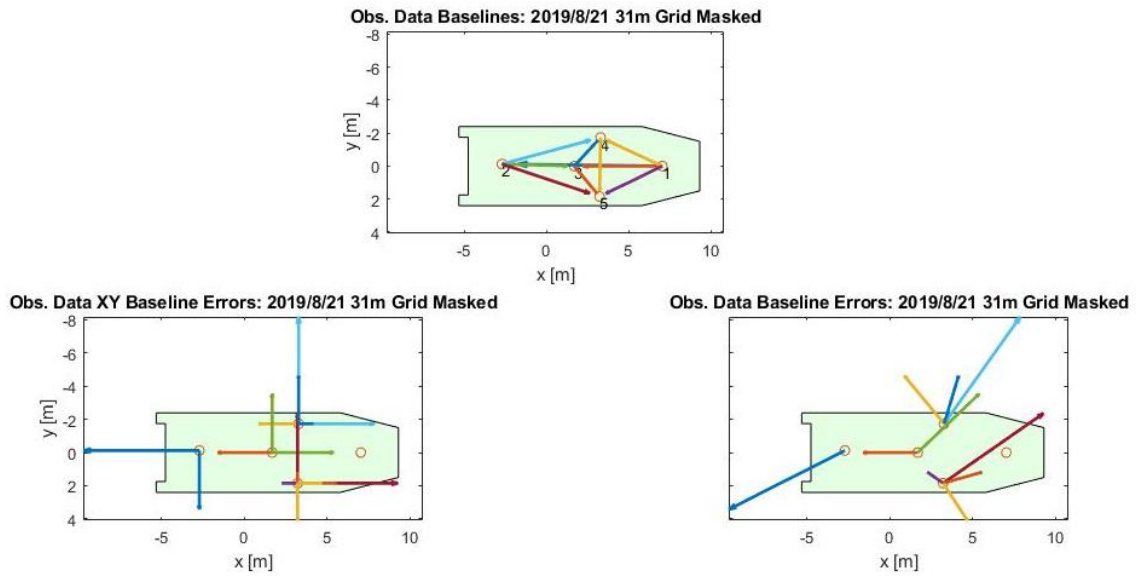

Figure 54: SRF baseline lengths (top), error vectors (left), and polar errors (right) of a 31 m grid GCP, masked dataset flown on August 21, 2019. Errors are scaled by a factor of 30.

Figure 55 demonstrates a dataset that went from almost all baselines being under scaled without GCPs to the baselines being more evenly distributed in Cartesian scaling with GCPs. This demonstrates the value of having GCPs to better scale the vessel measurements. A dataset collected with a loose vessel configuration experienced similar scaling re-distribution when including GCPs, Figure 56. Absolute scales across all UAS datasets can be seen in Appendix B.
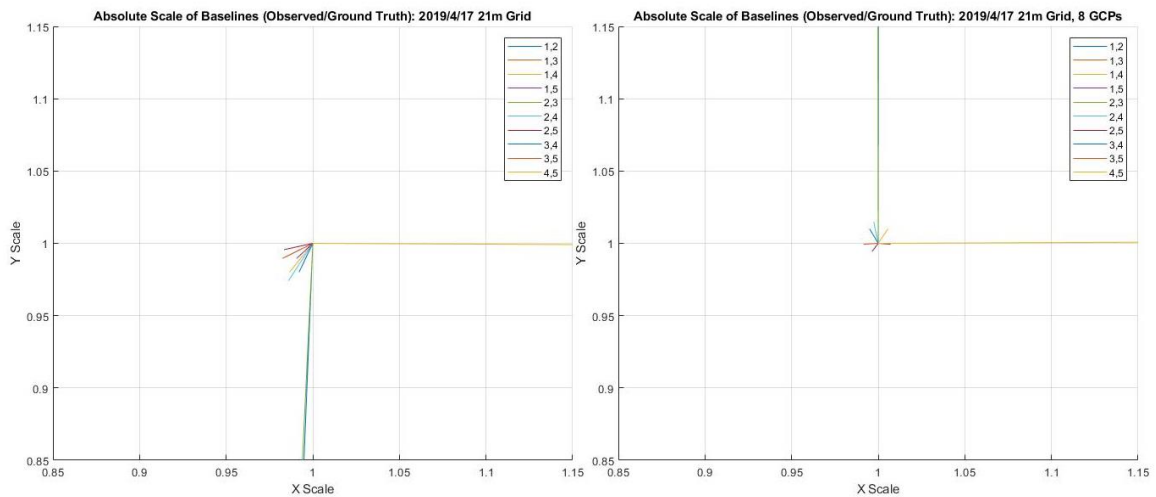

Figure 55: Absolute scales of SRF baselines observed from a 21 m grid flown on April 17, 2019 without GCPs (left) and with GCPs (right).
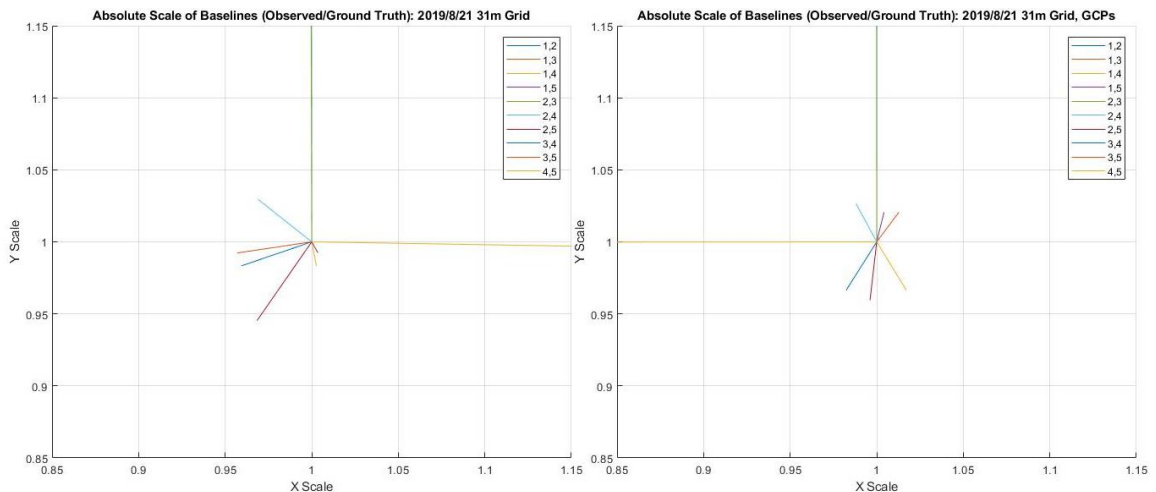
Figure 56: Absolute scales of SRF baselines observed from a 21 m grid flown on August 21, 2019 without GCPs (left) and with GCPs (right).

3.2 Horizontal Error Estimates: Seafloor Reference Method

The results from the single-beam seafloor reference method produced inconsistent results. Figures 57 and 58 demonstrate how varied the resulting lever arm approximations can be for the same line performed in opposing directions and over multiple days. Given the feature and that the line of focus is an x calibration line, it is expected that the estimated y offset be very small, while the estimated x offset be very close to its true value. However, the x estimations are in most cases rarely accurate or precise, analogous to trends seen in other x designated calibration lines, Appendix C.
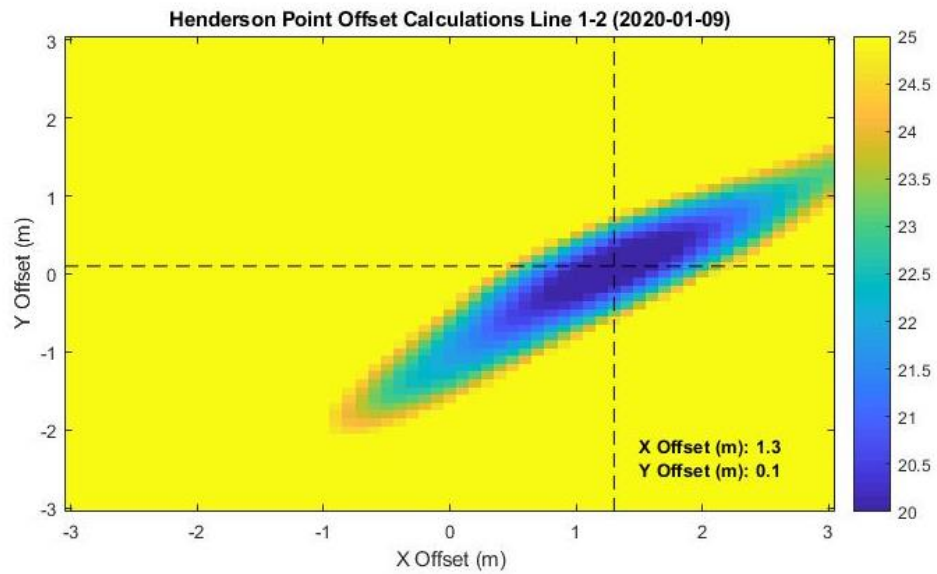
Figure 57: Estimation of x and y vessel offsets using an x calibration line at Henderson Point on January 9, 2020, with the color bar representing sum of the squares of the residuals values between ground truth and observed elevations. Lines 1-1 and 1-2 are the same line performed in opposing directions.
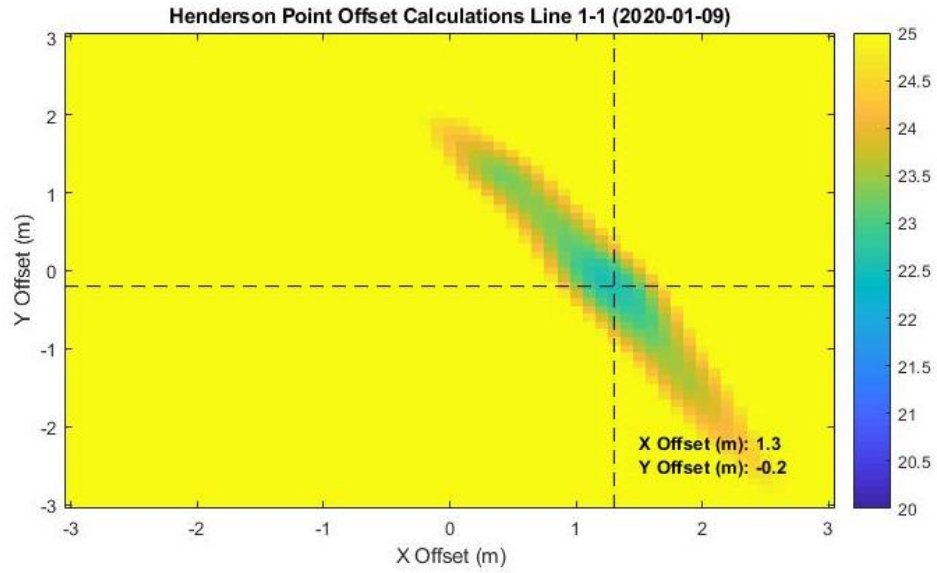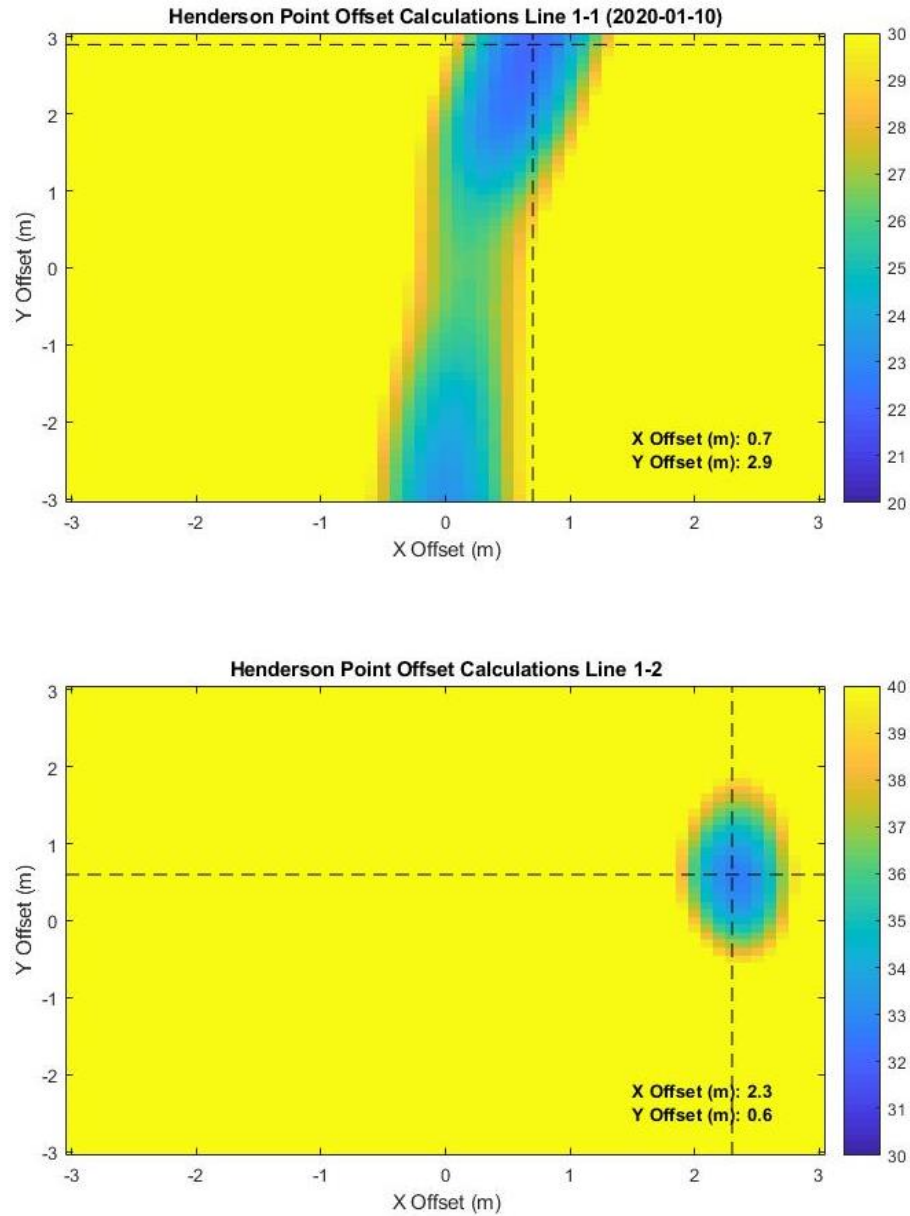
Figure 58: Estimation of x and y vessel offsets using an x calibration line at Henderson Point on January 10, 2020, with the color bar representing sum of the squares of the residuals values between ground truth and observed elevations. Lines 1-1 and 1-2 are the same line performed in opposing directions.

Similar to the performance of the x calibration lines, y calibration lines resulted in varied y offset estimations, Figures 59 and 60. The y lever arm approximations do not appear to be accurate for the same line executed in opposing directions, the same line executed over

multiple days, or between the two different features. Additionally, the y calibration lines generate predictions of the x offset that sometimes are closer to the true offset than the estimations stemming from the x calibration lines. These phenomena appear consistent across all other observed single-beam datasets, Appendix C. The implementation of this method leads to x and y offset estimations commonly between zero and 2.5 m. This is a wide range of distance, especially with the ground truth SRF Cartesian offsets in this instance being only (x,y) = (2.345, 1.294) m.

Figure 59: Estimation of x and y vessel offsets using a y calibration line at Cod Rock on January 9, 2020, with the color bar representing sum of the squares of the residuals values between ground truth and observed elevations. Lines 16-1 and 16-2 are the same line performed in opposing directions.
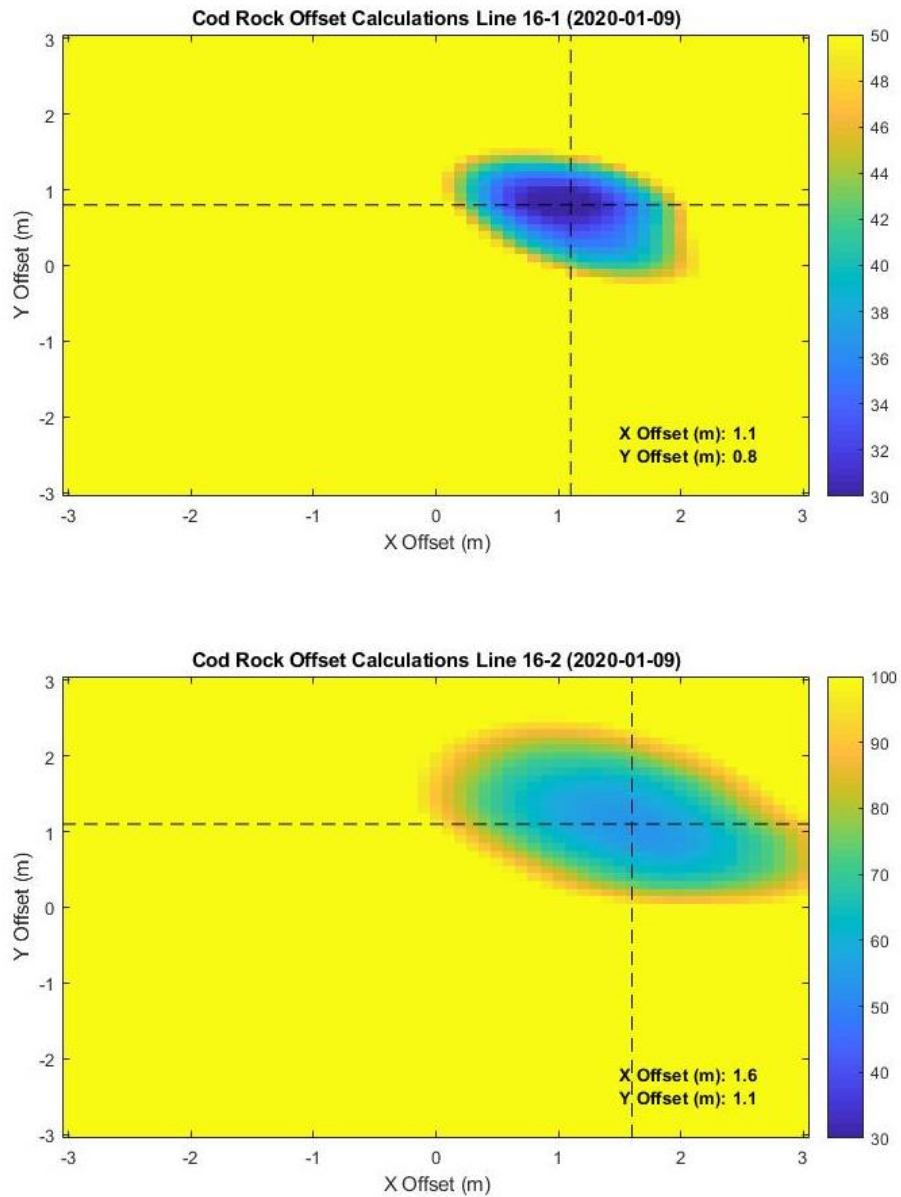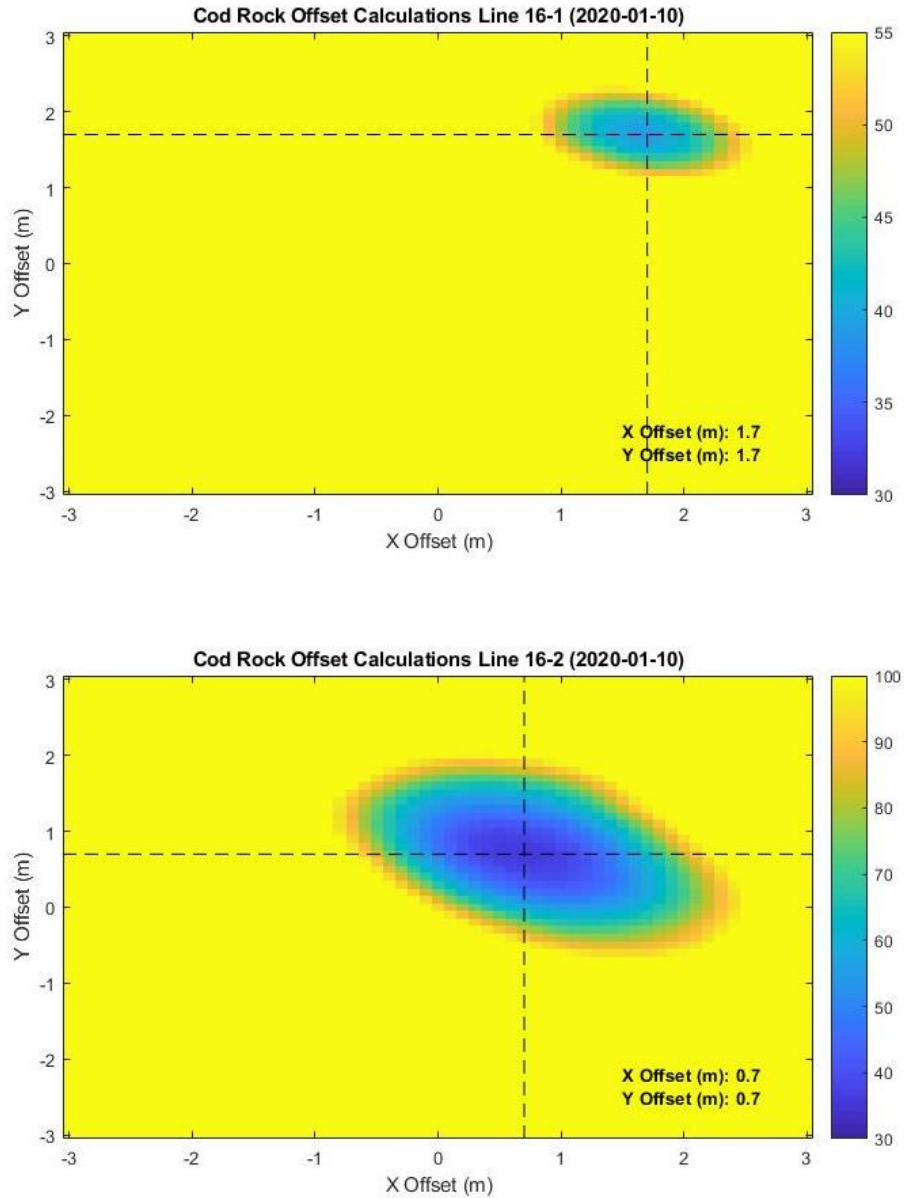
Figure 60: Estimation of x and y vessel offsets using a y calibration line at Cod Rock on January 10, 2020, with the color bar representing sum of the squares of the residuals values between ground truth and observed elevations. Lines 16-1 and 16-2 are the same line performed in opposing directions.

CHAPTER 4

DISCUSSION

4.1 Comparison of Methods

4.1.1 Comparison of Errors

The results achieved from the UAS methods have much lower uncertainty and are more consistent than those of the single-beam seafloor reference method. UAS SfM photogrammetry datasets experienced decimeter level and occasionally centimeter level deviation estimates without ground control. Implementation of ground control for the UAS SfM photogrammetry datasets lead to consistent centimeter level results, even with just three or four GCPs. UAS lidar also experienced a deviation on the centimeter level. However, the single-beam seafloor reference method was more unpredictable with x and y lever arm estimates commonly ranging from zero to 2.5 m.

4.1.2 Limitations and Benefits

The UAS methods discussed here present a choice between SfM photogrammetry and lidar, with some overlapping and separate factors to consider. Table 9 highlights the tradeoffs between using UAS SfM photogrammetry and lidar for vessel calibrations. It can be seen that the lowest cost UAS survey is SfM photogrammetry without ground control. Both time and cost will inherently increase when a UAS SfM survey is performed with GCPs. However, even with taking the time to survey in GCPs, the UAS SfM photogrammetry method could still cost less than a UAS lidar survey. Additionally, if GCPs are desired it

would be best to secure them to a pier or stable feature(s) near an open area where the vessel can safely be tied down and mapped by a UAS. It is important to note that the time it takes to execute this type of survey will depend on the size and shape of the vessel.

Table 9: An illustration showing the tradeoffs between the two investigated UAS methods for horizontally calibrating vessels.

UAS Tradeoffs: Vessel Calibration Surveys	
UAS SfM Photogrammetry	**UAS Lidar**
Low cost UAS and camera sensors can be utilized	Expensive UAS and lidar units required
Decimeter/centimeter level accuracies without GCPs (Lowest cost survey)	High quality aircraft positioning required (RTK or PPK GNSS)
Centimeter level accuracies with GCPs (Second lowest cost survey)	Centimeter level accuracies (Highest cost survey)
Quick survey time. Multiple flights may be required	Quick survey time. A single flight is most likely sufficient
Survey quality affected by water level and vessel attitude change	Survey quality affected by water level and vessel attitude change
Requires extra lines to tie down the vessel, optimizing survey qualities	Requires extra lines to tie down the vessel, optimizing survey qualities
Best performed during high or low tide	Best performed during high or low tide
Simple to operate	Complex to operate

Cost effectiveness will be a significant factor in CSB providers deciding which UAS method to use for this application. Consumer grade photogrammetry UASs cost much less than industrial grade UASs implemented for aerial lidar. UAS lidar also requires an expensive lidar system to be mounted onto the UAS, a calibration of the offsets between the UAS sensors, and can be complex to operate. This thesis demonstrates that UAS SfM photogrammetry with GCPs can obtain similar and at times slightly better accuracies than UAS lidar, meaning UAS SfM photogrammetry can be used to produce a comparable quality survey as UAS lidar at a much lower cost. However, if operators of vessels want to calibrate horizontal lever arms without paying to have their vessel surveyed, the manual single-beam seafloor reference method could be employed and the data sent to a trusted node for processing.

The seafloor reference method provides an advantageous alternative technique to the proposed UAS methods as it does not require any additional equipment outside of typical ocean mapping operations and it directly calibrates the horizontal lever arms. However, basic requirements must be met before the calibration can proceed. There must be a local bathymetric feature that holds a significant amount of elevation change. In addition, the feature must have previously been mapped with a MBES and must be extremely stable in appearance, ensuring that the results are repeatable. Unfortunately, this could potentially limit the implementation of this method as some vessels may not have the luxury of transiting near a feature such as this. Even with the existence of such a feature, CSB vessels must go over the feature in ways that enable proper data comparisons to the reference surface for offset estimations.

An additional limitation to the single-beam seafloor reference method is the quality of offset estimations obtained from the described lever arm estimation process. Offset estimations from this technique ranged from zero to 2.5 m, making the method unreliable for vessels with short lever arms, thus limiting the practical implementation of this particular methodology. Since the methodology tested in this thesis relies strongly on the relationship of the elevation patterns between the single-beam profiles and the reference surface, the accuracy of the offset estimation is limited by both the quality/resolution of the reference data and the minimum sum of the squares of the residuals algorithm. The algorithm's ability to estimate how strongly the observed and reference elevation patterns match each other does not reach the desired level of accuracy or consistency for CSB offsets when using the reference data described in this thesis. Recent work by Rondeau and

Dion (2020) demonstrate that a workflow, similar to the one laid out in this thesis, was utilized to calibrate an x lever arm length of 184 m with a 1 m accuracy. This finding and the research in this thesis suggest that this type of calibration may possess a limited accuracy for horizontal offset estimation, which in some instances may not meet the desired accuracy for CSB surveys.

4.2 Implementation of Methods

4.2.1 Operational Recommendations

Before workflows of the outlined methods are implemented in the field for practical use, there are important recommendations to consider. When performing horizontal vessel calibrations with UASs it is best to perform the survey(s) at high or low tide, with the vessel tied down as tightly as possible, and during calm environmental conditions. For consistent centimeter level accuracies, establishment of a ground control network near the vessel must be done. This thesis demonstrates that it is not essential to have the vessel reside within the control network to obtain centimeter level accuracies. Thus, simply having the control network as close to the vessel as possible will suffice. If large vessel movement is expected, it is recommended to utilize GCPs to limit the errors introduced from the motion. However, this protocol will not eliminate all induced errors and the errors will become more random with higher degrees of motion. If the vessel does not have an established SRF, the workflow outlined in this paper should be utilized to establish the SRF, and refer coordinates to it. A point in the middle of the vessel that can be seen from the aircraft should be chosen as the arbitrary horizontal origin of the vessel if one does not already exist. Additional defined features on the vessel that can be seen from the UAS, such as sharp edges, should be

assigned coordinates to preserve the SRF. If the echo sounder is not visible from the aircraft, a point in which manual measurements to the echo sounder can be made could be established. If obtaining significant vertical information of the vessel is desired, it is recommended to carry out oblique camera oriented orbits as supplementary data to the 3D grid nadir camera orientation flights.

4.2.2 Future Work

Discoveries have been made on how the methods developed could be practically implemented, but there are opportunities for continuing work with these methods. For this project, investigation into alternative horizontal calibration methods for vessels was the focus for the three proposed methods. However, each method produces 3D geospatial data that could be utilized to calibrate vertical sensor offsets on vessels. Both UAS SfM photogrammetry and lidar data collected in the discussed experiments could be utilized to explore this idea. Contrary to the UAS horizontal calibration, the vertical calibration would most likely be performed by selecting points that define a desired measurement in the point cloud or mesh model instead of the orthomosaic, as the orthomosaic is best defined in the horizontal plane as opposed to the vertical. By comparing vertical measurements on the observed models to ground truth measurements, accuracies for the UAS vertical calibrations could be estimated. Existing vessel motion analysis from these experiments could be implemented to assess the impacts of vessel motion on the quality of UAS vertical calibrations. Additionally, the single-beam seafloor reference workflow described in this paper could be utilized to investigate the practicality of performing a vertical offset

calibration. These described methods may offer alternatives or checks to traditional vessel surveys and the vertical offset calibration implemented in Calder et al. (2020).

In addition to exploring vertical calibrations with the proposed methods, work could be attempted to further understand the capabilities of the UAS methods. This work explores surveying vessels while they are docked in water with UASs and assesses the resulting errors. Even though an SRF transformation is demonstrated, the workflow was not implemented to define the exact location of an echo sounder on board a vessel. Directly surveying in a location such as this with a UAS may prove to be difficult since most echo sounders are secured to the hull of the vessel and would not be visible from the aircraft. Consequently, a procedure must be created to obtain an echo sounder location within an SRF when implementing UASs to survey vessels. It would also be advantageous to continue investigation on how to limit errors of the UAS survey(s) induced by vessel motion.

An attempt was made in this research to compensate for the vessel's motion by applying the vessel's attitude changes to the UAS orientations. A code that took the changes in orientation from the vessel's position at the start of a defined flight, and subtracted them from the UAS's orientations at the time of picture capture, was created. This process incorporated exporting the Exchangeable Image File Format (EXIF) information as a text file from the relevant images, which included the aircraft's recorded roll, pitch, and heading at the time each image was captured. After the code calculated the new UAS orientations based on the changes in the vessel orientations, it updated the EXIF file for the associated

UAS images with the new UAS orientations. The new EXIF file and associated images were then imported into Agisoft Metashape where the previously described workflow was implemented to process the data. A couple of datasets were processed with this method but generated inconsistent results with respect to final survey accuracies. More rigorous means of factoring in the vessel motion may be required to determine whether factoring in the vessel's change in orientation to the UAS's recorded orientations is a viable means of limiting errors induced by the vessel's motion during aerial survey operations.

It would be valuable to further explore quality control techniques for the proposed UAS methods. For the purposes of this project a ground truth survey existed, enabling error estimation of the observed models. When implementing the proposed UAS methods in the field, a previous ground truth vessel survey will most likely not exist. Thus, exploration into checking the quality of an observed UAS vessel survey in the absence of ground truth data would be advantageous. In this thesis, temporary/secondary targets were established on the vessel and distances between targets were measured with tape, resulting in rough approximation checks. As a more accurate alternative, this may be done by statically observing multiple points on the vessel while it is in water over a defined length of time with a total station set up on a stationary known point in an external coordinate system. The coordinate observations could then be directly compared to the observed UAS based vessel coordinates in an external coordinate system. This exploration could prove to be useful in quantifying errors of observed UAS vessel models. Similarly, accuracy assessment of UAS vessel surveys performed with a vessel residing within a control network should be investigated. This work demonstrates that centimeter level accuracies

are obtainable with UAS sensors when establishing a control network adjacent to the vessel. However, investigating the effects that ensue when a vessel is docked within a control network could be valuable in knowing whether the location of the control network significantly impacts the UAS surveys.

Given the inconsistent results of the single-beam seafloor reference method, it can be concluded that the offset estimation methodology does not meet the standard of vessel offset accuracies with the combination of methodology and reference data used in this thesis. Based on the results from this thesis, it is suggested that another comparison algorithm be tested against higher resolution reference data. This exploration may uncover more information on the capabilities of utilizing known multibeam data and observed single-beam data to calibrate horizontal lever arms.

CHAPTER 5

CONCLUSION

Through the implementation of all three proposed methods for performing horizontal vessel calibrations, discoveries on the limitations and benefits of each method have been made. These pathfinder experiments investigated how to deal with the different challenges associated with each technique by attempting different collection and processing procedures. This experimentation led to the creation of fine-tuned SOPs for each explored method. In the future, if users want to employ the discussed methods for horizontally calibrating vessels, they can follow the data collection and processing guidelines set forth by this thesis.

This thesis also demonstrated that the established SOPs for the UAS methods led to as low as centimeter level deviation estimates, while the single-beam seafloor reference SOP resulted in much higher, meter level errors. Although there is no set standard for CSB offset accuracies, the achieved UAS horizontal deviation estimates exceed accuracy expectations of horizontal offsets for CSB applications, unlike the seafloor reference method. In addition to CSB use, the UAS methods have potential to be implemented for high quality ocean mapping operations, given that their centimeter level accuracy potential could meet offset accuracy requirements for these vessels. The procedures and results from this thesis demonstrate that there are practical alternatives to traditional land surveying methods for accurately calibrating horizontal vessel offsets.

List of References

American Society for Photogrammetric Engineering and Remote Sensing (ASPRS). (2015). ASPRS positional accuracy standards for digital geospatial data (Edition 1, Version 1.0., November, 2014). Photogrammetric Engineering & Remote Sensing, 81(3), A1-A26.

Agisoft LLC. (2019). Agisoft Metashape User Manual Professional Edition, Version 1.5. Available at: https://www.agisoft.com/pdf/metashape-pro_1_5_en.pdf

Applanix Corp. (2013). POSMV 320 Specifications. Available at: https://seatronics-group.com/files/6314/1753/4903/Applanix_POS_MV_-_Datasheet.pdf

ARE. (July 2019). UNH Gulf Surveyor Lidar Scan. For access contact info@ccom.unh.edu.

Calder, B. R., Dijkstra, S. J., Hoy, S., Himschoot, K., & Schofield, A. (2020). A Design for a Trusted Community Bathymetry System. *Marine Geodesy*, 1-32.

Center for Coastal and Ocean Mapping Joint Hydrographic Center (CCOM/JHC). R/V Gulf Surveyor. Retrieved on January 20, 2020. Retrieved from: http://ccom.unh.edu/facilities/research-vessels/rv-gulf-surveyor

DJI. Matrice 600 Pro. Retrieved on January 20, 2020. Retrieved from: https://www.dji.com/matrice600-pro

DJI. Phantom 4 Pro. Retrieved on January 20, 2020. Retrieved from: https://www.dji.com/phantom-4-pro/info

DJI. Phantom 4 Pro V2.0. Retrieved on January 20, 2020. Retrieved from: https://store.dji.com/product/phantom-4-pro-v2?site=brandsite&from=buy_now_bar&vid=43151

Dodge, M. & Kitchin, R. (2013). Crowdsourced cartography: mapping experience and knowledge. *Environment and Planning A*, *45*(1), 19-36.

Doucet Survey Inc. (May 2016), Surveying and Laser Scanning Service For the "Gulf Surveyor" Research Vessel. For access contact info@ccom.unh.edu.

Doucet Survey Inc. (June 2016), Updated Reference Coordinates For the "Gulf Surveyor" Research Vessel. For access contact info@ccom.unh.edu.

Herlihy, D., Hillard, B., & Rulon, T. (1989). National oceanic and atmospheric administration seabeam system patch test. *International Hydrographic Review*, *66*(2), 119-139.

Hillman, J. I. (2019). Mapping the Oceans. *Frontiers for Young Minds*, *7*(Article 25).

Hughes Clarke, J. (2003, March). A reassessment of vessel coordinate systems: what is it that we are really aligning. In *US Hydrographic Conference*.

IHO. Crowdsourced Bathymetry. Retrieved on January 20, 2020. Retrieved from: https://iho.int/en/crowdsourced-bathymetry

James, M. R. & Robson, S. (2014). Mitigating systematic error in topographic models derived from UAV and ground-based image networks. *Earth Surface Processes and Landforms*, *39*(10), 1413-1420.

Luma-ang, C. (2017). Crowdsourced Bathymetry: Supporting Progress or Threatening Security.

Mayer, L., Jakobsson, M., Allen, G., Dorschel, B., Falconer, R., Ferrini, V., Lamarche, G., Snaith, H., & Weatherall, P. (2018). The Nippon Foundation—GEBCO seabed 2030 project: The quest to see the world's oceans completely mapped by 2030. *Geosciences*, 8(2), 63.

NGS. National Geodetic Survey Data Explorer. Retrieved on January 20, 2020. Retrieved from: https://www.ngs.noaa.gov/NGSDataExplorer/

NGS. Geodetic Toolkit: HTDP. Retrieved on March 5, 2020. Retrieved from: https://www.ngs.noaa.gov/TOOLS/Htdp/Htdp.shtml

NOAA NCEI. Report for H11014. Retrieved on March 12, 2020. Retrieved from: https://www.ngdc.noaa.gov/nos/H10001-H12000/H11014.html

NOAA. Tides/Water Levels. Retrieved on January 20, 2020. Retrieved from: https://tidesandcurrents.noaa.gov/waterlevels.html?id=8423898&units=metric&bdate=20190417&edate=20190418&timezone=LST/LDT&datum=MLLW&interval=6&action=

Nebiker, S., Annen, A., Scherrer, M., & Oesch, D. (2008). A light-weight multispectral sensor for micro UAV—Opportunities for very high resolution airborne remote sensing. *The international archives of the photogrammetry, remote sensing and spatial information sciences*, *37*(B1), 1193-1199.

Paul S. (2018). Hyperparameter Optimization in Machine Learning Models. Retrieved on March 12, 2020. Retrieved from: https://www.datacamp.com/community/tutorials/parameter-optimization-machine-learning-models

Robertson, E. (2016). Crowd-Sourced Bathymetry Data via Electronic Charting Systems. *In ESRI Ocean GIS Forum*. Available at: https://proceedings.esri.com/library/userconf/oceans16/papers/oceans_12.pdf

Rondeau, M. & Dion, Pierre. (2020). Potential of a HydroBox Crowd-Sourced Bathymetric Data Logger to Support the Monitoring of the Saint-Lawrence Waterway. *Canadian Hydrographic Conference.*

Sanz-Ablanedo, E., Chandler, J., Rodríguez-Pérez, J., & Ordóñez, C. (2018). Accuracy of unmanned aerial vehicle (UAV) and SfM photogrammetry survey as a function of the number and location of ground control points used. *Remote Sensing*, *10*(10), 1606.

SeaBeam Instruments. (2000). Multibeam Sonar Theory of Operation.

Simpson, C. H. (2018). A Multivariate Comparison of Drone-Based Structure from Motion and Drone-Based Lidar for Dense Topographic Mapping Applications.

Weatherall, P., Marks, K. M., Jakobsson, M., Schmitt, T., Tani, S., Arndt, J. E., Rovere, M., Chayes, D., Ferrini, V., & Wigley, R. (2015). A new digital bathymetric model of the world's oceans. *Earth and Space Science*, *2*(8), 331-345.

Appendix A
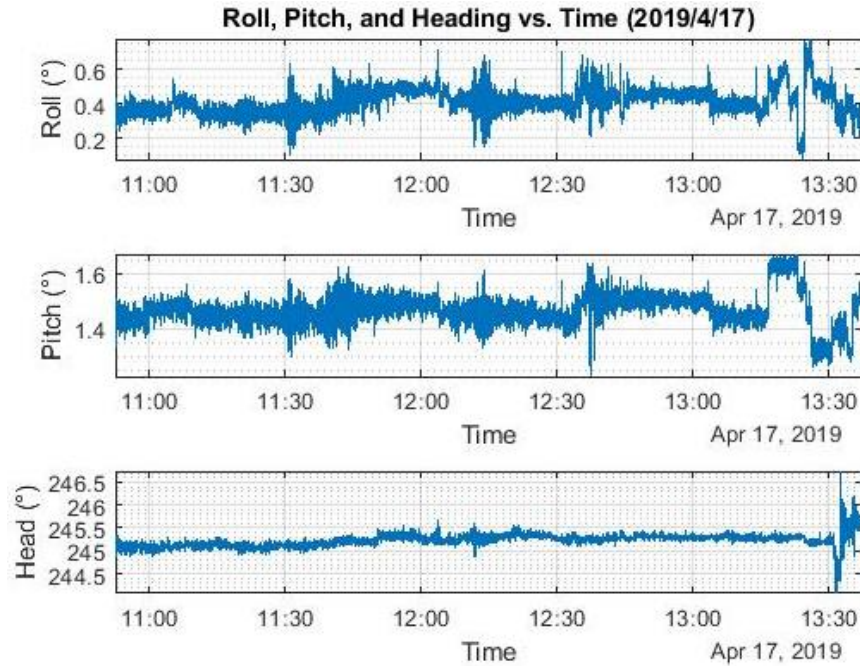
Figure A.1: Roll, pitch, and heading time series of the *R/V Gulf Surveyor* tightly tied down on April 17, 2019, with time in EST.
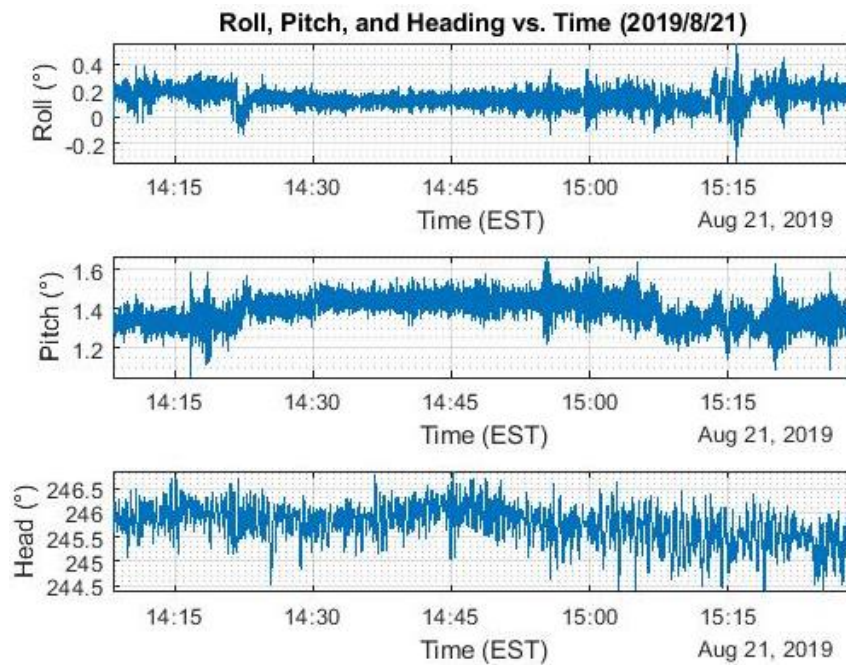
Figure A.2: Roll, pitch, and heading time series of the *R/V Gulf Surveyor* loosely tied down on August 21, 2019.
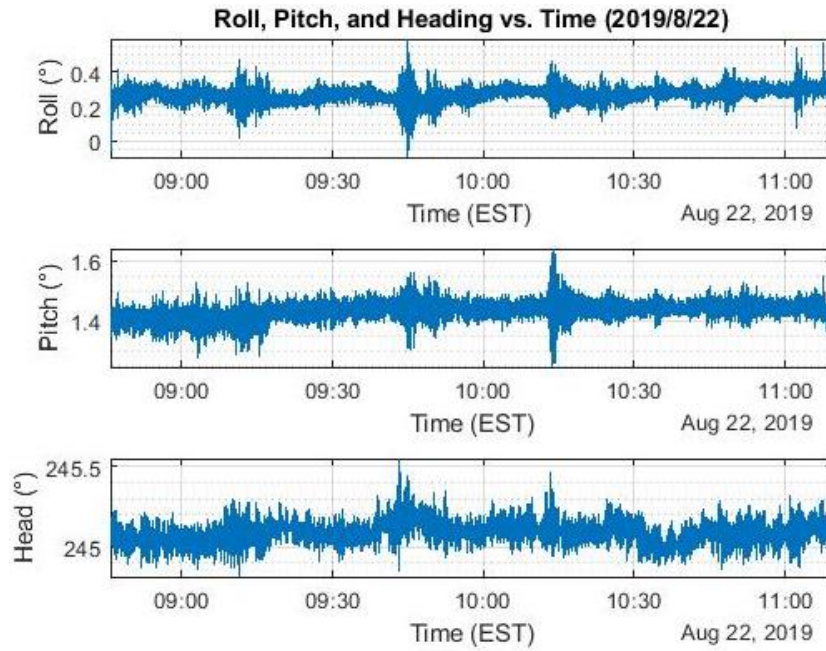
Figure A.3: Roll, pitch, and heading time series of the *R/V Gulf Surveyor* tightly tied down on August 22, 2019.
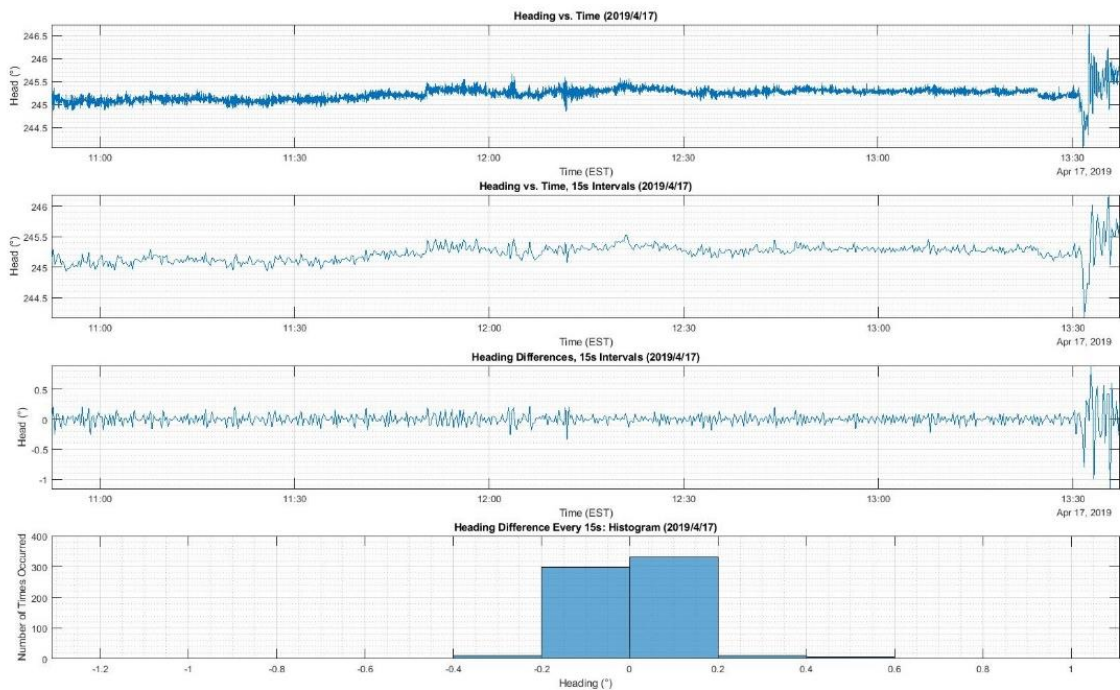
Figure A.4: Heading plots of the *R/V Gulf Surveyor* tightly tied down on April 17, 2019.
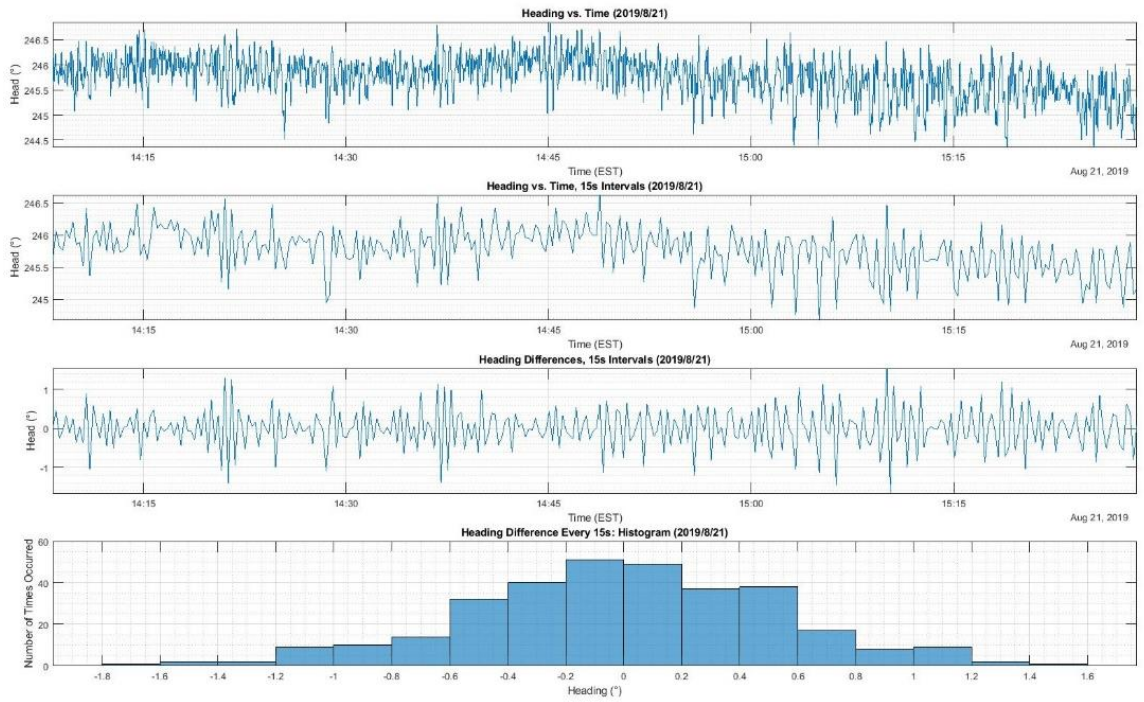
Figure A.5: Heading plots of the *R/V Gulf Surveyor* loosely tied down on August 21, 2019.
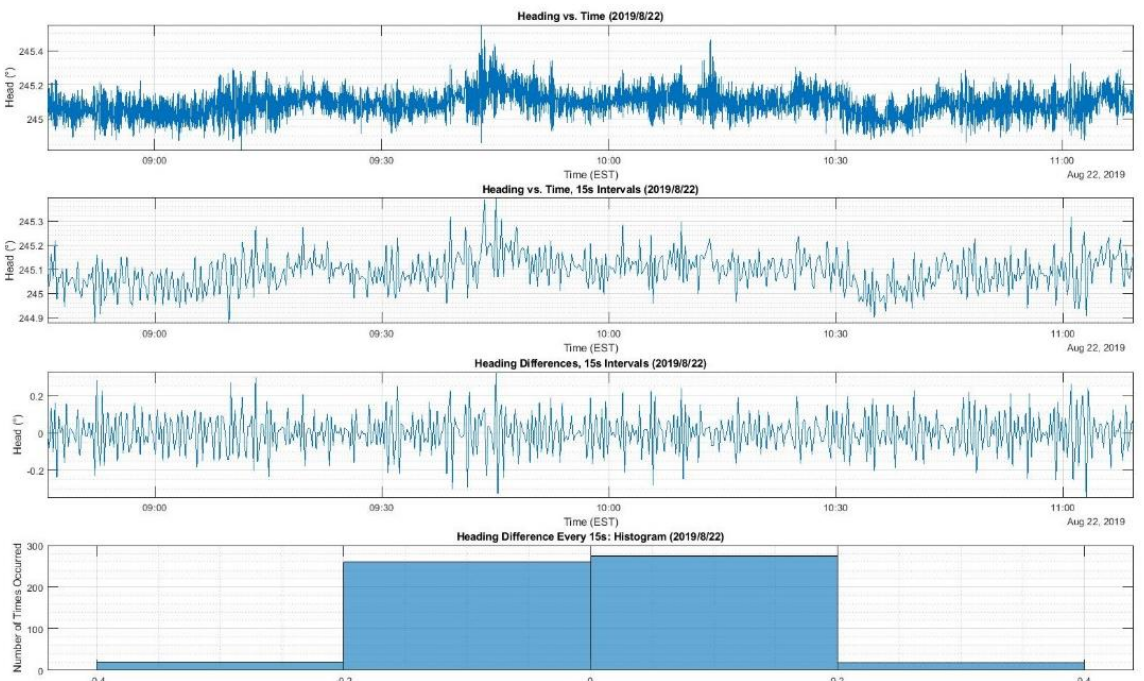
Figure A.6: Heading plots of the *R/V Gulf Surveyor* tightly tied down on August 22, 2019.
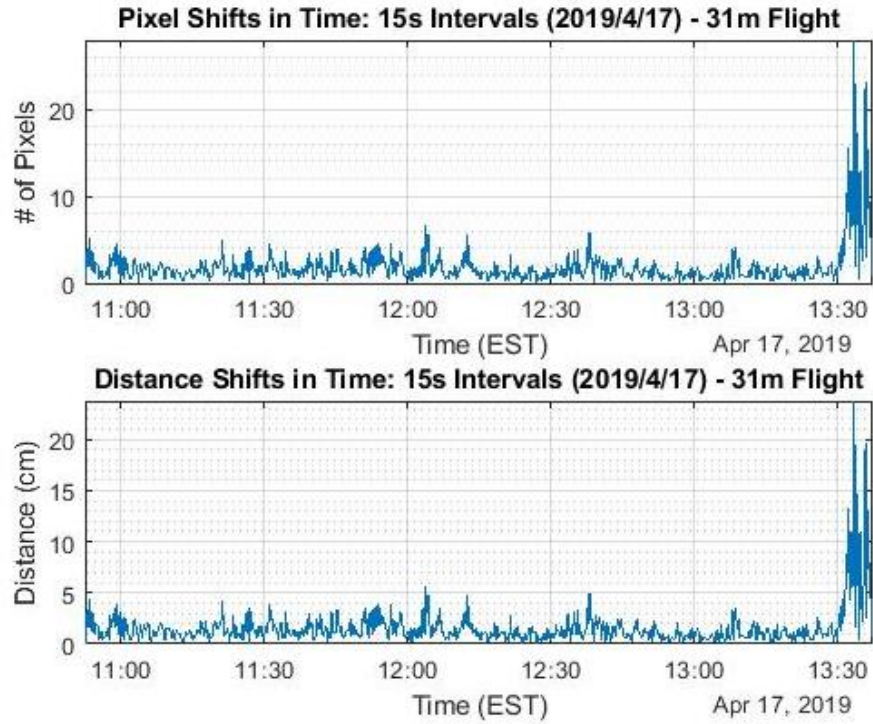
Figure A.7: Pixel and distance shifts the tightly tied down *R/V Gulf Surveyor* experienced during the April 17, 2019 UAS surveys.
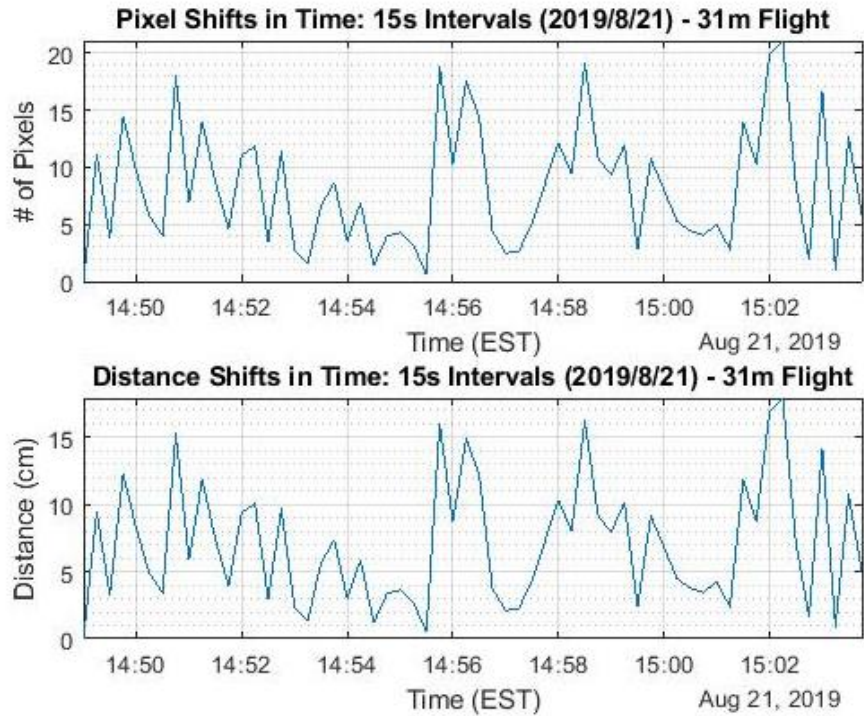
Figure A.8: Pixel and distance shifts the loosely tied down *R/V Gulf Surveyor* experienced during the August 21, 2019 UAS surveys.
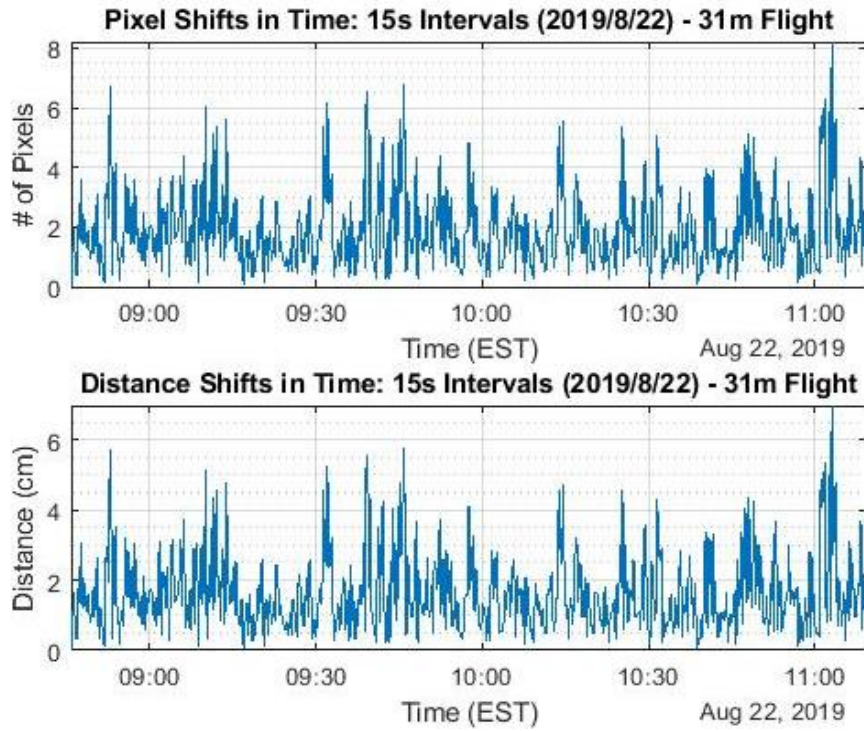
Figure A.9: Pixel and distance shifts the tightly tied down *R/V Gulf Surveyor* experienced during the August 22, 2019 UAS surveys.

Appendix B
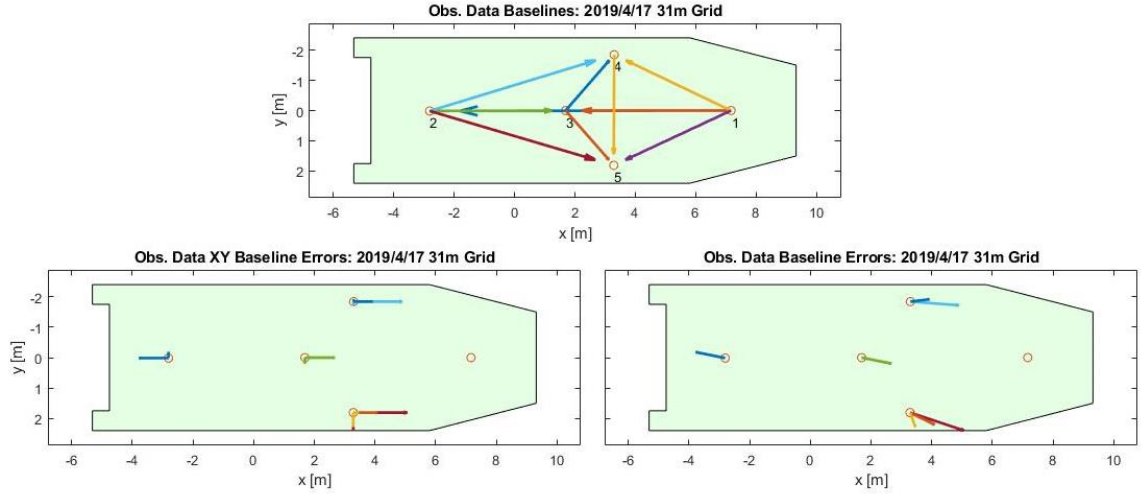
Figure B.1: SRF baseline lengths (top), error vectors (left), and polar errors (right) of a 31 m grid dataset flown on April 17, 2019. Errors are scaled by a factor of 30.
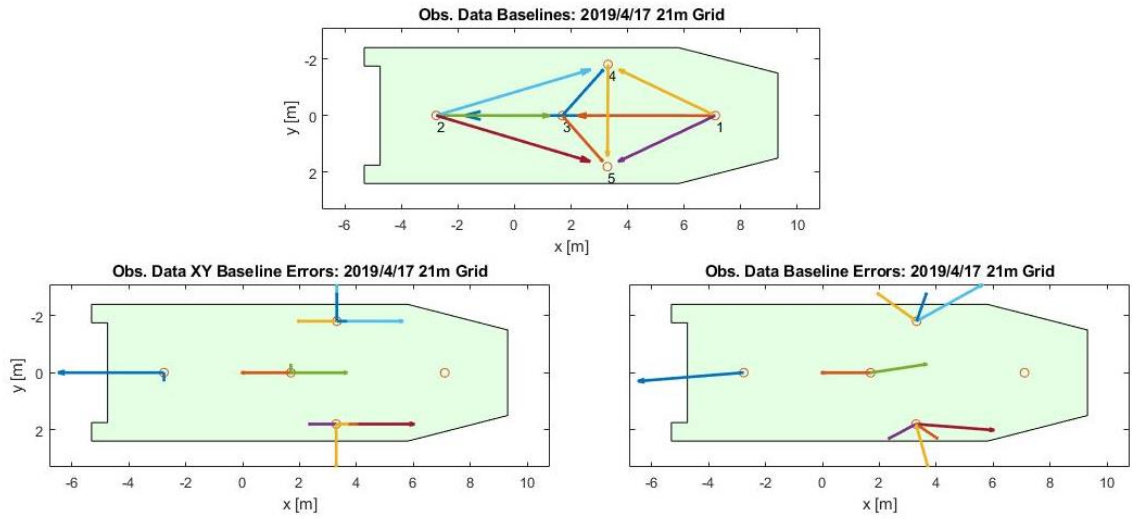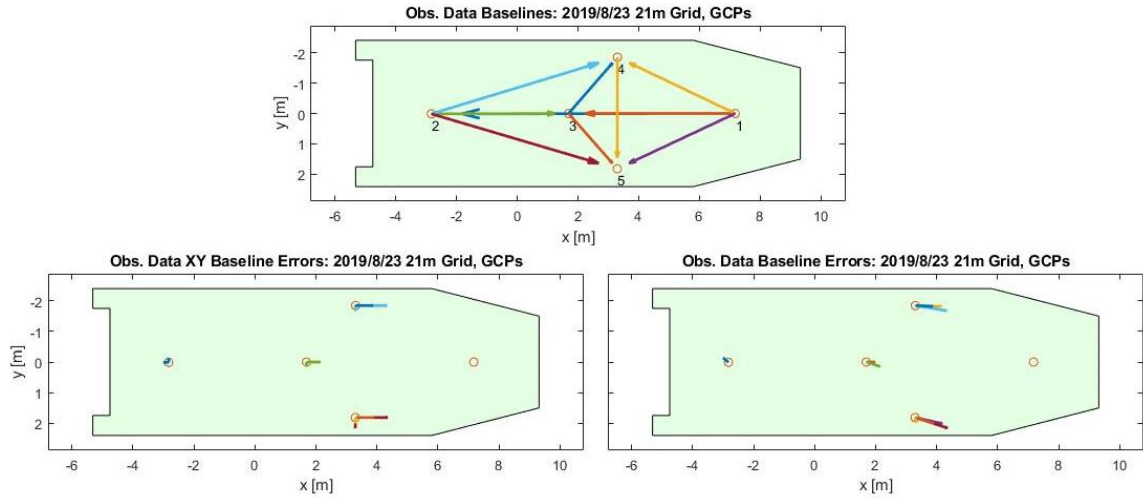

Figure B.2: SRF baseline lengths (top), error vectors (left), and polar errors (right) of a 21 m grid dataset flown on April 17, 2019. Errors are scaled by a factor of 30.
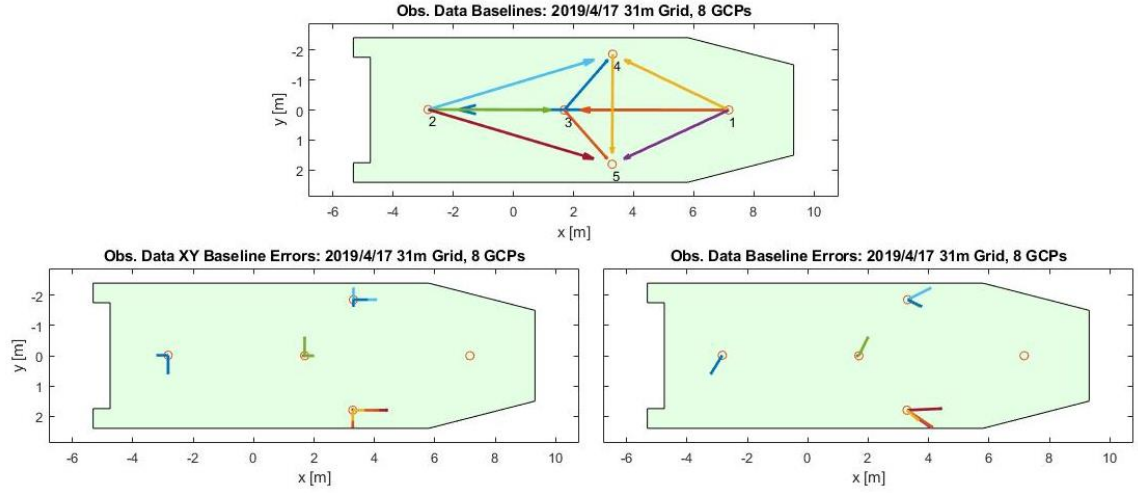
Figure B.3: SRF baseline lengths (top), error vectors (left), and polar errors (right) of a 31 m grid dataset with GCPs flown on April 17, 2019. Errors are scaled by a factor of 30.
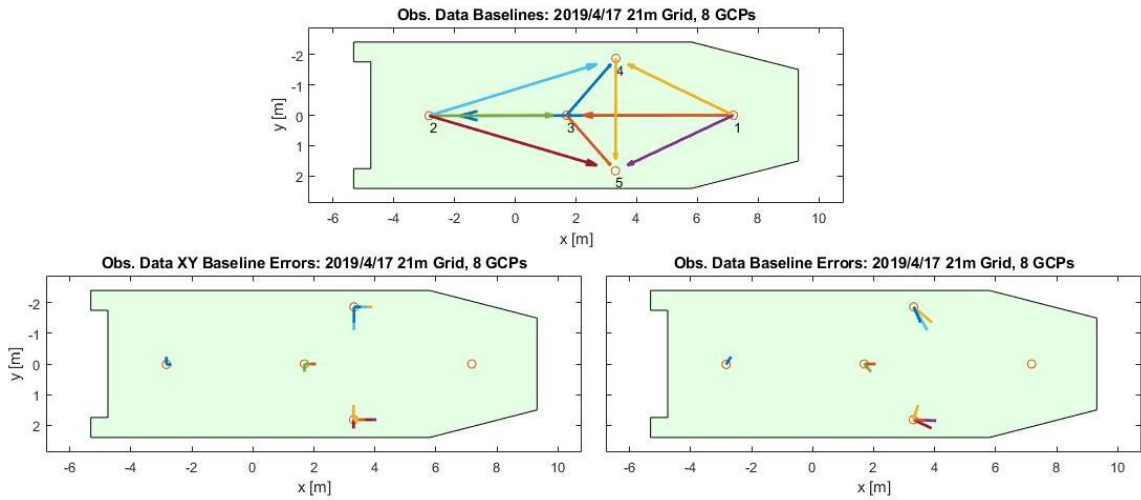
Figure B.4: SRF baseline lengths (top), error vectors (left), and polar errors (right) of a 21 m grid dataset with GCPs flown on April 17, 2019. Errors are scaled by a factor of 30.
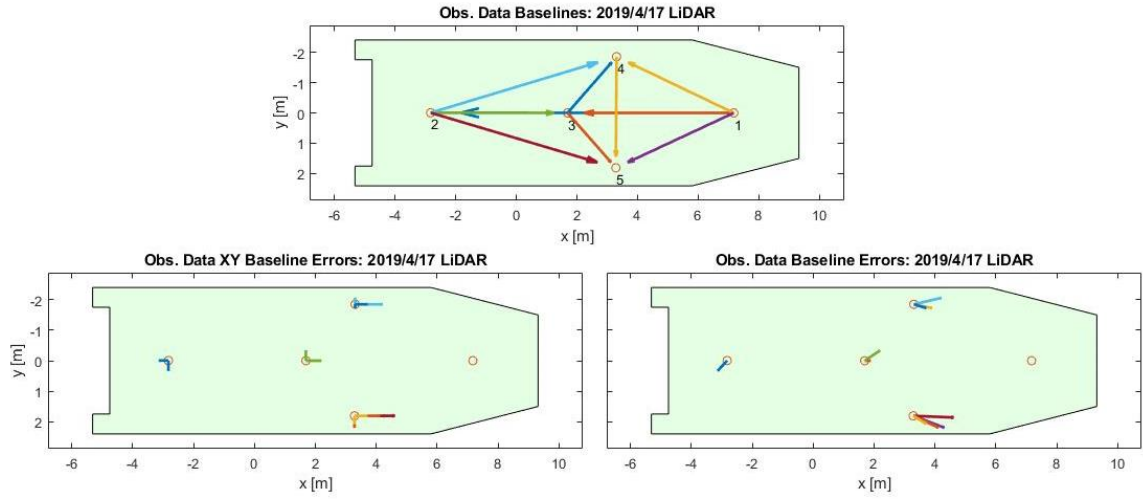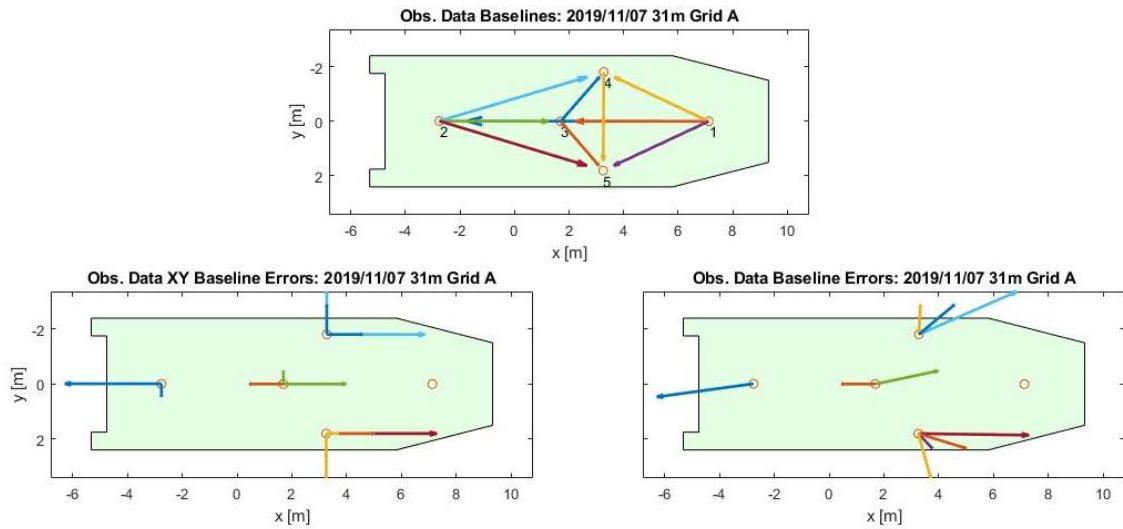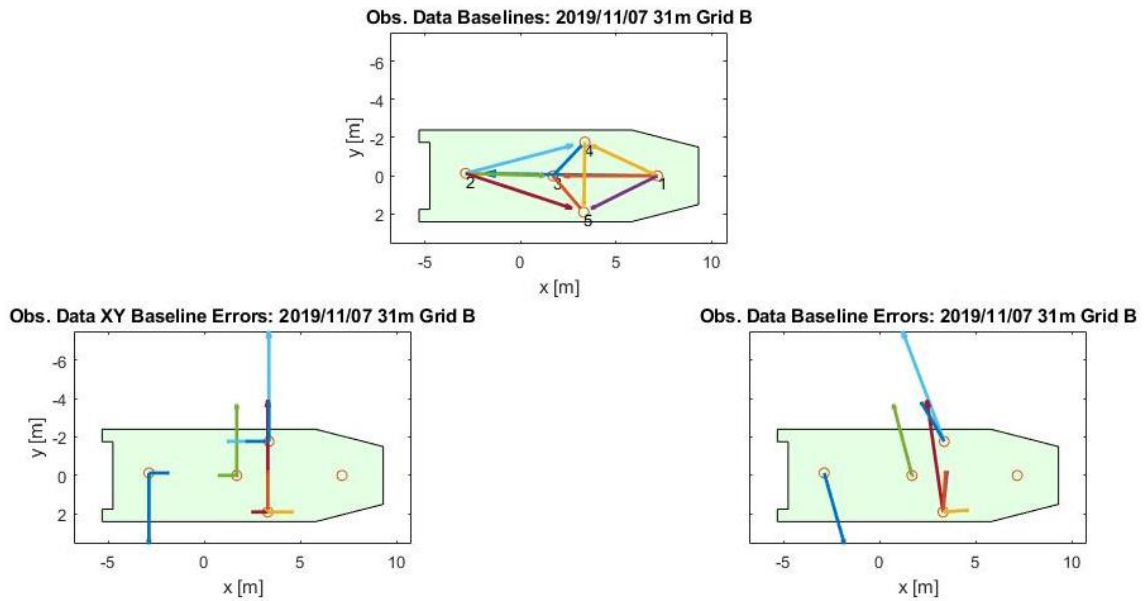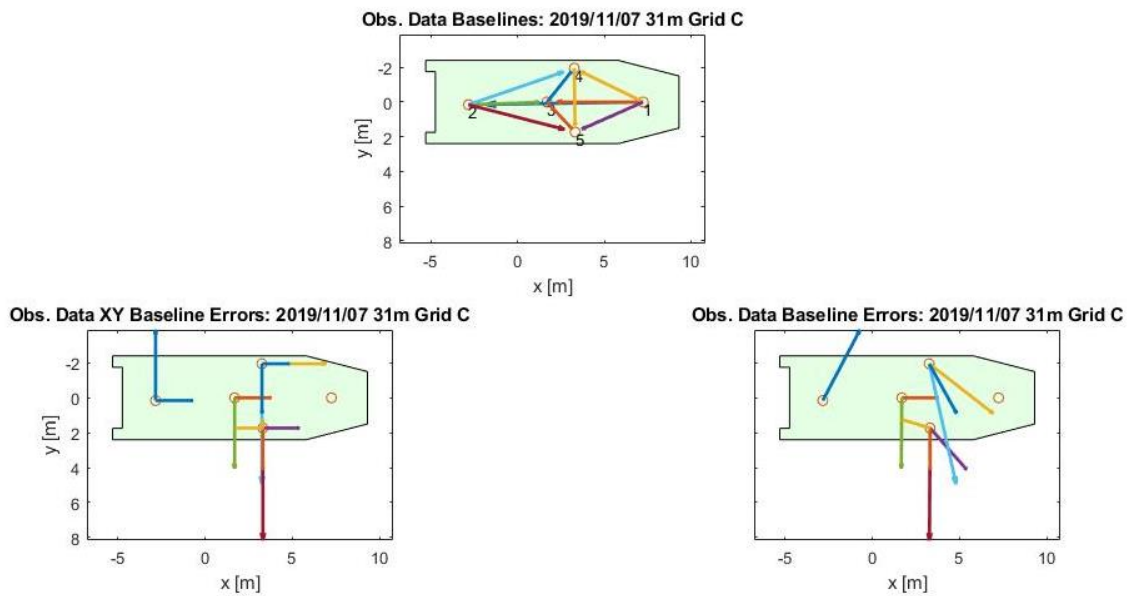
Figure B.5: SRF baseline lengths (top), error vectors (left), and polar errors (right) of lidar data flown on April 17, 2019. Errors are scaled by a factor of 30.
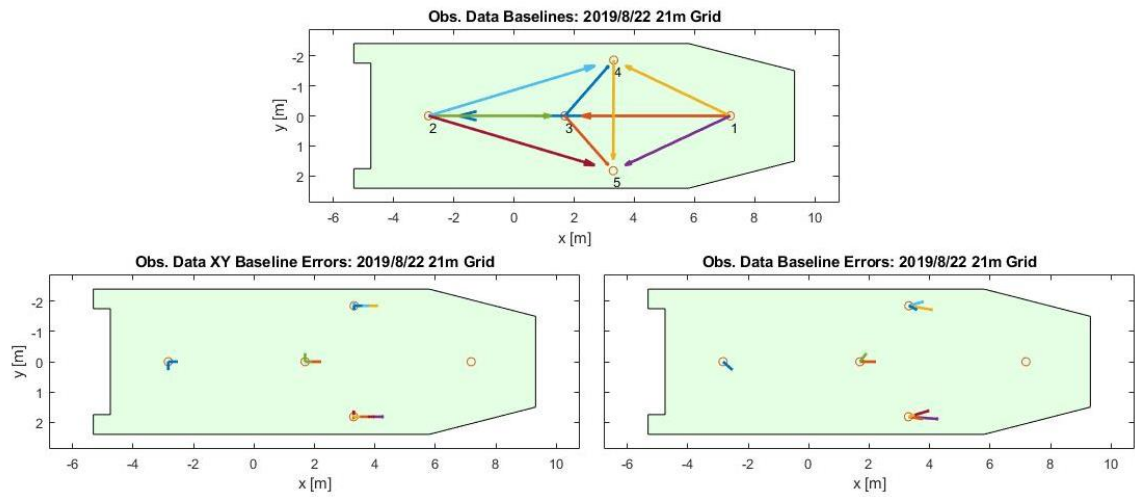
Figure B.6: SRF baseline lengths (top), error vectors (left), and polar errors (right) of a 21 m grid dataset flown on August 22, 2019. Errors are scaled by a factor of 30.
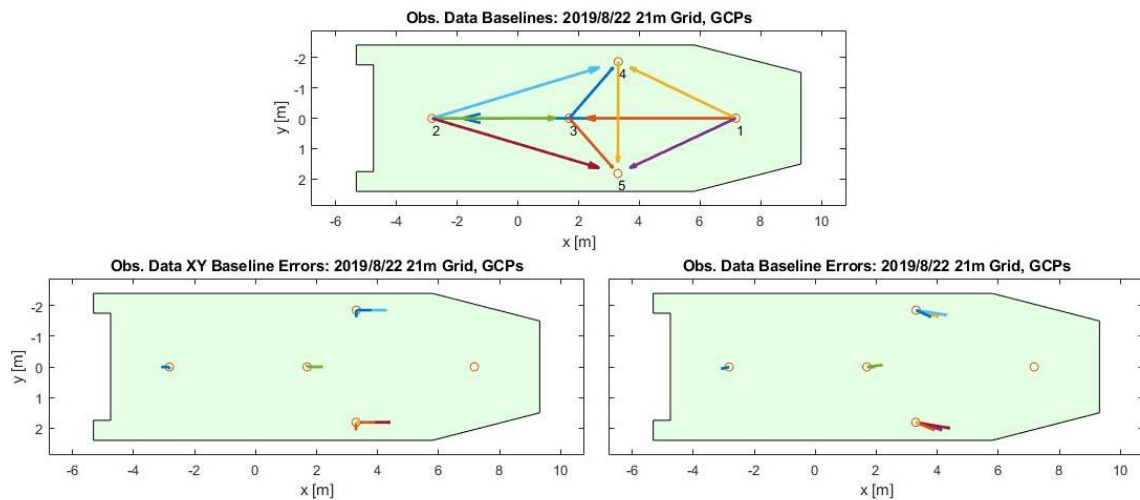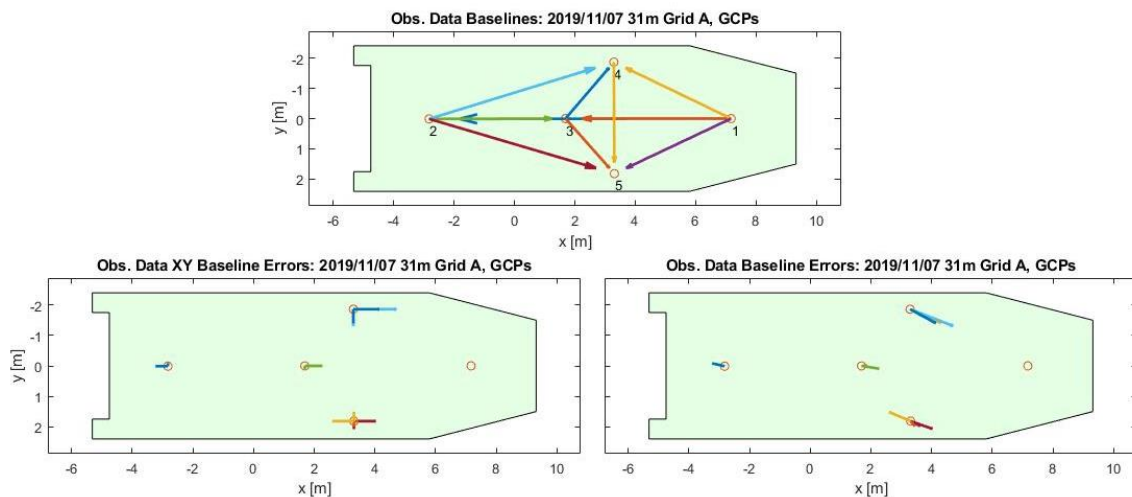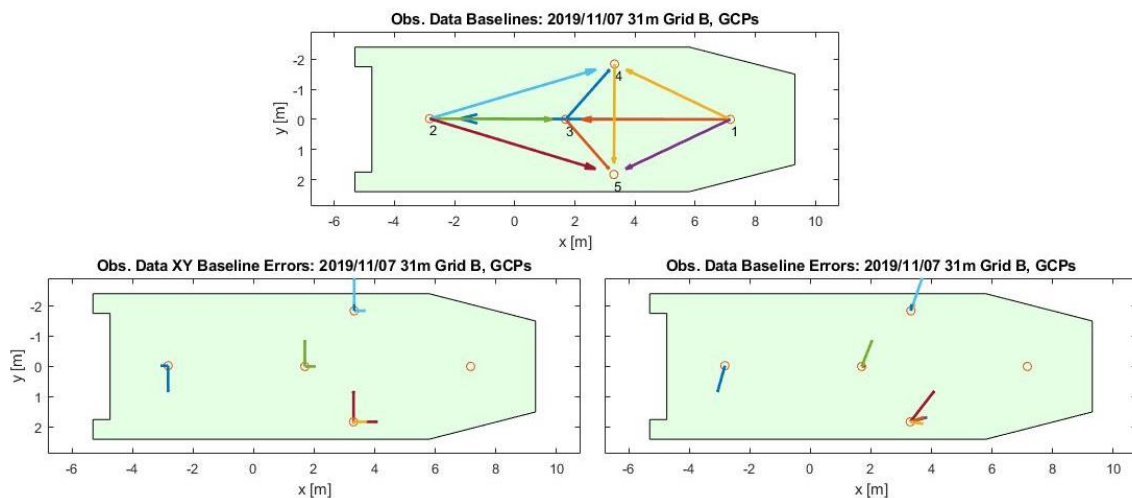
Figure B.7: SRF baseline lengths (top), error vectors (left), and polar errors (right) of a 21 m grid dataset with GCPs flown on August 22, 2019. Errors are scaled by a factor of 30.
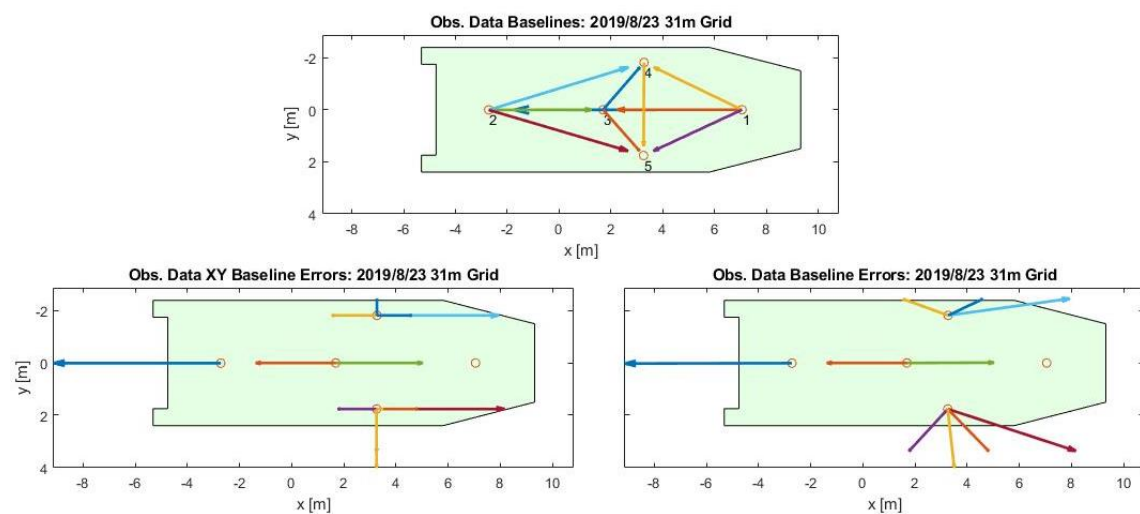
Figure B.8: SRF baseline lengths (top), error vectors (left), and polar errors (right) of a 31 m grid dataset flown on August 23, 2019. Errors are scaled by a factor of 30.
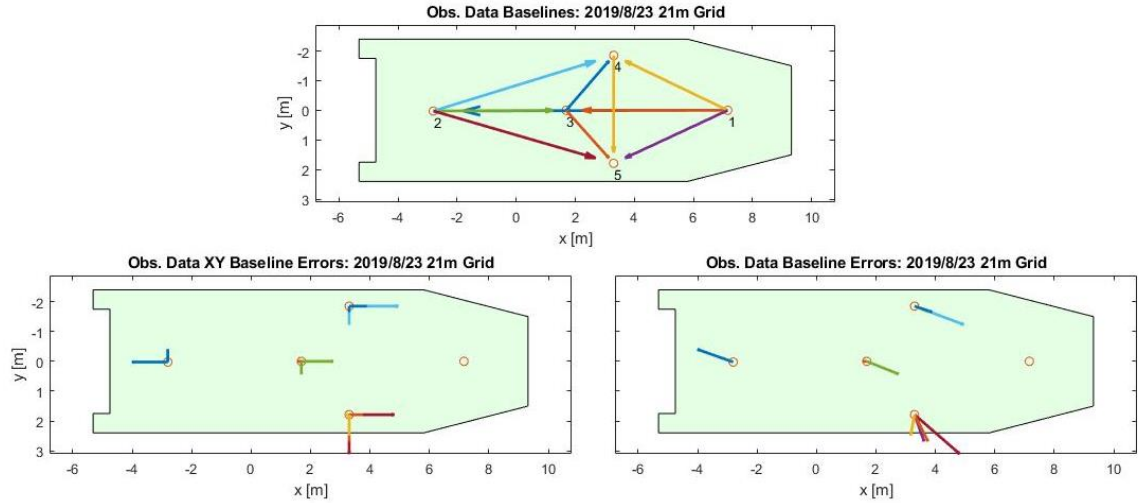
Figure B.9: SRF baseline lengths (top), error vectors (left), and polar errors (right) of a 21 m grid dataset flown on August 23, 2019. Errors are scaled by a factor of 30.
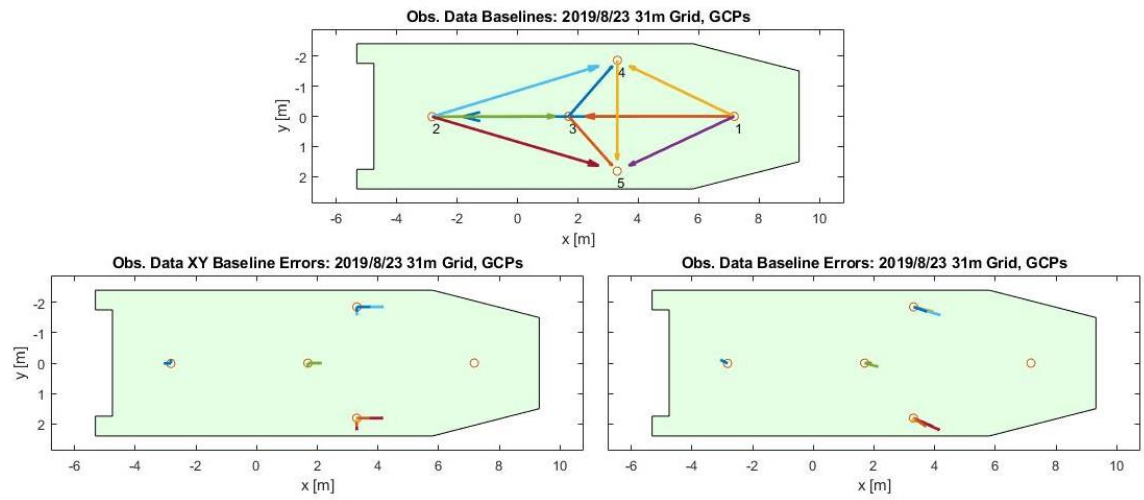
Figure B.10: SRF baseline lengths (top), error vectors (left), and polar errors (right) of a 31 m grid dataset with GCPs flown on August 23, 2019. Errors are scaled by a factor of 30.

Figure B.11: SRF baseline lengths (top), error vectors (left), and polar errors (right) of a 21 m grid dataset with GCPs flown on August 23, 2019. Errors are scaled by a factor of 30.

Figure B.12: SRF baseline lengths (top), error vectors (left), and polar errors (right) of a 31 m grid dataset while the vessel was loosely tied down, flown on November 7, 2019. Errors are scaled by a factor of 30.
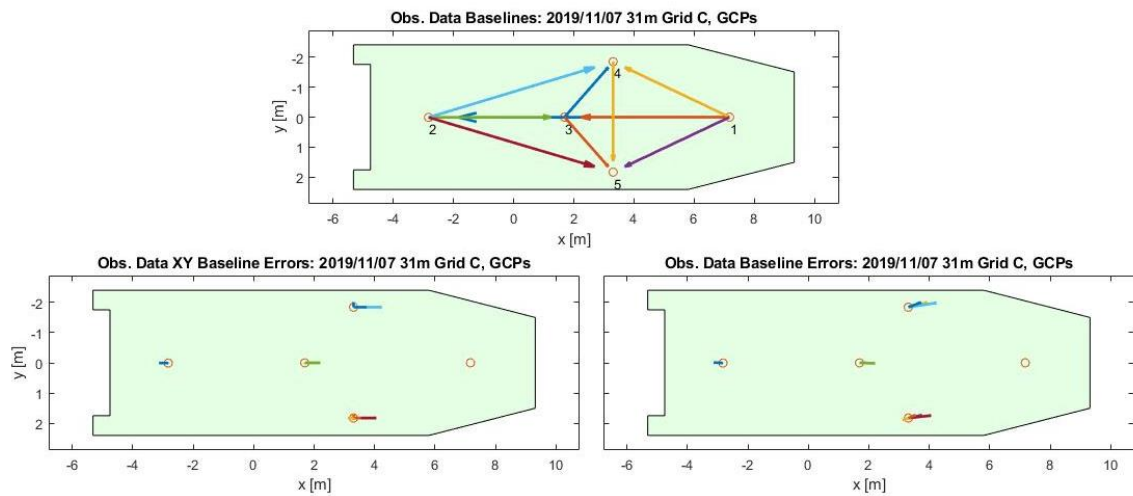
Figure B.14: SRF baseline lengths (top), error vectors (left), and polar errors (right) of a 31 m grid dataset while the vessel was loosely tied down, flown on November 7, 2019. Errors are scaled by a factor of 30.


Figure B.13: SRF baseline lengths (top), error vectors (left), and polar errors (right) of a 31 m grid dataset while the vessel was tied down tight, flown on November 7, 2019. Errors are scaled by a factor of 30.

Figure B.15: SRF baseline lengths (top), error vectors (left), and polar errors (right) of a 31 m grid GCP dataset while the vessel was tied down loose, flown on November 7, 2019. Errors are scaled by a factor of 30.

Figure B.16: SRF baseline lengths (top), error vectors (left), and polar errors (right) of a 31 m grid GCP dataset while the vessel was tied down loose, flown on November 7, 2019. Errors are scaled by a factor of 30.

Figure B.17: SRF baseline lengths (top), error vectors (left), and polar errors (right) of a 31 m grid GCP dataset while the vessel was tied down tight, flown on November 7, 2019. Errors are scaled by a factor of 30.
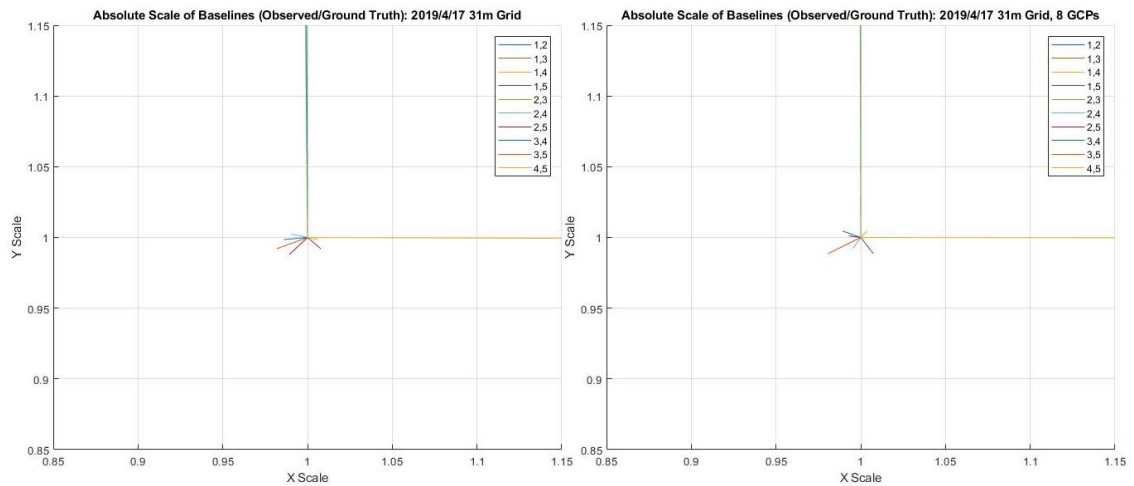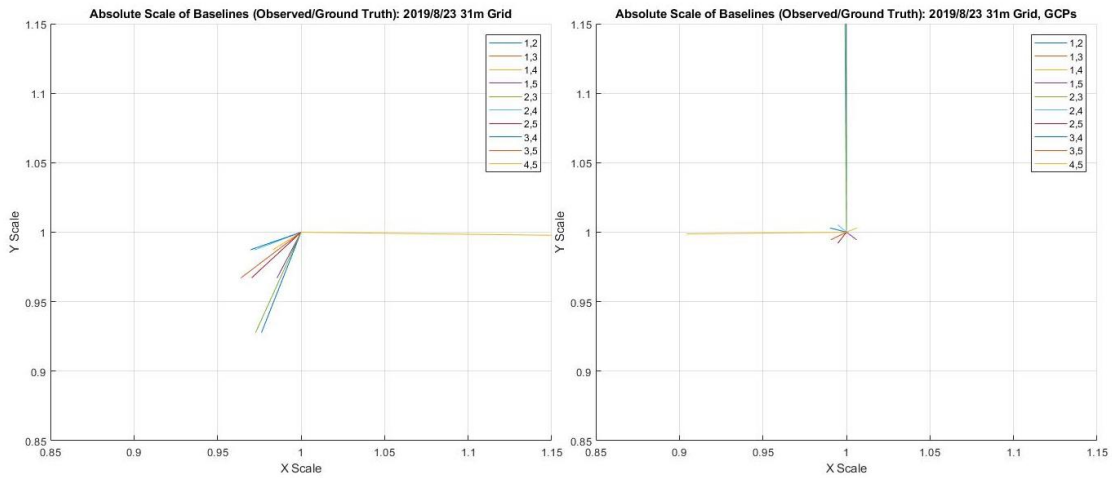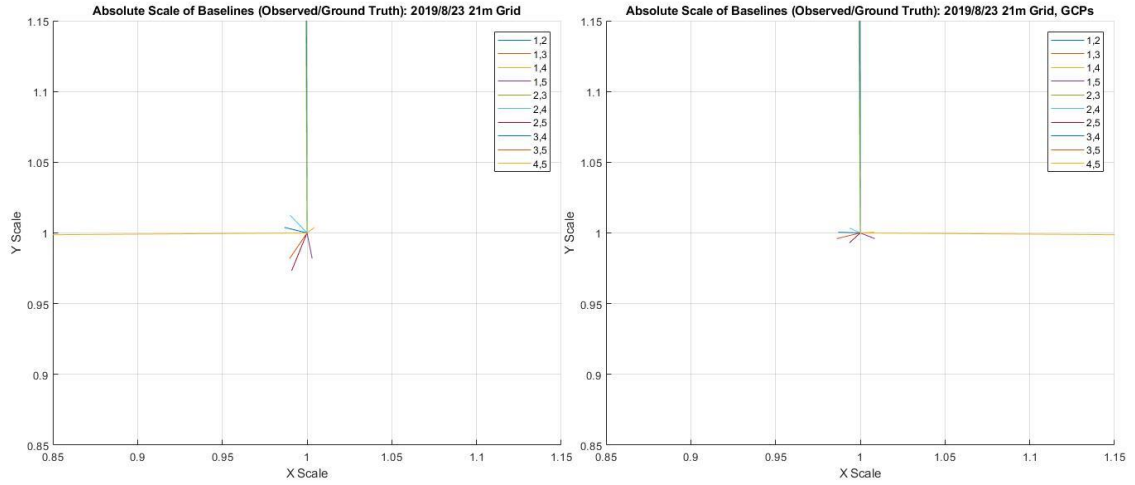

Figure B.18: Absolute scales of SRF baselines observed from a 31 m grid flown on April 17, 2019 without GCPs (left) and with GCPs (right).
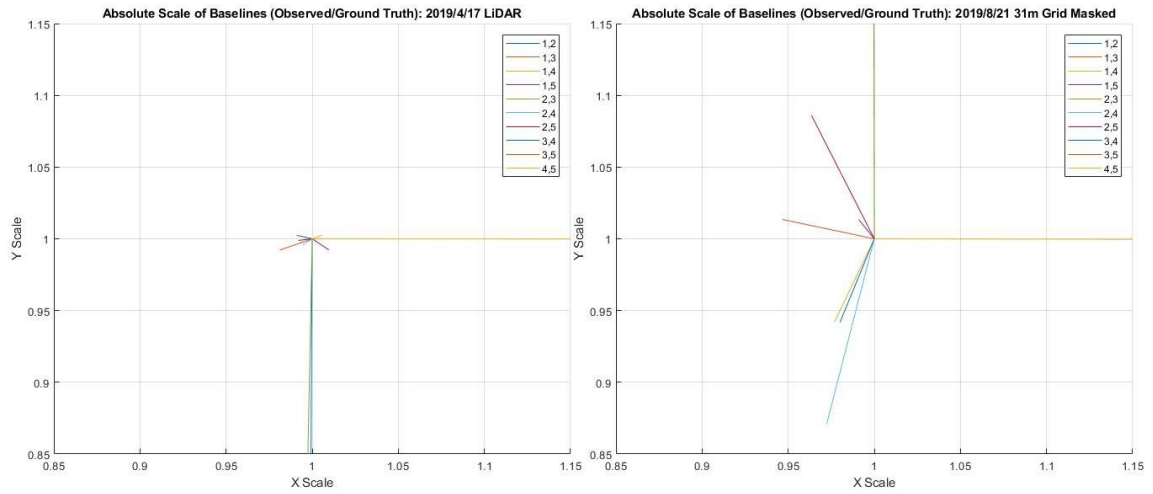
Figure B.19: Absolute scales of SRF baselines observed from lidar data flown on April 17, 2019 (left) and a 31 m grid masked dataset flown on August 21, 2019 (right).
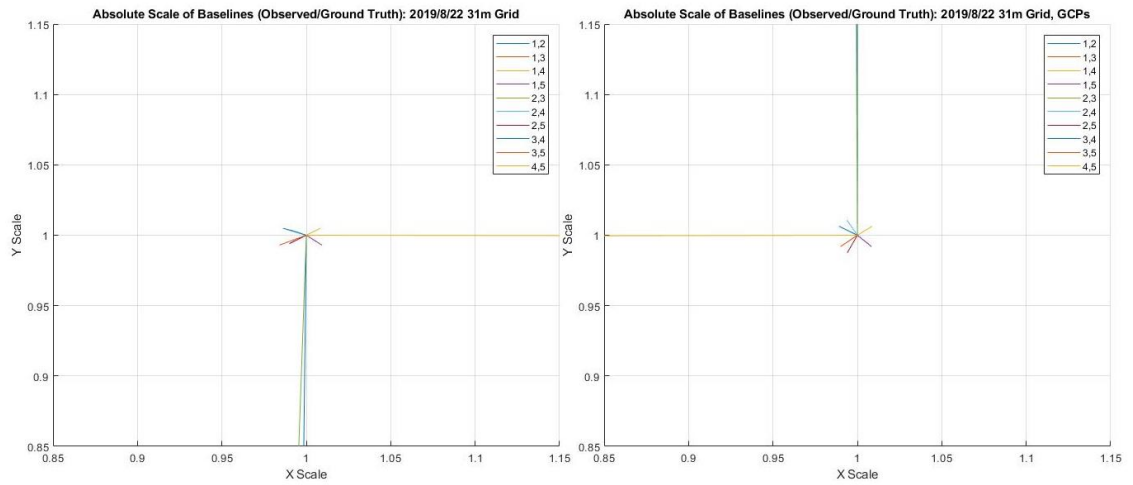
Figure B.20: Absolute scales of SRF baselines observed from a 31 m grid flown on August 22, 2019 without GCPs (left) and with GCPs (right).
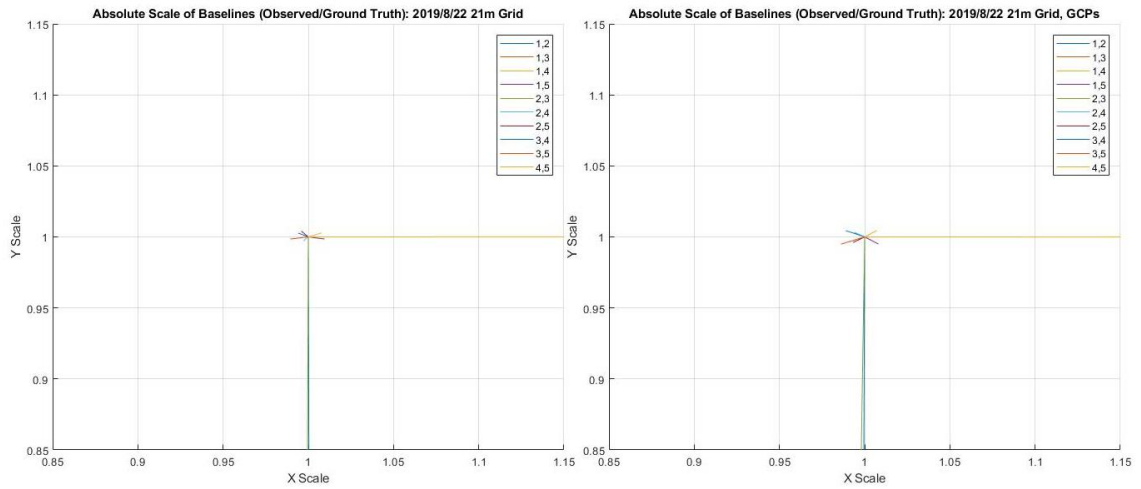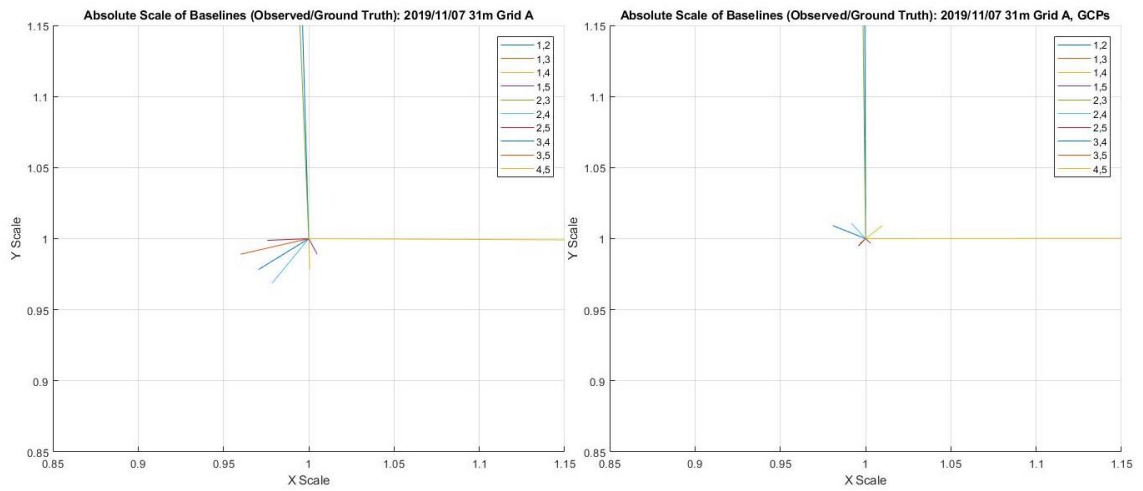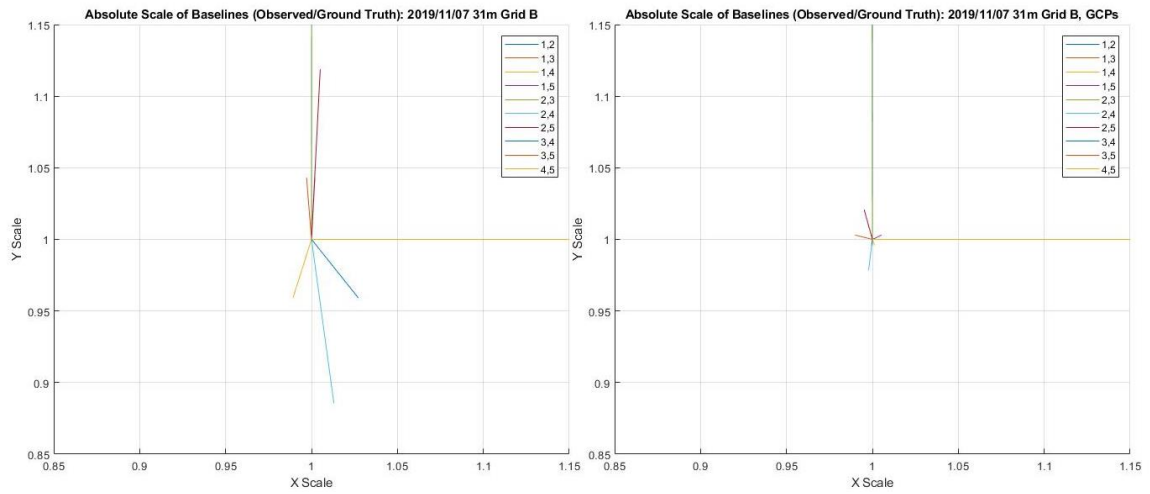
Figure B.21: Absolute scales of SRF baselines observed from a 21 m grid flown on August 22, 2019 without GCPs (left) and with GCPs (right).

Figure B.22: Absolute scales of SRF baselines observed from a 31 m grid flown on August 23, 2019 without GCPs (left) and with GCPs (right).

Figure B.23: Absolute scales of SRF baselines observed from a 21 m grid flown on August 23, 2019 without GCPs (left) and with GCPs (right).

Figure B.24: Absolute scales of SRF baselines observed from a 31 m grid flown on November 7, 2019 without GCPs (left) and with GCPs (right).

Figure B.25: Absolute scales of SRF baselines observed from a 31 m grid flown on November 7, 2019 without GCPs (left) and with GCPs (right).
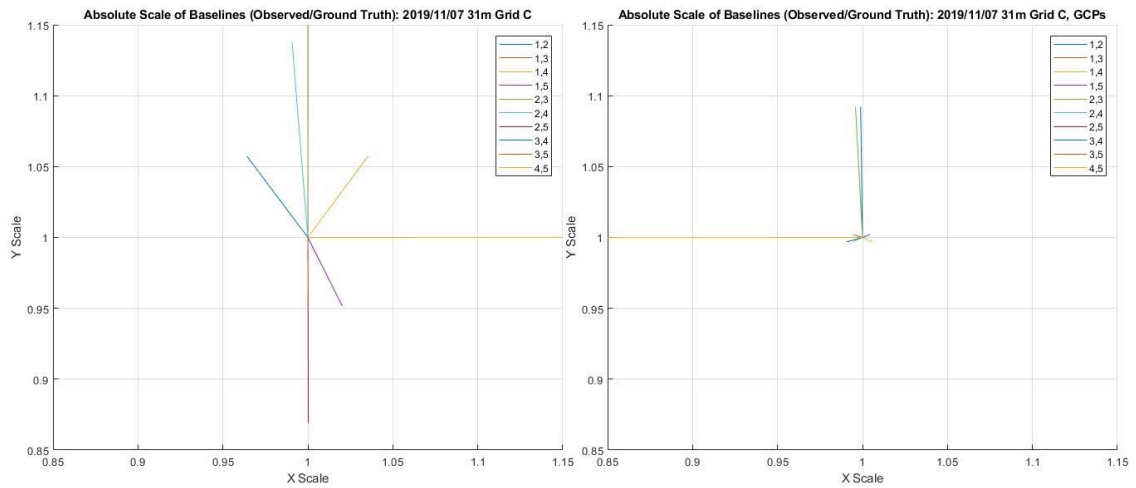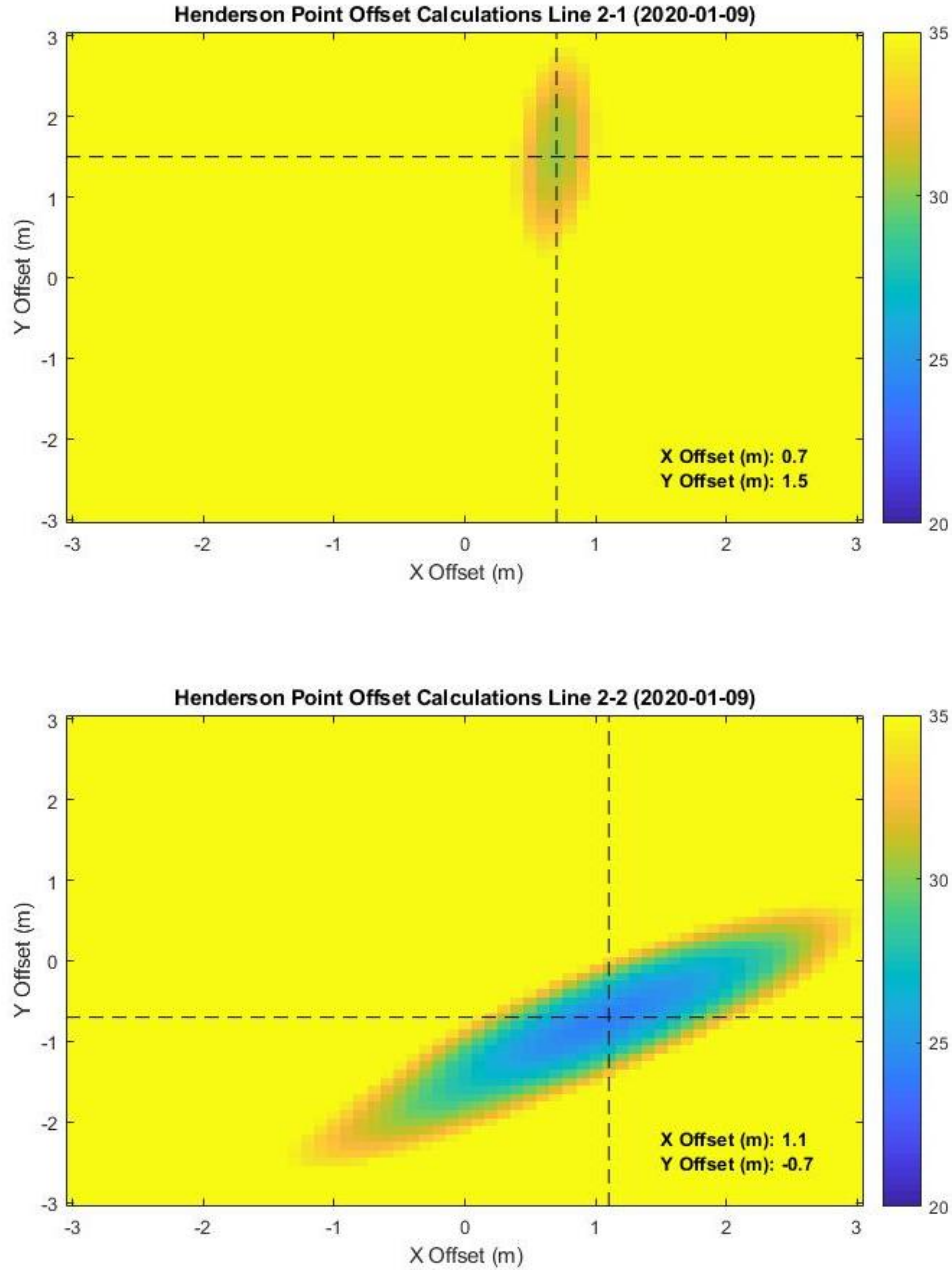

Figure B.26: Absolute scales of SRF baselines observed from a 31 m grid flown on November 7, 2019 without GCPs (left) and with GCPs (right).

Appendix C

Figure C.1: Estimation of x and y vessel offsets using a y calibration line at Henderson Point on January 9, 2020, with the color bar representing sum of the squares of the residuals values between ground truth and observed elevations. Lines 2-1 and 2-2 are the same line performed in opposing directions.
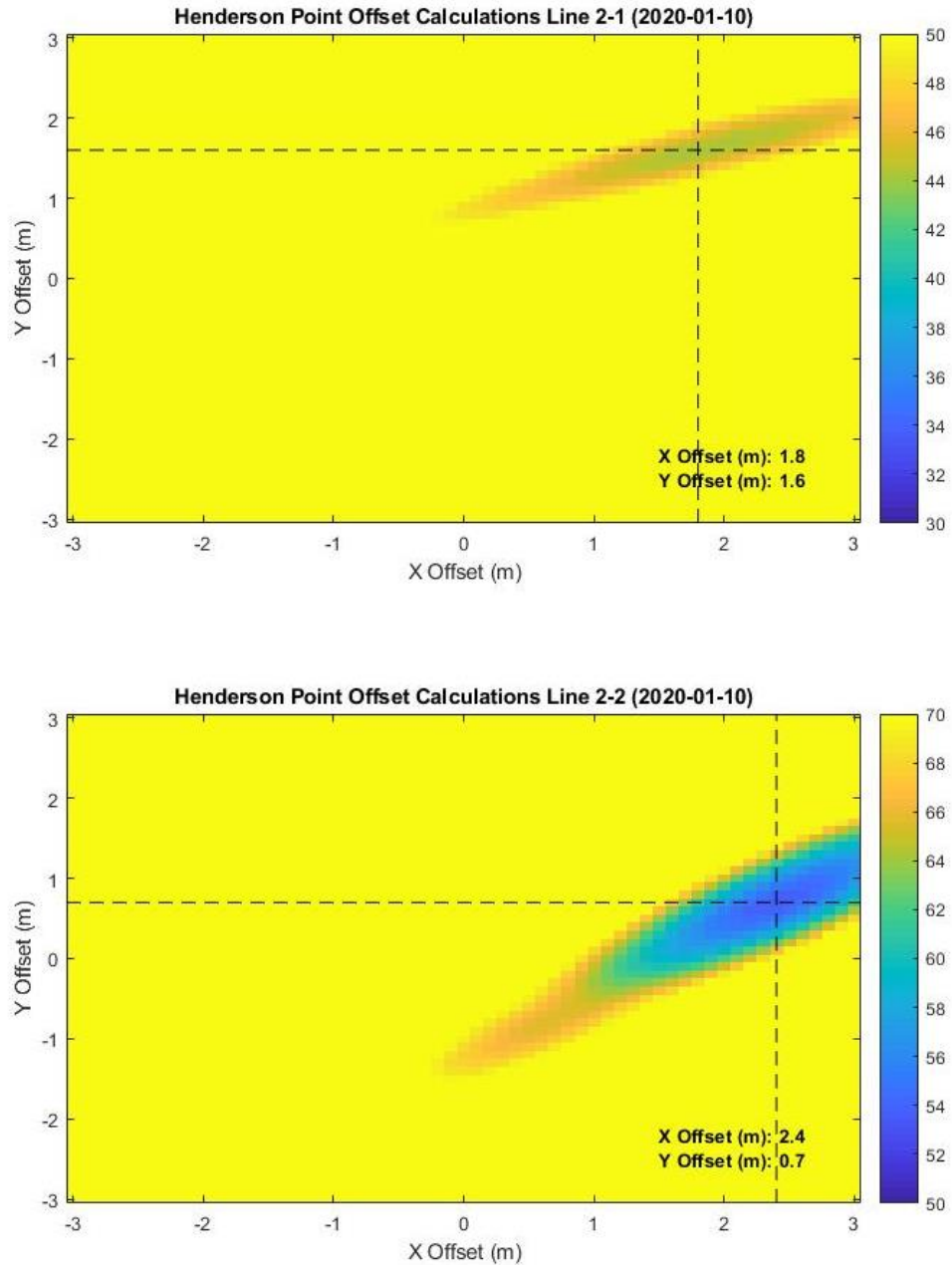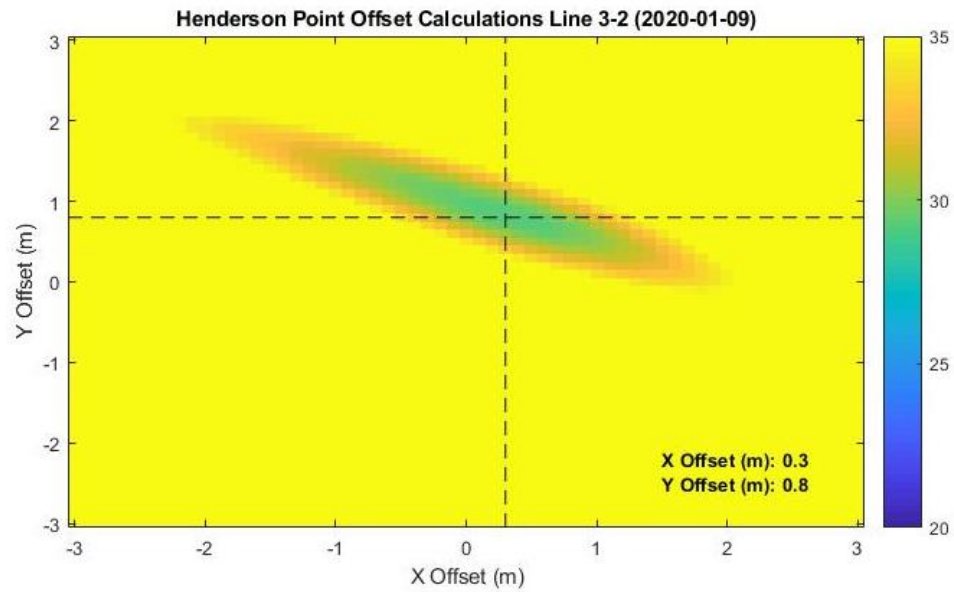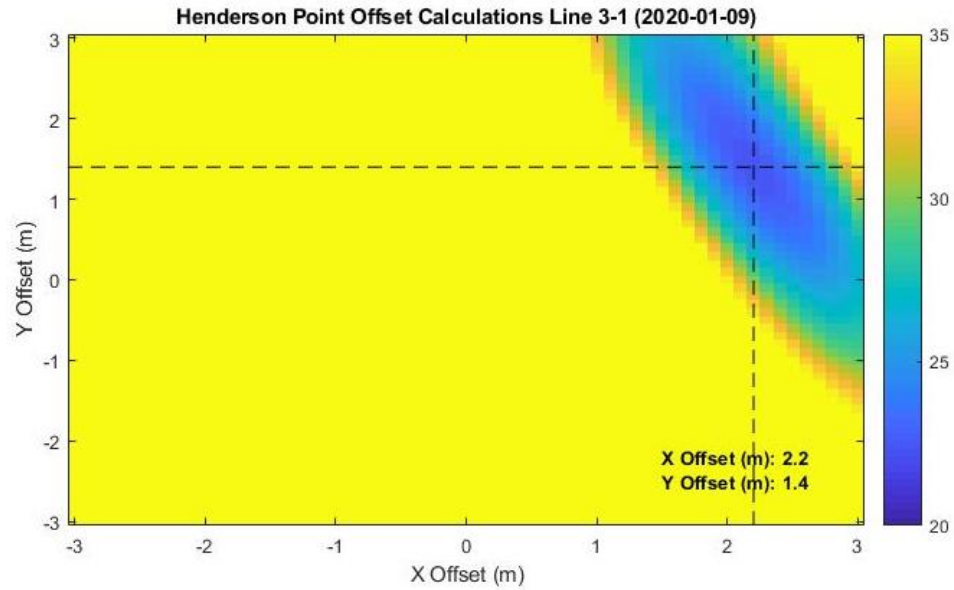
Figure C.2: Estimation of x and y vessel offsets using a y calibration line at Henderson Point on January 10, 2020, with the color bar representing sum of the squares of the residuals values between ground truth and observed elevations. Lines 2-1 and 2-2 are the same line performed in opposing directions.

Figure C.3: Estimation of x and y vessel offsets using a y calibration line at Henderson Point on January 9, 2020, with the color bar representing sum of the squares of the residuals values between ground truth and observed elevations. Lines 3-1 and 3-2 are the same line performed in opposing directions.
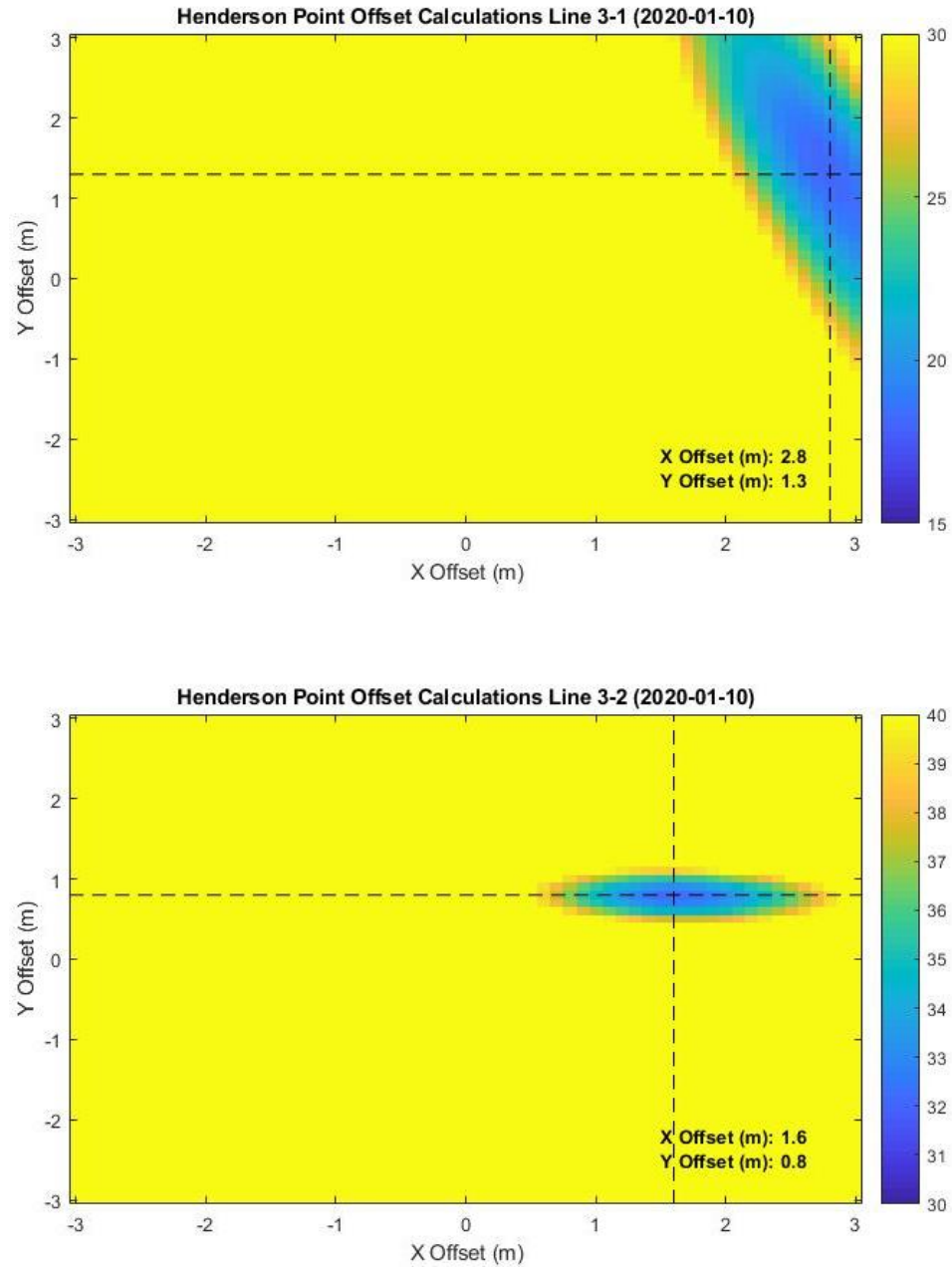
Figure C.4: Estimation of x and y vessel offsets using a y calibration line at Henderson Point on January 10, 2020, with the color bar representing sum of the squares of the residuals values between ground truth and observed elevations. Lines 3-1 and 3-2 are the same line performed in opposing directions.
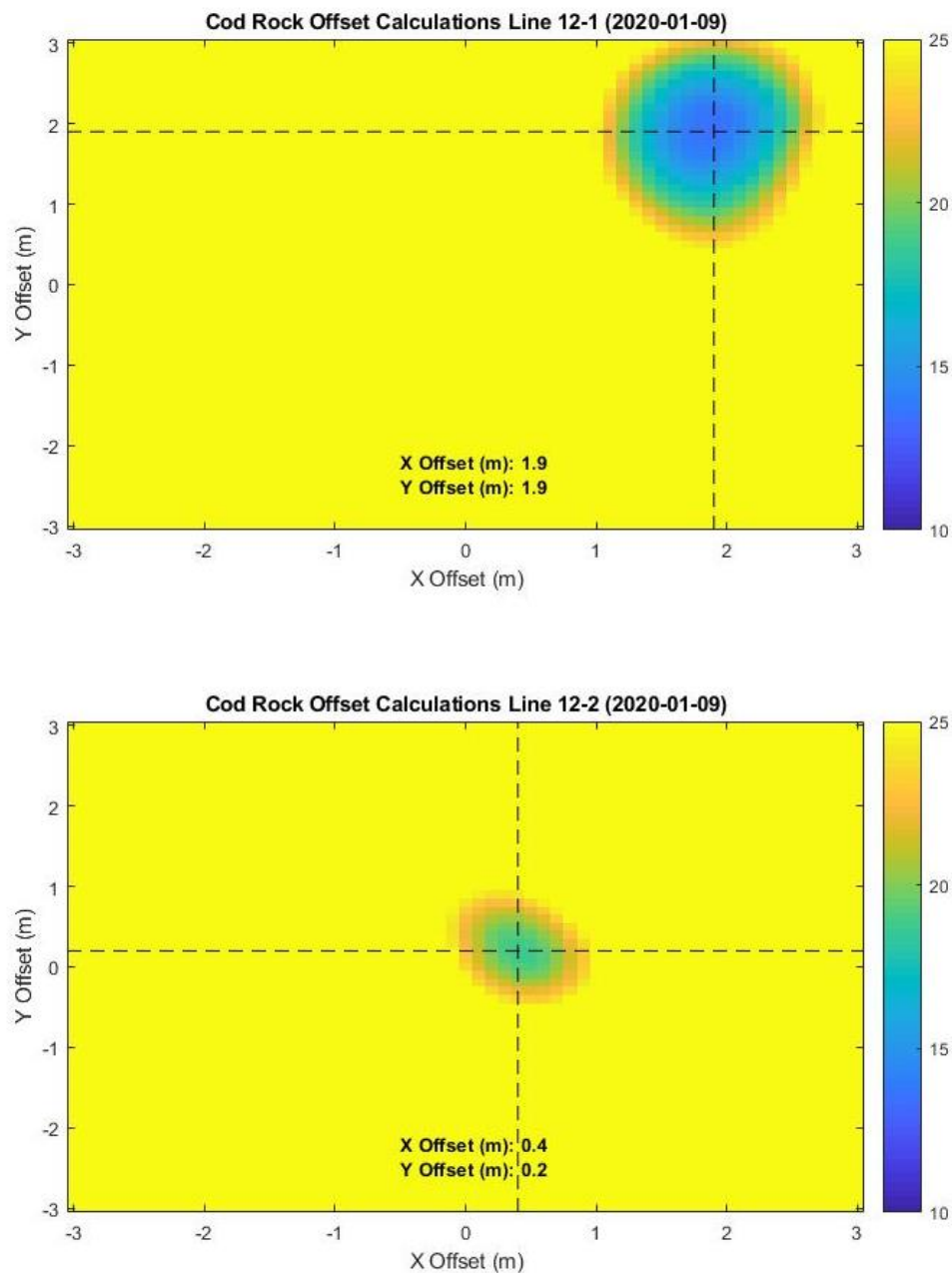
Figure C.5: Estimation of x and y vessel offsets using a x calibration line at Cod Rock on January 9, 2020, with the color bar representing sum of the squares of the residuals values between ground truth and observed elevations. Lines 12-1 and 12-2 are the same line performed in opposing directions.
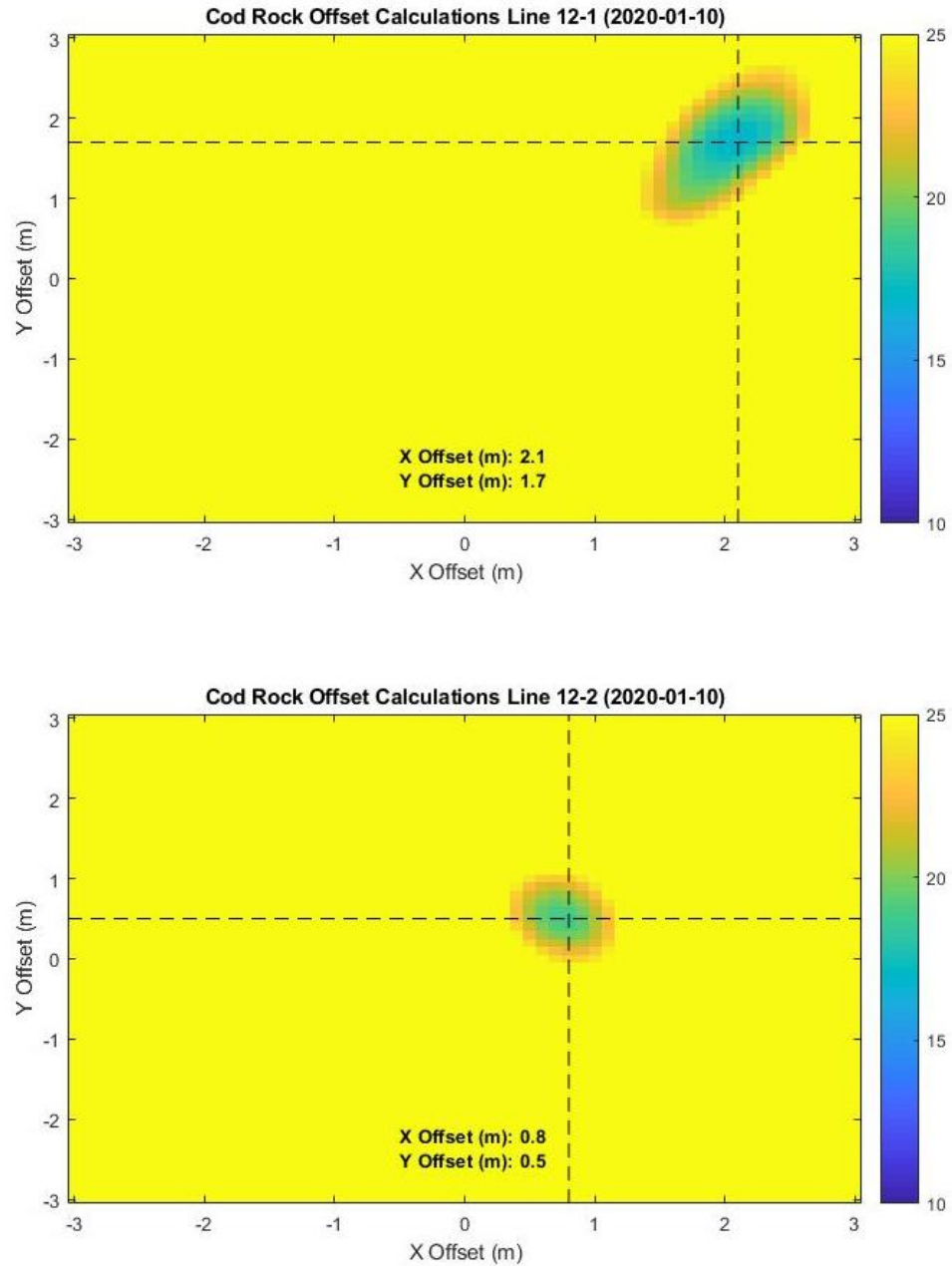
Figure C.6: Estimation of x and y vessel offsets using a x calibration line at Cod Rock on January 10, 2020, with the color bar representing sum of the squares of the residuals values between ground truth and observed elevations. Lines 12-1 and 12-2 are the same line performed in opposing directions.
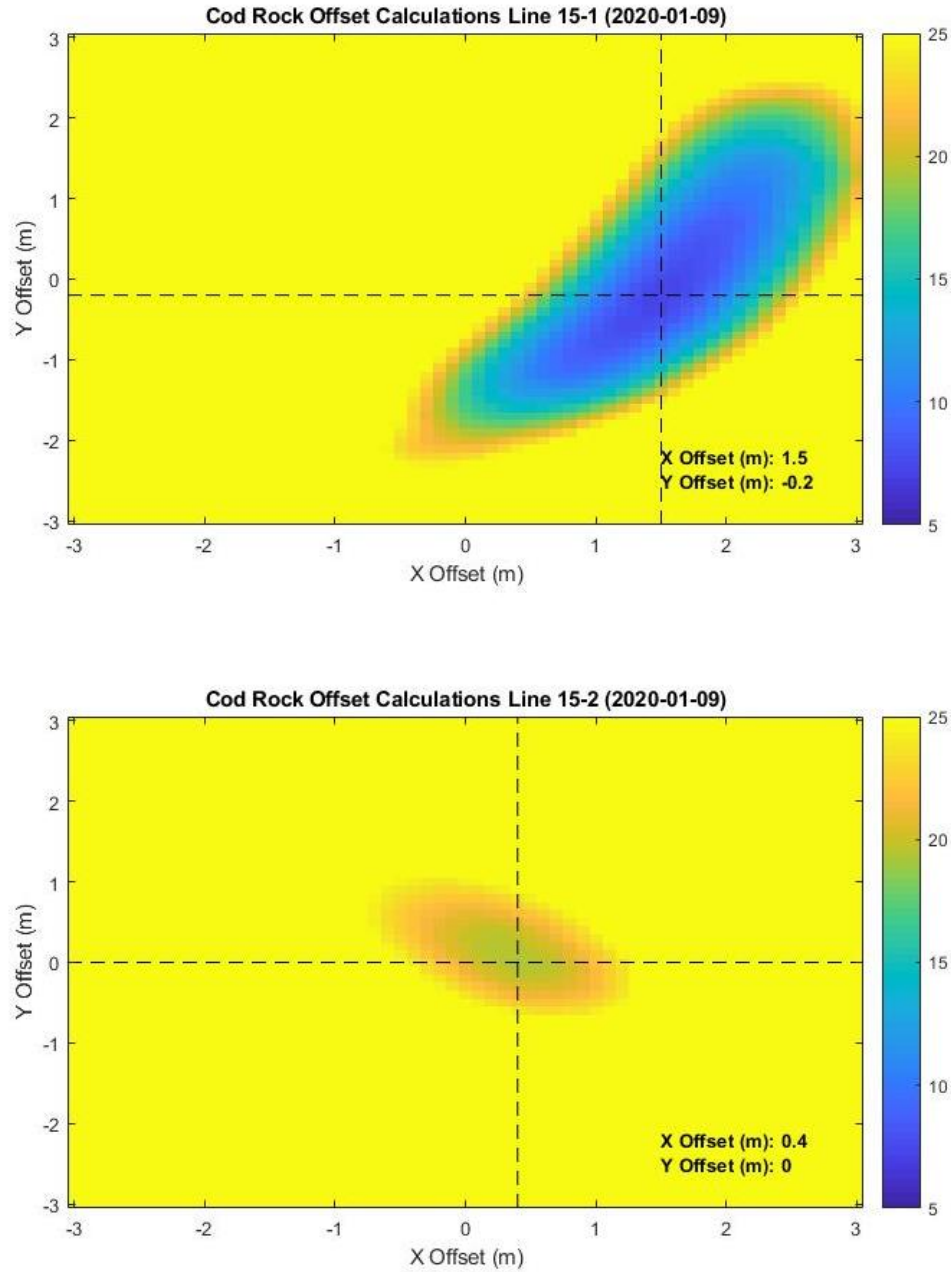
Figure C.7: Estimation of x and y vessel offsets using a y calibration line at Cod Rock on January 9, 2020, with the color bar representing sum of the squares of the residuals values between ground truth and observed elevations. Lines 15-1 and 15-2 are the same line performed in opposing directions.
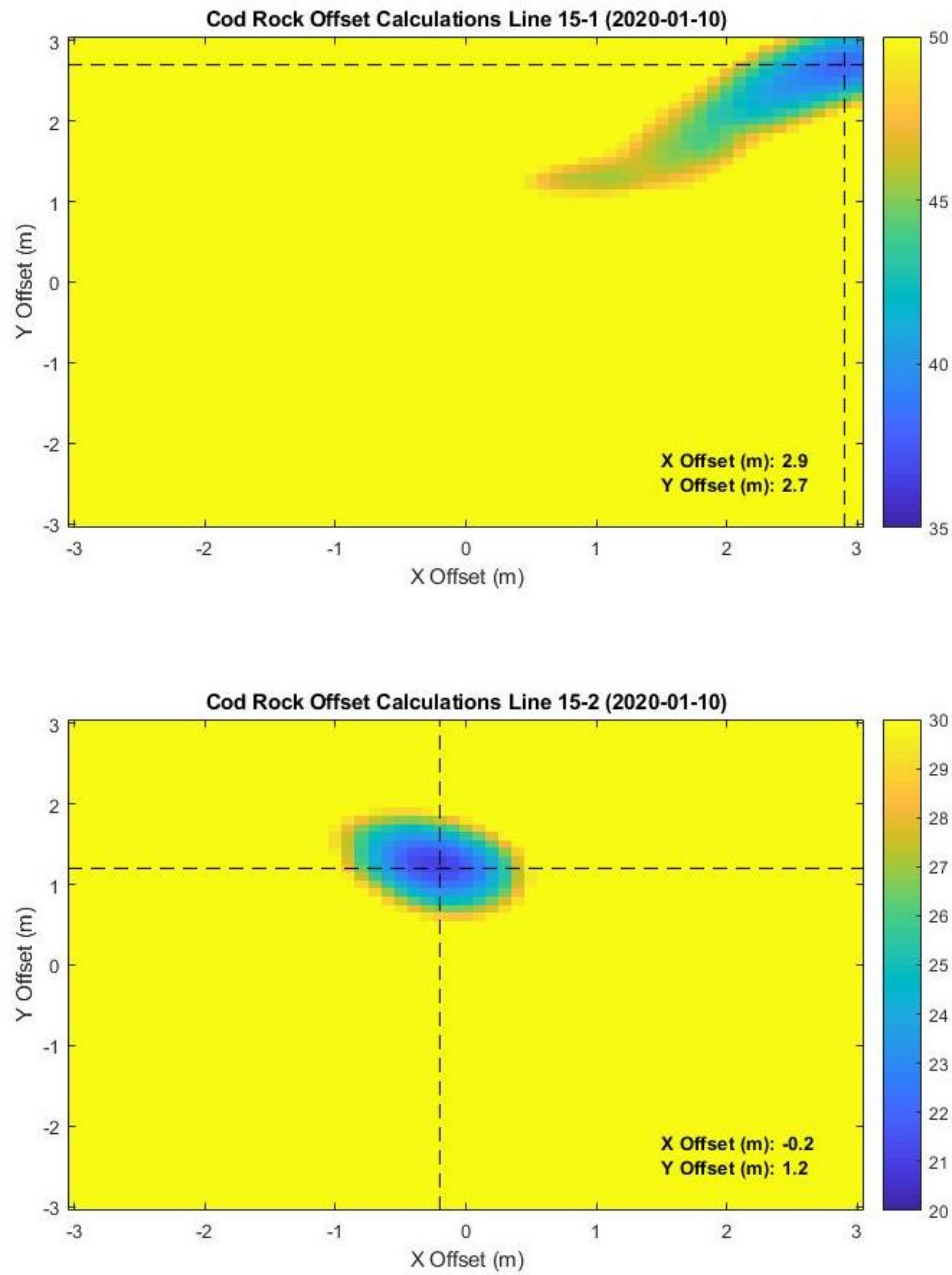
Figure C.8: Estimation of x and y vessel offsets using a y calibration line at Cod Rock on January 10, 2020, with the color bar representing sum of the squares of the residuals values between ground truth and observed elevations. Lines 15-1 and 15-2 are the same line performed in opposing directions.